The Thesis Committee for Jason Charles Sanford
Certifies that this is the approved version of the following thesis:

The Cretaceous-Paleogene boundary deposit in the Gulf of Mexico: Oceanic basin response to the Chicxulub impact
and
Geomechanics of reservoir-scale sand injectites, Panoche Hills, California

APPROVED BY
SUPERVISING COMMITTEE:

Supervisor: _____
Peter B. Flemings

Co-supervisor: _____
Sean P. S. Gulick

_____
John W. Snedden

The Cretaceous-Paleogene boundary deposit in the Gulf of Mexico: Oceanic basin response to the Chicxulub impact
and
Geomechanics of reservoir-scale sand injectites, Panoche Hills, California

by

Jason Charles Sanford, B.A.

Thesis

Presented to the Faculty of the Graduate School of

The University of Texas at Austin

in Partial Fulfillment

of the Requirements

for the Degree of

Master of Science in Geological Sciences

The University of Texas at Austin

August 2015

Acknowledgements

I am indebted to many for their support during my graduate tenure. My family and friends, in particular. There were several times over the past couple of years when I questioned the path I was on, and I thank them for giving me wise counsel and earnest support. Quarter-life crises are difficult to weather, but easier with the haven of those that care. I also owe a great deal to my advisors, whose stress and anxiety I undoubtedly amplified at times. I sincerely appreciate their unwavering support, even when my commitment flagged. Peter, thank you for providing support when I was particularly… conflicted.

Support for my work on the Cretaceous-Paleogene boundary deposit was provided by the Gulf Basin Depositional Synthesis Project and its industry affiliates and the Jackson School of Geosciences at the University of Texas at Austin, and the GBDS at UTIG. I thank Richard Denne, Erik Scott, and James Kaiser for many beneficial interactions.

Support for my work on the Panoche Giant Injection Complex was provided by the UT GeoFluids consortium and their industry affiliates and the Jackson School of Geosciences. Support for fieldwork was provided by UT GeoFluids and the Jackson School of Geosciences. I thank Greg Middleton at the U.S. Bureau of Land Management for access to the Panoche Hills Wilderness Area.

Abstract

The Cretaceous-Paleogene boundary deposit in the Gulf of Mexico: Oceanic basin response to the Chicxulub impact and Geomechanics of reservoir-scale sand injectites, Panoche Hills, California

Jason Charles Sanford, MSGeoSci

The University of Texas at Austin, 2015

Supervisors: Peter B. Flemings

Sean P.S. Gulick

Hydrocarbon exploration in the last decade has yielded sufficient data to evaluate the Gulf of Mexico basin response to the Chicxulub asteroid impact. Given its passive marine setting and proximity to the impact structure on the Yucatán Peninsula, the Gulf is the premier locale in which to study the near-field geologic effect of a massive bolide impact. We mapped a thick (dm- to hm-scale) deposit of carbonate debris at the Cretaceous-Paleogene boundary that is ubiquitous in the Gulf and readily identifiable on borehole and seismic data. We interpret deposits seen in seismic and borehole data in the distal deepwater Gulf to be predominately muddy debrites with minor turbidites based on cores in the southeastern Gulf. Mapping of the deposit in the northern Gulf of Mexico

reveals that the impact redistributed roughly 1.05 x 10^5 km^3 of sediment therein, and over 1.98 x 10^5 km^3 Gulf-wide. Deposit distribution suggests that the majority of sediment derived from coastal and shallow-water environments throughout the Gulf via seismic and megatsunamic processes initiated by the impact. The Texas shelf and northern margin of the Florida Platform were primary sources of sediment, while the central and southern Florida Platform underwent more localized platform collapse. Crustal structure of the ancestral Gulf influenced post-impact deposition both directly and indirectly through its control on salt distribution in the Louann salt basin. Nevertheless, impact-generated deposition overwhelmed virtually all topography and depositional systems at the start of the Cenozoic, blanketing the Gulf with carbonate debris within days.

The Panoche Giant Injection Complex (PGIC) in central California is a complete injectite system. We measured hundreds of injectites over ~600 m of stratigraphic thickness in two locales in order to determine geomechanical controls on injection. We document an injectite architecture in the PGIC that we interpret to reflect a reversal in paleostress state from reverse to strike-slip or normal with proximity to the paleoseafloor. We demonstrate that injectite aperture and bulk strain decrease with distance from the injection source. We model this behavior with three hydraulic fracture geometries and conclude that injectites formed via radially propagating hydraulic fractures. We document a northeast-southwest paleo-orientation preference of subvertical injectites, which reflects the control of Farallon plate subduction on stress state at the PGIC. We estimate that the PGIC was complete and active for ~1 Ma and punctuated by ~20–150 ky-long periods of quiescence based on thickness and spacing of extrudites in the PGIC.

Table of Contents

List of Tables x

List of Figures xi

THE CRETACEOUS-PALEOGENE BOUNDARY DEPOSIT IN THE GULF OF MEXICO: OCEANIC BASIN RESPONSE TO THE CHICXULUB IMPACT 1

Chapter 1: Introduction 1

Chapter 2: Materials and methods 5

Seismic Data 5

Seismic interpretation methods 5

Borehole data 7

Borehole data interpretation methods 8

Mapping methods 9

Chapter 3: Results 15

Structure and distribution of the boundary deposit in the northern Gulf of Mexico 15

Gulf of Mexico paleoshelf 16

Louann salt basin (western/central deepwater Gulf) 18

Eastern deepwater Gulf 21

Structure and distribution of the boundary deposit at the Chicxulub impact basin 22

Sedimentology of the boundary deposit in the southeastern Gulf of Mexico 23

Chapter 4: Discussion 36

Regional sediment sources for the boundary deposit and implications for depositional mechanics and timing 36

Salt and basement control on boundary deposit distribution 38

Volume of sediment mobilized by the Chicxulub impact in the Gulf of Mexico 40

Chapter 5: Summary and conclusions....42

GEOMECHANICS OF RESERVOIR-SCALE SAND INJECTITES, PANOCHE HILLS, CALIFORNIA 44

Chapter 6: Introduction....44

Chapter 7: Geologic background....50

Tectonic and depositional setting....50

Stratigraphy of the Panoche Giante Injection Complex....51

Chapter 8: Materials and methods....54

Field measurement....54

Unmanned aerial vehicle photogrammetry....55

Grain size analysis....55

Laboratory mapping....55

Chapter 9: Results....57

Stratigraphy of the Panoche Giant Injection Complex....57

Architecture of the Panoche Giant Injection Complex....57

Source interval....58

Injectite interval....59

Sill zone....61

Sill-dike transition zone....62

Dike zone....62

Extrudite interval....70

High-angle injectite behavior in the upper injectite interval....71

Paleo-orientation of exposures....73

Two-dimensional injectite models....73

Chapter 10: Discussion....80

Injection geomechanics....80

Tectonic control for injection....82

Paleostress regime at the Panoche Giant Injection Complex....83

Duration and periodicity of injection 86

Chapter 11: Summary and conclusions 87

Appendices 88

Appendix 1: Detailed mapping methodology of the Cretaceos-Paleogene boundary deposit 88

Appendix 2: Core description of the Cretaceous-Paleogene boundary deposit at DSDP Leg 77 Sites 536 and 540 94

Appendix 3: True Stratigraphic Position transformation for field measurements of the Panoche Giant Injection Complex 110

Appendix 4: Unmanned Aerial Vehicle data acquisition and processing of Moreno Gulch, Panoche Hills 126

References 127

Vita… 139

List of Tables

Table 1: KPBD facies at sites 536 and 540.....33

Table 2: Stratigraphic thickness of the Panoche Giant Injection Complex. ...49

Table 3: Stratigraphic thickness of the Moreno Formation and underlying Panoche Group.....53

Table 4: Number of orientation and aperture measurements and scan lines...56

Table 5: Scan line grid geometries and logistics.....56

Table 6: Injectite paleo-orientation by style and architectural zone. 66

Table 7: Thickness, proximity, and paleogeographic setting of KPBD locales in the circum-Gulf region.....90

Table 8: Velocities for seismic and megatsunami waves used for first arrival calculation. 91

Table 9: Data sources for seismic and borehole data used in this study. 91

Table 10: Sources of seismic and borehole data used in this study. 92

Table 11: Mapping parameters used in this study.....93

Table 12: Bedding and injectite orientation measurements and injectite aperture measurements collected in Moreno Gulch (MG) and Marca Canyon (MC).....125

List of Figures

Figure 1: **(A)** Paleogeographic map of the Gulf of Mexico at the end of the Cretaceous [*Blakey*, 2011], illustrating thickness and paleogeographic setting of known KPBD locales in the circum–Gulf region. **(B)** Schematic lithologic sections of the KPBD by distance from the crater. 4

Figure 2: Study area and data extent in the Gulf of Mexico.. 11

Figure 3: Seismic facies of the K-Pg KPBD in the Gulf of Mexico, with representative localities annotated. 12

Figure 4: Segment of line CHICX-B from the 1996 Chicxulub survey demonstrating seismic facies of the KPBD at the crater, as well as crater morphology. 13

Figure 5: Type log of the KPBD in the deepwater Gulf of Mexico, demonstrating its characteristic signature: blocky with low gamma-ray counts (GR), high-resistivity (RES), low neutron-porosity (Φ_N) and bulk-density (ρ_b), and high compressional acoustic velocity (DTC). 14

Figure 6: Structure at the top of the KPBD in the northern Gulf of Mexico, illustrating regional structural features and extreme local variation in structure within the Louann salt basin 25

Figure 7: Interval thickness of the KPBD in the northern Gulf of Mexico, suggesting local basement and salt control. 26

Figure 8: Uninterpreted (top) and interpreted (below) regional seismic reflection transects through the Gulf of Mexico, illustrating KPBD thickness and structure through structural provinces in the basin. Annotations at the top and base of each interpreted section indicate geographic and structural provinces, respectively. 28

Figure 9: Uninterpreted (top) and interpreted (bottom) depth-converted seismic reflection section documenting suprasalt carapaces containing the KPBD and condensed Mesozoic and Early Cenozoic (Paleogene) strata in the Louann salt basin, Keathley Canyon (KC). 29

Figure 10: Structure at the base of the KPBD at the Chicxulub impact basin, illustrating crater morphology and preexisting structure. 30

Figure 11: Interval thickness of the KPBD at the Chicxulub crater. Structural features of the crater (blue lines) and preexisting Chicxulub embayment (dashed red line) are taken from Figure 10. 31

Figure 12: Idealized lithology of sites 540 and 536 cores, together interpreted to represent the entire KPBD sequence in the southeastern Gulf. 32

Figure 13: Schematic model for post-impact deposition in the eastern Gulf of Mexico. 35

Figure 14: Schematic model for postimpact deposition in the deepwater Louann salt basin province. 41

Figure 15: (A) Location map of the PGIC in the Panoche and Tumey Hills of central California. (B) Stratigraphy of the mud-prone Moreno Formation overlying the sand-prone Uhalde Formation, as well as a generalized schematic of PGIC architecture. (C) Schematic tectonic model of the PGIC on the western margin of the Great Valley forearc basin in the Late Creteaceous and Early Paleocene. 46

Figure 16: Aerial imagery of (A) Moreno Gulch and (B) Marca Canyon in the northern Panoche Hills illustrating mapped source and remobilized sands of the PGIC, location of measurements and photogrammetric model acquired for this study, and stratigraphy of the Moreno Formation from [*Bartow*, 1996]. 48

Figure 17: Schematic measured sections of (A) Moreno Gulch and (B) Marca Canyon illustrating architecture of the PGIC and stratigraphy of the Moreno Formation. 52

Figure 18: Quantitative grain size of 10 samples of remobilized and depositional sands in Moreno Gulch Marca Canyon. 59

Figure 19: Field photographs of (A) source, (B–I) injected, and (J–O) extruded sand in Moreno Gulch and Marca Canyon.....65

Figure 20: (A) Injectite paleodip versus TSP above PGIC source for all injectites measured in Moreno Gulch and Marca Canyon. Stereographic projections of poles to planes of injectite paleo-orientation in the (B) dike zone, (C) SDTZ, and (D) sill zone. 67

Figure 21: Stratigraphically extensive high-angle dikes and associated sills and low-angle dikes mapped in the middle to upper SDTZ and dike zone in (A) Moreno Gulch and (B–C) Marca Canyon. 68

Figure 22: Simplified stratigraphically extensive high-angle dikes in (A) Moreno Gulch and (B–C) Marca Canyon documenting several examples of Type II injectite aperture behavior. 69

Figure 23: (A) Average and (B) normalized cumulative high-angle dike aperture versus stratigraphic position. The "source" is the top of the Uhalde Formation. 72

Figure 24: (A) Paleo-orientation (solid) and modern orientation (dashed) of planes representing exposures in Marca Canyon and Moreno Gulch. (B) Schematic of paleo-exposure of stratigraphically extensive high-angle dikes in Moreno Gulch (c.f. Figure 21A) and (C) simplified model of injectites intersected by paleo-exposure. 73

Figure 25: Illustration of fracture geometries in (A) PKN, (B) GdK, and (C) penny fracture models. (D) Fracture aperture versus fracture length for the three fracture models, defined by equations for width in (A–C). 77

Figure 26: Traverse geometries for the three fracture models. (A–C) Cartoons of injectite geometries for GdK, PKN, and penny fracture models. (D–F) Aperture versus true stratigraphic position (TSP) for four traverses at at different points of the injectite geometries 78

Figure 27: (A) Average and (B) normalized cumulative aperture of GdK (red), PKN (blue), and penny (black) geometries.....79

Figure 28: (A) Average and (B) normalized cumulative aperture of model geometries and field data.. 82
Figure 29: Illustration of (A) linear propagation from a linear source as per the PKN fracture model and (B) radial propagation from a point source as per the penny model. 82
Figure 30: (A) Schematic pore pressure profile of the PGIC illustrating rotation of stress state from reverse to normal or strike-slip with proximity to the seafloor. (B) Pore pressure profile of the Kumano forearc basin and Nankai accretionary prism calculated from borehole failures by *Chang et al.* [2010]......85
Figure 31: Diagram illustrating terminology and trigonometry of transform from Cartesian coordinates to True Stratigraphic Position.....111

THE CRETACEOUS-PALEOGENE BOUNDARY DEPOSIT IN THE GULF OF MEXICO: OCEANIC BASIN RESPONSE TO THE CHICXULUB IMPACT

Chapter 1: Introduction

The Cretaceous-Paleogene (K-Pg) extinction event is the latest of five major extinction events in the Phanerozoic and is responsible for the extinction of ~36% of known marine animal genera and ~76% of known marine invertebrates [*Jablonski*, 1994; *Raup and Sepkoski*, 1982; *Rohde and Muller*, 2005]. The prevailing theory for the event invokes the Chicxulub asteroid impact as the sole cause of rapid global climatologic and ecologic crisis that occurred at the start of the Cenozoic [e.g., *Pälike*, 2013; *Renne et al.*, 2013]. There is a consensus within the geologic community that impact-initiated processes led to the global deposition of the K-Pg boundary deposit (KPBD) [e.g., *Bralower et al.*, 2010; *Denne et al.*, 2013; *Schulte et al.*, 2010], though the theory is not without critics [e.g., *Keller*, 2011; *Keller et al.*, 1993; *Keller et al.*, 2003a].

The single-impact Chicxulub-crater hypothesis for the origin of the KPBD is now corroborated by more than 350 sites throughout the world that document the K-Pg boundary [*Claeys et al.*, 2002; *Schulte et al.*, 2010; *Smit*, 1999]. Furthermore, substantial change in thickness and lithology of the KPBD with proximity to the Chicxulub crater strongly suggests a genetic link between the two (Figure 1) [*Schulte et al.*, 2010]. Shocked quartz, spherules, and clays enriched in platinum group elements have been identified at sites around the world, from proximal to virtually antipodal to the crater [e.g., *L W Alvarez et al.*, 1980; *Claeys et al.*, 2002; *Gilmour and Anders*, 1989; *Kyte et al.*, 1985; *Schulte et al.*, 2010; *Smit*, 1999]. At sites more than ~5,000 kilometers from the crater (e.g., Gubbio, Italy, Caracava de la Cruz, Spain, and El Kef, Tunisia), this boundary clay, or “fireball layer” [*Hildebrand and Boynton*, 1990], comprises the entire KPBD [*Perch-Nielsen et al.*, 1982; *Schulte et al.*, 2010; *Smit and Hertogen*, 1980]. Within

~5,000 kilometers of the crater (e.g., "intermediate" sites in the Western Interior, Bermuda Rise, Caribbean, and shallow-water Gulf), the boundary clay incorporates a lower spherule-rich layer, and the entire KPBD is up to 1 m thick [e.g., *Izett*, 1990; *MacLeod et al.*, 2007; *Schulte et al.*, 2009].

Even nearer to the crater (<1000 km), this lower ejecta bed incorporates a substantial clastic component with sedimentary structures indicative of high-energy depositional mechanisms (e.g. turbidity currents, debris flows, slumps, and slides) [*Alegret et al.*, 2001; *Campbell et al.*, 2007; *Ferrell et al.*, 2011; *Frederiksen et al.*, 1982; *Grajales-Nishimura et al.*, 2000; *Keller et al.*, 2003b; *Smit et al.*, 1992; *Soria et al.*, 2001; *Stinnesbeck et al.*, 1993; *Yancey*, 1996; *Yancey and Liu*, 2013]. Paleogeography is increasingly a factor in KPBD thickness, geometry, and composition, though the lithologic consistency of the KPBD is remarkable throughout the Gulf. Because the impact occurred on the margin of the Yucatán Peninsula, a nominal 1,000-km radius circumscribes a wide range in paleogeography, and thus depositional setting and local response to the impact, from coastal to abyssal (Figure 1A). As such, the KPBD within this distance exhibits a wide range of thickness, from ~1 m (e.g., Brazos River outcrop, Texas) [*Yancey*, 1996; *Yancey and Liu*, 2013] to nearly 1 km (e.g., Cacarajícara formation, Cuba, impactites within the Chicxulub impact crater, Mexico) [*Gulick et al.*, 2013; *Tada et al.*, 2003] or more (this study; Figure 1). Generally, shallow-water deposits in the Gulf range from 1 m to many decimeters thick, whereas deepwater deposits are hectometers thick (Figure 1).

Given this established change in character and thickness with proximity to the Chicxulub crater, the Gulf of Mexico represents a geographic, energetic, and depositional end-member to the continuum of global KPBD settings. The impact input ~100 teratons into the Earth system [*Covey et al.*, 1994] and likely generated a magnitude 11 earthquake [*Day and Maslin*, 2005] at

the site of impact, initiating seismic shaking and ground-roll and a megatsunami wave train that would have traversed the Gulf within an hour [e.g., *Boslough et al.*, 1995; *Denne et al.*, 2013; *Klaus et al.*, 2000; *Norris and Firth*, 1999; *Norris et al.*, 2000; *Tada et al.*, 2003; *Yancey and Liu*, 2013]. Given its proximity to the crater and its exceptional accommodation space, the deepwater Gulf was likely a regional sink to the tremendous amount of sediment generated by the impact. Thus, the Gulf is the premier locale in which to study the near-field geologic effect of a massive bolide impact. However, until recently, data in the Gulf has been limited to the basin periphery because of the expense and difficulty of acquiring deepwater data. Hydrocarbon exploration in the past decade has yielded significant borehole and seismic data that can be used to better understand the deepwater response to the impact in the Gulf [e.g. *Denne et al.*, 2013; *E D Scott et al.*, 2014].

It is the aim of this study to characterize and map the KPBD using borehole and seismic data throughout the northern Gulf of Mexico and to map the continuity of the KBPD from the northern Gulf to the Chicxulub impact basin. We present available lithologic data to determine the mechanisms responsible for deposition of the KPBD in the wake of the impact. We present data that leads to a comprehensive understanding of the deposit in the deepwater Gulf of Mexico, including the identification of impact-mbilized sediment sources and the role of syndepositional salt topography and postdepositional salt migration. For the first time, the KPBD is correlated from the Chicxulub impact basin to the deepwater Gulf, stratigraphically establishing a relationship between the impact and the KPBD.

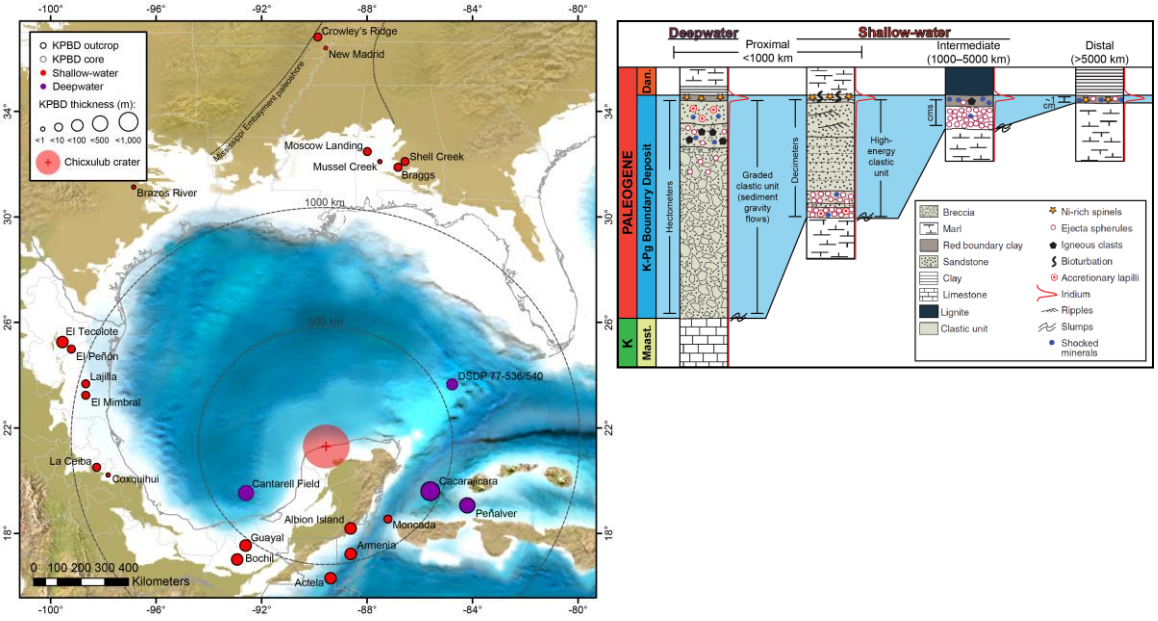

Figure 1: **(A)** Paleogeographic map of the Gulf of Mexico at the end of the Cretaceous [*Blakey*, 2011], illustrating thickness and paleogeographic setting of known KPBD locales in the circum–Gulf region. **(B)** Schematic lithologic sections of the KPBD by distance from the crater. Change in composition and thickness of the KPBD with proximity to the crater strongly suggests a genetic link between the two. The locations of Cuban outcrops in **(A)** are repositioned relative to the paleolocation of Cuba; all other outcrops are displayed in their modern location. Note that the Mississippi Embayment at the end of the Cretaceous likely extended considerably northward of the limit depicted by *Blakey* [2011] (short-dashed line) in **(A)**, as indicated by megatsunamigenic KPBDs in Missouri [*Campbell et al.*, 2007; *Frederiksen et al.*, 1982]. Cantarell is a supergiant oil field in which fractured KPBD comprises the primary reservoir [*Cantu-Chapa and Landeros-Flores*, 2001; *Grajales-Nishimura et al.*, 2000; *Ricoy-Paramo*, 2005]. Gray lines in **(A)** indicate coastline and administrative boundaries, and gray dashed lines indicate radial distance from the crater. KBPD outcrop and core locations and thicknesses are from various sources, counter-clockwise from northeast: Braggs, Mussel Creek, and Moscow Landing [*Hart et al.*, 2013]; Shell Creek [*King and Petruny*, 2007]; Brazos [*Yancey*, 1996; *Yancey and Liu*, 2013]; El Tecolete [*Soria et al.*, 2001]; El Peñón [*Stinnesbeck et al.*, 1993]; Lajilla, El Mimbral, La Ceiba, and Coxquihui [*Smit et al.*, 1996]; Bochil and Guayal [*Grajales-Nishimura et al.*, 2000]; Cantarell [*Cantu-Chapa and Landeros-Flores*, 2001]; Albion Island [*Ocampo et al.*, 1996]; Armenia [*Pope et al.*, 2005]; Actela [*Fourcade et al.*, 1998]; Moncada [*Tada et al.*, 2002]; Cacarajicara [*Tada et al.*, 2003]; and Peñalver [*Kiyokawa et al.*, 2002]. **(B)** is modified from *Schulte et al.* [2010]. See Table A1 in Appendix 1 for data from **(A)** in tabular form.

Chapter 2: Materials and methods

SEISMIC DATA

We relied primarily on seismic stratigraphic interpretation of regional depth-converted two-dimensional seismic reflection data in order to map the KPBD in the northern Gulf of Mexico (Figure 2). In total, we used over 210,000 km of depth-converted two-dimensional seismic data from four regional industry datasets and ~9,000 km^2 of high-resolution depth-converted three-dimensional seismic reflection data from one industry dataset (Figure 2). Additionally, we used two-dimensional data from two academic seismic reflection surveys for mapping of the KPBD on the northwestern Yucatán Platform. We depth-converted the original time data from these surveys for this study using velocity models produced by *G L Christeson et al.* [2009]. Paradigm Focus seismic processing software was used for depth-conversion. Finally, we utilized two-dimensional seismic reflection time data from multiple academic surveys to supplement interpretations of depth-converted data. These data were particularly valuable as they allowed correlation of the KPBD from the Chicxulub impact basin to the northern Gulf (Figure 2). Detailed information on various sources for seismic data are tabulated in Table A4 of Appendix 1. We refer the reader to the Seismic Data Center (SDC) at UTIG for more information regarding all academic seismic data used for this study [*Shipley et al.*, 2013].

SEISMIC INTERPRETATION METHODS

We relied primarily on seismic stratigraphic interpretation methods [e.g., *Sheriff*, 1980; *Snedden and Sarg*, 2008; *Vail*, 1987] in order to map the KPBD on regional seismic data. The principles of sequence stratigraphy [e.g., *Van Wagoner*, 1988] were employed wherever beneficial, particularly where correlation of sub- and superjacent stratigraphy facilitated mapping of the KPBD. Recognition of seismic facies and stratal relationships is critical for mapping the KPBD throughout the northern Gulf. To that end, a number of seismic facies were identified,

revealing that the seismic character of the deposit varies significantly throughout the study area while maintaining key diagnostic features (Figure 3). Primary criteria for recognition of the KPBD in seismic data are a uniform, high-amplitude peak-trough-peak response (a single peak when erosional) and subjacent stratal truncation (Figure 3A–C). In shelf- and platform-proximal areas, diagnostic criteria for mounding or slumping of the KPBD include low-amplitude, chaotic or discontinuous internal character bounded by high-amplitude events (Figure 3D–F).

Salt tectonics within the Louann salt basin (terminology of *Hudec et al.* [2013a]) can result in duplicate, out-of-place, or absent strata and thus require a mapping methodology that accounts for such cases. For instance, while the KPBD is typically located within primary (i.e., subsalt) basins, there exist areas where the KPBD is locally rafted with bounding strata via salt migration, resulting in out-of-place "carapaced" sections within secondary (i.e., suprasalt) basins that are unrepresentative of regional trends and controls on KPBD deposition. As such, the KPBD where carapaced was omitted from regional mapping. Additionally, the KPBD is absent in areas where salt stocks or roots are present (between individual primary basins), but given the scale of mapping for this study, coupled with the difficulty of resolving such areas on narrow-azimuth two-dimensional seismic reflection data, the KPBD was mapped as continuous across primary basins throughout the Louann salt basin.

Where the KPBD is too thin for crustal-scale vertical seismic resolution (e.g., Florida Platform and upper Texas shelf), we approximated KPBD thicknesses documented in borehole data by picking the base of the deposit on the first negative amplitude event below the positive amplitude event (i.e., peak) picked as the top of the deposit. We acknowledge the geophysical shortcomings of such a method, but deem it suitable in order to map the KPBD on seismic data within these locales without the need to correct for exaggerated thicknesses.

Within the Chicxulub impact basin, we consider the KPBD to be equivalent to the "impact breccia", "suevitic breccia", or "suevite" of previous investigators of geophysical and borehole data at the crater [*Sharpton et al.*, 1994; *Sharpton et al.*, 1996; *W C Ward et al.*, 1995]. The rationale for this definition is seismic-, litho-, and chronostratigraphic: (1) it differentiates clastic brecciation (with some melting) above from shock-melting below, thus isolating the deposit most analogous to the KPBD elsewhere in the Gulf; (2) it coincides with a chronostratigraphic boundary that represents a transition from crater formation to debris deposition as the crater took its final form; and (3) the KPBD mapped throughout the Gulf, outside of the impact basin, is a clastic impact-related unit rather than an impactite, *sensu stricto*; and (4) it facilitates seismic interpretation, as this unit is a chaotic to semicoherent package bounded below by a generally well-resolved, broad-wavelength, high-amplitude peak that separates it from an incoherent section that extends downward indeterminately within the impact basin (Figure 4). While both the contact and the genetic processes are gradational, borehole and seismic data justify this distinction, as all boreholes within the impact basin penetrate clastic breccia overlying melt breccia and melt, and the contact between the two units correlates to the broad-wavelength peak consistently observed in seismic data (Figure 4).

BOREHOLE DATA

We utilized 408 wells penetrating the Cretaceous for this study: 40 deepwater (>300 m as per the Minerals Management Service (MMS)) wells, 51 shallow-water (<300 m) wells in federal waters, and 317 onshore and shallow-water wells in state waters (Figure 2) [*Richardson et al.*, 2008]. Of the 40 deepwater Cretaceous wells, seven penetrate the KPBD within a salt-related carapace and eight only partially penetrate the KPBD (typically logging <50 m of Cretaceous section), one of which is within a carapace. As with seismic data, we exluded wells

containing carapaced KPBD from regional structure and thickness mapping as they are stratigraphically and geographically out of place. Additionally, because partial penetrations do not log the base of the KPBD, they were not used for thickness mapping. In total, we used 401 wells for structure mapping and 393 wells for thickness mapping.

The majority of biostratigraphic and petrophysical data for wells utilized in this study were released by the U.S. Bureau of Ocean Energy Management (BOEM). In some cases, biostratigraphic data have been reinterpreted by Paleo-Data, Inc. (PDI), a micropaleontological firm and third-party sponsor of the Gulf Basin Depositional Synthesis Project (GBDS).

While cores of the KPBD in the deepwater Gulf of Mexico are extremely rare, those that exist are critical to assessing the sedimentology and depositional processes of the KPBD. Leg 77 of the Deep Sea Drilling Project (DSDP) acquired core at four sites (536–538 and 540) in the southeastern Gulf of Mexico that contain the KPBD [*Buffler et al.*, 1984; *Watkins and McNulty*, 1984].

During Leg 10 of the DSDP, conducted seven years prior to Leg 77, cores containing Cretaceous sediments were acquired at four sites (86, 94, 95, and 97) in the southern Gulf of Mexico [*Worzel et al.*, 1970]. While the majority of these cores are interpreted to contain only Early Cretaceous sediments, core from Site 97 in the southeastern Gulf (adjacent to Leg 77 sites) possibly contains the KPBD [*Smith and McNeely*, 1970].

BOREHOLE DATA INTERPRETATION METHODS

We employed borehole wireline, biostratigraphic, and lithologic data wherever available to corroborate seismic interpretation and reduce seismic data gaps for mapping. The KPBD is remarkably consistent in petrophysical character throughout the Gulf and generally exhibits a blocky signature of low gamma ray counts, neutron-porosity, and bulk density, and high

resistivity relative to bounding strata (Figure 5). Often, gamma ray counts increase slightly upward, while resistivity decreases slightly, interpreted to represent the upward-fining lithology of the deposit, as observed in cores at DSDP Leg 77. On the Florida Platform, the KPBD thins to <30 m, exhibits a slightly less "clean" log signature, and is often difficult to distinguish from over- and underlying platform carbonates. Furthermore, onshore wells generally contain a significantly thinner KPBD (often <10–15 m), though it exhibits similar low gamma ray counts and high resistivity. High compressional acoustic velocity relative to superjacent shales and subjacent marls results in a high impedance contrast, corroborating regional seismic identification of the KPBD (Figures 4 and 6).

Where available, we used biostratigraphic data to guide wireline log interpretation or confirm the position of the KPBD. The KPBD in the deep water generally exhibits the characteristic K-Pg "boundary cocktail", a mixture of reworked nannofossils and foraminifera first described by *Bralower et al.* [1998], as the work of *Denne et al.* [2013] recently confirmed.

Over the course of June 17 and 18, 2013, we evaluated and described cores from DSDP Leg 77 at the Texas A&M IODP Gulf Coast Repository (GCR) in College Station, Texas. Visual and microscopic core description was performed on cores from sites 536–538 and 540 of Leg 77, guided by interpretations made by *W Alvarez et al.* [1992] and *Bralower et al.* [1998].

MAPPING METHODS

We used Landmark DecisionSpace Desktop for seismic and borehole data interpretation and grid generation. We then imported the resultant grids into ArcGIS for minor processing, contouring, and volumetric calculation. We calculated KPBD volume from the interval thickness map produced from seismic and borehole mapping. To do so, we used the Zonal Statistics tool in ArcMap to tabulate map cell–based thicknesses, from which we calculated average thickness.

We then multiplied average thickness by the map area to determine total volume for the northern Gulf. Finally, we calculated KPBD in the southern Gulf by extrapolating the average thickness from the northern Gulf and multiplying it by the area of the southern Gulf based on the Cretaceous-Tertiary North American paleogeographic map of [*Blakey*, 2011]. We refer the reader to Appendix A1 for a detailed methodology of mapping and volumetric calculation.

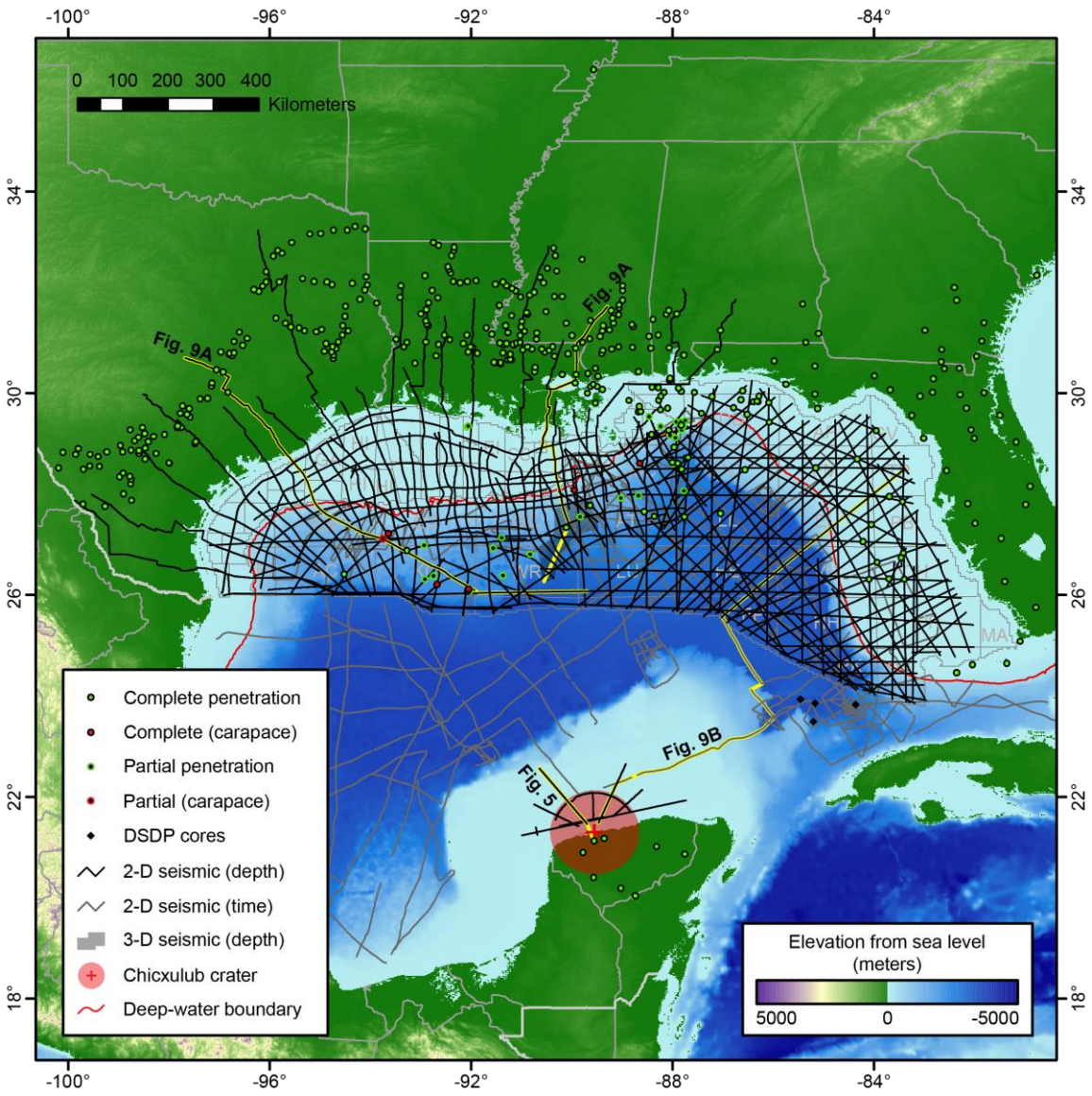

Figure 2: Study area and data extent in the Gulf of Mexico. The red 300 m bathymetric contour line throughout the northern Gulf demarcates deep- and shallow-water provinces, as per *Richardson et al.* [2008]. Yellow highlights indicate lines displayed in Figures 5 and 9A–C. See section 2.2 for an explanation of the types of penetrations (i.e., complete vs. partial, conventional vs. carapace). Fugro DeepFocus dataset not displayed.

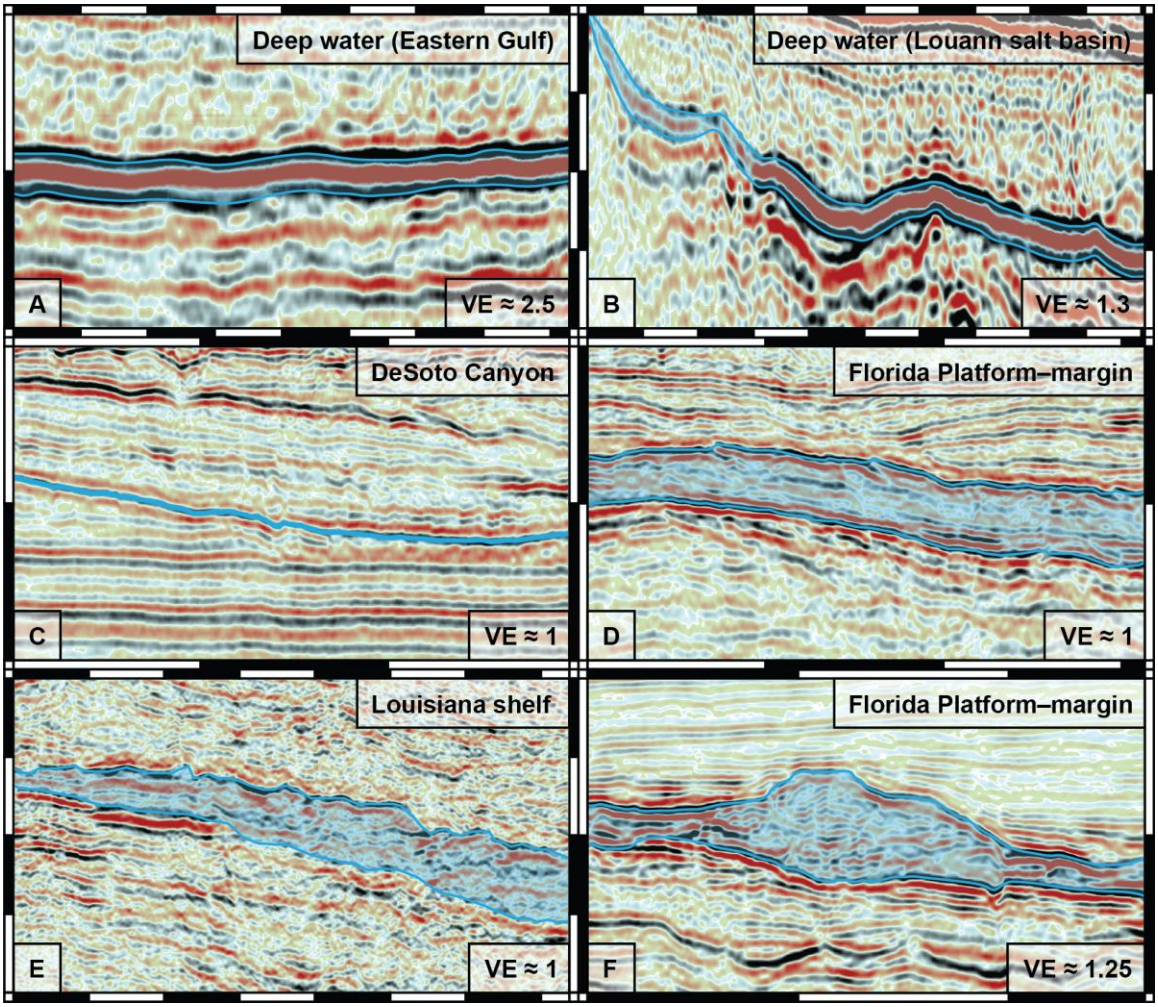

Figure 3: Seismic facies of the K-Pg KPBD in the Gulf of Mexico, with representative localities annotated. **(A)** Characteristic "blanket" facies in the deepwater Gulf, where not occluded by overlying salt or complicated by interacting salt: top and base are both defined by high-amplitude peaks, and the internal character is a uniform, high-amplitude trough; subtle subjacent stratal truncation (small red arrows). **(B)** Similar to **(A)**, but with more severe truncation of subjacent strata and thinning onto adjacent salt ridge (large arrow). **(C)** Erosional facies: severe truncation of underlying strata (small red arrows) and conformable overlying strata; KPBD is either virtually nonexistent or below seismic resolution, and boundary "surface" is defined by a high-amplitude peak. **(D)** moderate- to low-amplitude discontinuous seismic facies: generally discontinuous internal character with subtle horizontal and dipping reflectors bounded by high-amplitude peaks **(E)** Chaotic slump facies on the Louisiana shelf: tabular, internally chaotic package bounded by high-amplitude peaks. **(F)** Variable-amplitude slump facies adjacent to the Florida Platform: mounded, internally chaotic package bounded by high-amplitude peaks; onlapping superjacent strata. Scale interval is 1 km; vertical exaggeration (VE) annotated.

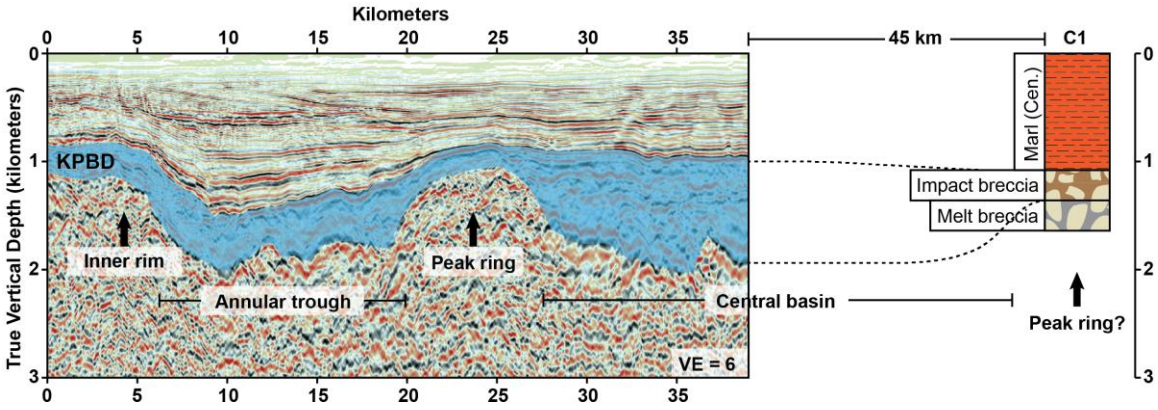

Figure 4: Segment of line CHICX-B from the 1996 Chicxulub survey demonstrating seismic facies of the KPBD at the crater, as well as crater morphology. The seismic response of the KPBD is characterized by a low- to moderate-amplitude, chaotic to semi-coherent seismic package bounded by upper short- and lower broad-wavelength peak. C1 is the Chicxulub 1 borehole, the nearest borehole to the center of the crater [*Sharpton et al.*, 1994; *Sharpton et al.*, 1996; *W C Ward et al.*, 1995]. Note that the KPBD, as defined in this study, includes only the clastic breccia ("impact breccia", "suevitic breccia", or "suevite") that overlies the crater, and not the underlying melt breccia, melt, and peak ring (of unknown lithology; see section 2.2 for explanation). Red arrows indicate onlap of Cenozoic strata. Vertical exaggeration (VE) annotated. Interpretation of the C1 borehole is modified from various authors [*Sharpton et al.*, 1994; *Sharpton et al.*, 1996; *W C Ward et al.*, 1995].

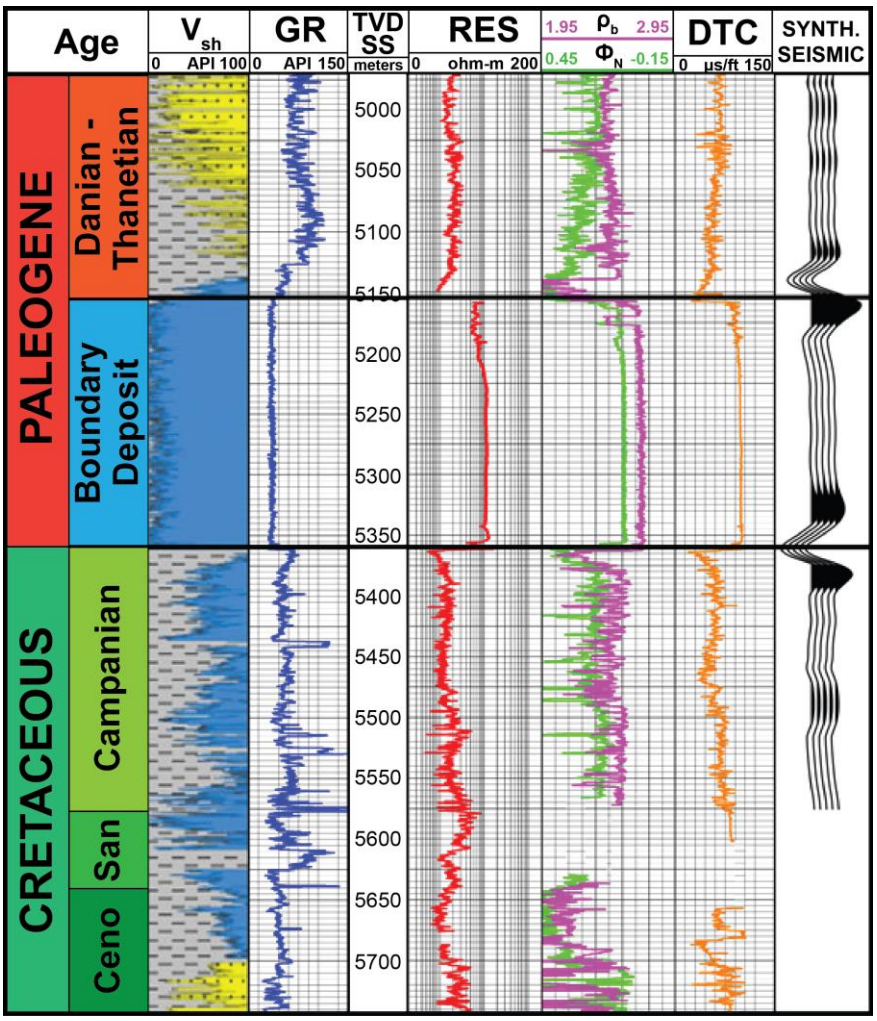

Figure 5: Type log of the KPBD in the deepwater Gulf of Mexico, demonstrating its characteristic signature: blocky with low gamma-ray counts (GR), high-resistivity (RES), low neutron-porosity (Φ_N) and bulk-density (ρ_b), and high compressional acoustic velocity (DTC). Depth in true vertical meters below sea level (TVDSS). Shale volume (V_{sh}), synthetic seismic, and biostratigraphic ages are modified from *Denne et al.* [2013].

Chapter 3: Results

STRUCTURE AND DISTRIBUTION OF THE BOUNDARY DEPOSIT IN THE NORTHERN GULF OF MEXICO

Structure at the top of the KPBD in the northern Gulf of Mexico illustrates several regional features inherited from basement and salt-tectonic features and indicates possible structural controls on deposition (Figures 7 and 8). In particular, drastic variation in structure in the Louann salt basin suggests complicated salt dynamics, though detailed inspection is required to obtain a sense of timing. Furthermore, DeSoto Canyon, likely an area of focused erosion during generation and deposition of KPBD sediment [*Denne and Blanchard*, 2013], exhibits a subtle regional expression on the northwest margin of the Florida Platform. Other regional features evident in the structure at the top of the KPBD are the Mississippi Salt Basin and the San Marcos Arch, both crustal features interpreted by several authors to have formed during opening of the Gulf of Mexico (Figures 9A and B) [*Buffler*, 1991; *Salvador*, 1991; *Sawyer et al.*, 1991].

Furthermore, thickness of the KPBD throughout the Gulf suggests several unique sediment sources and depositional processes and pathways (Figure 7). Local areas of thick KPBD on the north and northwestern shelf indicate areas of isolated slumping. Similarly, local thickening along the base of the Florida Platform suggests extensive platform collapse, whereas the rest of the eastern deep water indicates uniform KPBD thickness. The Florida Platform itself appears to have been an area of net erosion; in particular, DeSoto Canyon, on the northwestern margin of the Platform, appears to have sustained focused erosion and been a point source for deepwater deposition (Figure 7). The Louann salt basin appears to have been a regional sink for sediment mobilized by the impact. Finally, intrabasinal thickness trends suggest regional salt-tectonic and basement control on deposition, while considerable local variation within individual

provinces of the salt basin indicates the complex history of salt deformation and its syn- and postdepositional impact on the KPBD. Herein, "syndepositional" and "postdepositional" refer exclusively to timing relative to KPBD deposition.

Gulf of Mexico paleoshelf

In the western coastal region of the Gulf, the KPBD exhibits considerable change in structure and thickness due to a variety of factors (Figures 7–8 and 9A). On the upper Texas shelf, the KPBD is a net-erosional feature (particularly on the San Marcos Arch), but transitions quickly into a thick (200–300 m) deposit on the lower Texas shelf, where listric faulting in the Gulf-rim fault zone (terminology of *Klitgord and Schouten* [1986]) strongly affects structure, but not thickness, of the deposit. Where salt interacts with the deposit on the lower Texas shelf, structure varies dramatically as a result of folding, and is occasionally interrupted by isolated salt stocks.

In the northern coastal region, the Mississippi Embayment is a prominent feature, with the KPBD extending several hundred kilometers northward into the boot-heel of modern-day Missouri [*Campbell et al.*, 2007; *Frederiksen et al.*, 1982]. South of the Embayment, on the upper Mississippi and Louisiana shelf, the Mississippi salt basin is a regional basement low apparent in cross section, though the deposit appears to preserve only a subtle expression thereof (Figure 7 and 9B). However, the salt basin appears to have had little influence on boundary unit thickness aside from that of salt diapirs, suggesting that it was almost entirely infilled by post-Callovian and Cretaceous sediments at the time of impact (Figure 7 and 9B). In the lower Louisiana, Mississippi, and Alabama shelf, faults within the Gulf-rim fault zone increasingly interact with the KPBD, but are rarely accompanied by thinning of the boundary unit, suggesting predominately postdepositional deformation (Figure 7 and 9B).

The eastern coastal region is unique in the Gulf of Mexico as a result of the Florida Platform, a prominent and long-lived carbonate platform that has been a province of sustained carbonate sedimentation since the Late Jurassic [*T M Scott and Anderson*, 2001]. While the carbonate platform is generally uniform in structure, several regional features were inherited by the underlying rifted continental basement blocks, including the northeast Gulf basin (DeSoto Canyon area) and the Tampa embayment [*Ewing*, 1991; *Marton and Buffler*, 1999; *Pindell*, 1993]. However, most of these features are only subtly expressed in the structure of the KPBD (Figure 6).

An interesting feature of the structure of the boundary unit is a northeasterly embayment in central Florida, suggesting the possibility of a local or regional waterway to the Atlantic north of the Florida Straits (Figure 6). While the majority of Florida was likely at least partially inundated at the end of the Cretaceous (see Figure 1) [*Miller et al.*, 2010; *Phelps*, 2012; *Sahagian et al.*, 1996; *Vail and Mitchum*, 1979], providing a general northeasterly outlet for wave energy initiated by the impact, a local depression in the Florida peninsular arch could have further reduced wave reflection and refraction from the Florida coast.

Interval thickness of the KPBD on the Florida Platform indicates a minor thickening trend along the Florida coast (Figure 7). The deposit thickens to roughly 100 meters in this area from 0 meters up-slope (on the Florida coast) and 25 to 50 meters down-slope (on the platform). This trend suggests that the Florida coast was a minor line source for sediment deposited on the platform after impact. Furthermore, comparison of this trend to the dominant trend of thick deposits on the lower Texas shelf may suggest that the Florida coast was a more significant source of sediment, but that the majority of this sediment was carried down-slope, possibly propelled from the platform by sediment gravity flows initiated by impact-related processes.

Denne and Blanchard [2013] recently published evidence of focused collapse and erosion occurring in the DeSoto Canyon as a result of the Chixculub impact. Distribution of the KPBD indicates that an 80,000 km^2 region immediately southeast of the DeSoto Canyon in the central Gulf accumulated the thickest deposits (~300 m on average) and suggests a point source from the DeSoto Canyon to the northeast (Figure 7). While this regional trend in thickness likely represents a number of factors, including it likely being a paleo-low and regional sink to sediment throughout the Gulf, the trend suggests that the Desoto Canyon was an area of focused erosion that channeled sediments seaward from the northeastern Gulf coast and shelf.

Louann salt basin (western/central deepwater Gulf)

Generally, the most salient aspect of the structure of the boundary unit is its unique structural style within the Louann salt basin. Across the Sigsbee Escarpment, the KPBD (and primary basin stratigraphy, generally) deepens significantly, plunging from ~11 km below sea level (bsl) to over 15 km in areas. Within the salt basin, structural style appears to be divisible into eastern and western provinces (Figure 6) on the basis of both regional and local trends in structure. This division roughly coincides in the northern salt basin with the location of the seaward extension of the Brazos transform fault originally proposed by *Simmons* [1992] and recently substantiated by *Hudec et al.* [2013a]; [*Hudec et al.*, 2013l]. In the southern salt basin, this division coincides with limit of oceanic crust (LOC) proposed by *Hudec et al.* [2013a]; [*Hudec et al.*, 2013l].

In the western province of the Louann salt basin, the KPBD is generally elevated relative to the eastern province by approximately 2–4 km and thus represents a regional plateau, with relatively minor local variation in structure reflecting folding with ~1–3 km wavelengths within an area of isolated salt stocks and welds analogous to the Mississippi Canyon disconnected salt-stock-canopy province of *Pilcher et al.* [2011] (Figure 8A). Eastward within this western

province, isolated salt stocks amalgamate as volume of the para-autochthonous salt increases, resulting in a province of amalgamated canopies, likely with individual local feeders as per the amalgamated salt-stock-canopy province of *Pilcher et al.* [2011]. Within primary basins below these amalgamated canopies, the KPBD is generally isopachous, though structurally complex as a result of postdepositional salt-tectonic deformation.

The postdepositional influence of the Perdido fold belt on the KPBD in southwestern Alaminos Canyon is evident (Figure 6). The relatively isopachous nature of the deposit in the fold belt (Figure 7 and 9A) suggests that compression responsible for the belt postdates KPBD emplacement, in agreement with the common model for formation [*Fiduk et al.*, 1999; *Trudgill et al.*, 1999; *Trudgill et al.*, 1995].

In the eastern province of the Louann salt basin, the KPBD is at its deepest (generally >12 km bsl) and varies substantially in depth (± ~3 km) over relatively short distances (25–100 km) in local lows (Figure 6). To the north, this province appears to reflect coincident faulting of secondary basin (supra-salt) strata and folding of primary basin (subsalt) strata in a pillow-fold–belt style as per *Dooley et al.* [2013] (Figure 8B). While local structure varies considerably in all directions, synclinal structures in the northern half of this province exhibit a subtle east-west axis, interpreted to represent the regional trend of faulting in the Gulf-rim fault zone that is expressed in the structure of the KPBD (Figures 8B). In the south-central portion of this eastern province, localized primary basins defined to the north by salt-related faulting and folding are occasionally controlled by overlying high-angle bucket-welds as defined by [*Pilcher et al.*, 2011]. Where bucket-welds are present, underlying primary-basin strata, including the KPBD, plunge 1 to 3 km below regional depth, as a result of overburden and overburden-driven migration of autochthonous (sub-primary-basin) salt.

While the complexity of KPBD distribution within the salt basin frustrates interpretation, the characteristic variability in thickness of the KPBD within the salt basin is likely a palimpsest of syndepositional salt-topographic control and postdepositional salt movement. Both isopachous and thinning relationships of the deposit with salt are observed (Figures 4B and 9A and B). Areas where the KPBD is isopachous relative to underlying or interacting salt structures likely represent postdepositional salt movement, whereas areas of thinning of the KPBD onto adjacent salt structures (e.g., Figure 8A) indicate that these salt structures were present when the KPBD deposited and that they locally restricted deposition. Early stages of postdepositional salt movement, either in the form of upward migration of underlying salt (e.g., structures analogous to Green Knoll) or lateral compression from advancing salt (e.g., Perdido fold belt), faulted and folded an otherwise isopachous and uniform KPBD (Figure 8A and B).

Salt carapaces containing older (Paleogene to Cretaceous), typically condensed strata in the Gulf of Mexico have gained considerable interest in the last two decades as hydrocarbon exploration has revealed the complexity of salt-laden sedimentary basins [*Hudec et al.*, 2013a; *McGuinness and Hossack*, 1993; *Mount et al.*, 2007; *Pilcher et al.*, 2011]. While KPBD penetrations within carapaces were not used in regional mapping, these wells serve to illustrate the complex dynamics of the Louann salt basin through time and the resultant complexity of the province today. Sediment loading on broad, long-lived salt highs can result in condensed sections that, through time, are transported (generally seaward) as the para-autochthonous salt migrates [*Hudec et al.*, 2013a; *Pilcher et al.*, 2011]. Eventually, the host salt body evolves into an allochthonous canopy with an overlying secondary basin containing the condensed section and an underlying primary basin containing in-place strata of the same age. As a result, certain boreholes exhibit anomalous stratigraphy, in which relatively old strata are penetrated at shallow

depths (typically ~3–4 km bsl) prior to penetrating salt and then reencountered upon exiting salt. Carapaces containing the KPBD indicate areas where para-autochthonous proto-canopies were present at the time of KPBD deposition and subsequently rafted the KPBD and bounding strata. While the KPBD in such carapaces presumably contain a condensed clastic section and the entire suspension-settled section, it is unknown the degree to which such proto-canopies restricted KPBD deposition and resulted in a condensed KBPD.

Nine boreholes are interpreted to penetrate the KPBD within salt carapaces in the deepwater Gulf based on seismic and borehole data (Figure 2). Figure 9 illustrates a particularly spectacular example from Keathley Canyon (KC), where four wells (KC 875 #1–2 and KC 919 #1–#2) penetrate the KPBD within a horizontal distance of ~14 km. While three of these wells penetrate the KPBD at roughly 3.5 km bsl, KC 919 #2 penetrates the deposit at approximately 8.5 km bsl. Seismic data in the area of these wells reveals a complex setting in which an amalgamated salt-stock-canopy superposes carapaced Mesozoic and Cenozoic sediments, including the KPBD, high above in-place primary basin stratigraphy.

Eastern deepwater Gulf

Structure of the KPBD in the deepwater eastern Gulf of Mexico is relatively uniform, aside from the Florida escarpment (Figure 6). On the basin floor, the KPBD deepens gradually over ~600 km, from ~5 km bsl to adjacent to the Florida escarpment ~12 km bsl adjacent to the Sigsbee Escarpment. Distribution of the KPBD in the eastern Gulf of Mexico is self-evident relative to the complexity of the Louann salt basin (Figure 7). The deposit is virtually absent on the Florida Escarpment, but quickly thickens to ~100–150 m on the basin floor. Immediately adjacent to the platform (within ~25–50 km), the KPBD thickens locally in multiple areas to up to ~400 m. These local areas of thick deposit correspond to mounded, chaotic to semicoherent

seismic facies interpreted to represent slump deposits resultant from platform collapse (Figure 3D and F).

Roughly 300 km outboard of the Florida Escarpment, the KPBD exhibits a regional, linear northwest-to-southeast thickening trend that coincides directly with the margin of the extinct (~145 Ma) spreading center mapped on seismic reflection data by *Snedden et al.* [2014] and corroborated by recent seismic refraction and potential fields studies (Figure 7) [*G Christeson et al.*, 2013; *Norton et al.*, 2013]. This coincidence suggests that basement structure in the eastern deepwater Gulf had some influence in deposition of the KPBD, and that the extinct ridge was elevated relative to the surrounding seafloor at the time of deposition of the KPBD (Figure 8C). Spreading centers like that mapped in the eastern Gulf are often elevated relative to the adjacent sea floor [*Perfit and Chadwick Jr*, 1998].

STRUCTURE AND DISTRIBUTION OF THE BOUNDARY DEPOSIT AT THE CHICXULUB IMPACT BASIN

Because the KPBD immediately overlies melt breccia and melt that were created upon impact and thus comprise the uppermost section of the impact basin, the structure at the base of the KPBD can be utilized to approximate the structure of the impact basin itself (Figure 10). Structure at the base of the KPBD reveals the characteristic features of a multi-ring impact basin [*French*, 1998; *Morgan et al.*, 1997; *Sharpton et al.*, 1996]. These features include a semicircular inner rim with a diameter of ~180 km, an ~100 km diameter annular trough, an ~60–70 km-diameter peak ring, and an inner central basin.

In addition to revealing crater morphology, the structure at the base of the KPBD suggests that several paleotopographic features were present at the site of the impact, at least one of which likely had a significant role in post-impact deposition (Figure 10). To the east, south, and west, a semicircular structural high greater than 200 km in diameter is likely a composite

feature resultant from pre-impact structure and imprinted crater morphology. However, a significant embayment to the northeast, referred to herein as the Chicxulub embayment, appears to be a significant paleostructural feature that was present at the time of impact, as has been suggested by *Gulick et al.* [2008]. The existence of this paleo-low at the time of impact likely had important implications for postimpact deposition of ejecta and mass flows at and near the impact basin, providing a sediment evacuation route to the northeast (Figure 10).

Interval thickness of the KPBD within the impact basin also suggests that crater morphology was a control on sediment distribution in the wake of the impact (Figure 11). Generally, the deposit thins over the peak ring and thickens within the central basin and annular trough. The thickest deposits are within the central basin, where they approach 1 km in thickness. To the northwest, deposit thickness increases relative to the rest of the impact basin, suggesting that the Chicxulub embayment did facilitate the evacuation of sediment to the deep water in a dominantly northeasterly direction, though differences in accommodation space within the crater may also have played a role (Figure 11). Distribution of the KPBD within and surrounding the impact basin is particularly important in that it established the paleotopography that likely was the foundation for early Cenozoic carbonate system recovery on the Yucatán Platform as reported by *Whalen et al.* [2013].

SEDIMENTOLOGY OF THE BOUNDARY DEPOSIT IN THE SOUTHEASTERN GULF OF MEXICO

Four cores acquired during DSDP leg 77 in the southeastern Gulf (Figures 2 and 3) provide important insight into the sedimentology and depositional processes of the KPBD. Together, sites 536 and 540 are interpreted to span a nearly complete section of the KPBD, after *W Alvarez et al.* [1992] and *Bralower et al.* [1998]. At these sites, the KPBD consists of an ~50 m interval of predominately sediment gravity flows and can be divided into six facies (Figure 12

and Table 3). These facies and their interpreted depositional mode are: a thick (~40 m) basal unit of poorly-sorted pebbly mudstones with scattered cobble- and boulder-sized blocks, interpreted to have resulted from one or more muddy debris flows with entrained slump blocks; a middle (~10 m) unit comprised of at least five sequences of generally upward-fining carbonate sandstones to mudstones, interpreted to represent deposition by successive turbidity currents; and a thin (~0.5 m) upper unit of massive carbonate mudstone with iridium enrichment measured by *W Alvarez et al.* [1992], interpreted to represent deposition of resuspended carbonate mud and silt- to clay-sized ejecta in the early Danian and resulting in the highest concentration of iridium. Detailed core descriptions of sites 536 and 540 are presented in Figures S1 and S2 of the supplementary information for this publication.

This sedimentary succession is interpreted to be analogous to deepwater deposits throughout the deepwater Gulf of Mexico. The ~50 m condensed section observed at these core sites relative to typical deepwater deposits (>100 m) observed in borehole and seismic data is explained in two ways: (1) the sites were likely in a platform-marginal paleoenvironment without severe adjacent bathymetric relief relative to Florida Platform–marginal areas (Figure 1); (2) the sites are interpreted to have been on high-standing basement blocks, and thus likely represented areas of condensed deposition. This latter characteristic is supported by seismic data and made the sites ideal candidates for drilling into Paleozoic basement [*Buffler et al.*, 1984].

Furthermore, based on the thickness and lower stratigraphic position of the muddy debrite part of the section, debris flow is interpreted to have been the first and primary mechanism of transport in the Gulf of Mexico in the wake of the impact. Furthermore, turbidity currents are interpreted to have been a significant contributor to the deposit in platform- and shelf-marginal settings, whereas deepwater deposits are speculated to consist mostly or entirely

of muddy debrites, as is consistent with the typical well-log character and cuttings descriptions (Figure 5). Finally, the thin mudstone unit that "caps" the KPBD is interpreted to have draped the entire Gulf in the wake of the impact, and is analogous to the global boundary clay or "fireball layer" of *Hildebrand and Boynton* [1990]. Thus this mudstone layer is speculated to be virtually ubiquitous in the Gulf. The fact that this layer is thicker than the global boundary clay (~0.5 m vs. <1 cm) is explained by the marine setting and proximity of the Gulf basin to the site of the impact, resulting in a large volume of resuspended carbonate mud that would have deposited within the same time frame as the finest fraction of iridium-enriched dust.

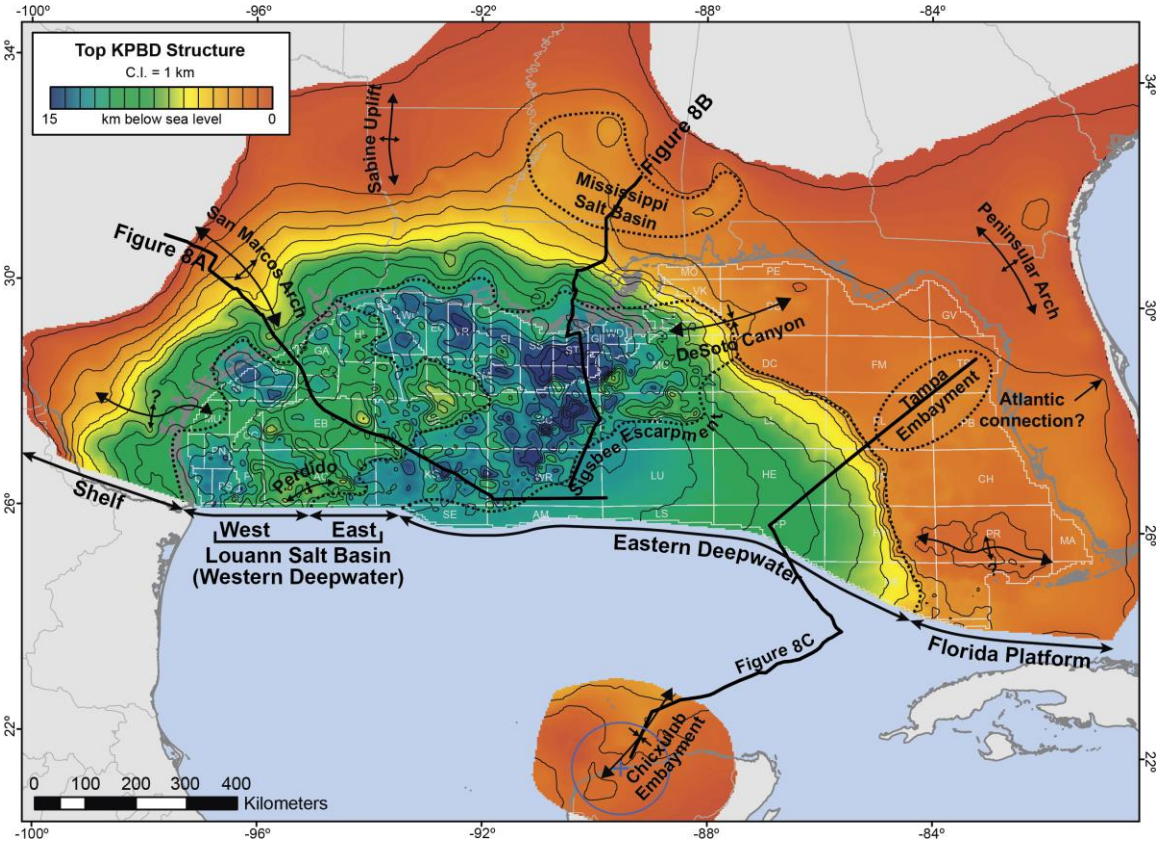

Figure 6: Structure at the top of the KPBD in the northern Gulf of Mexico, illustrating regional structural features and extreme local variation in structure within the Louann salt basin. Dashed black lines indicate the boundaries of key structural features, and dashed red lines indicate boundaries of salt provinces. Location of seismic transects in Figure 8 are indicated by blue lines.

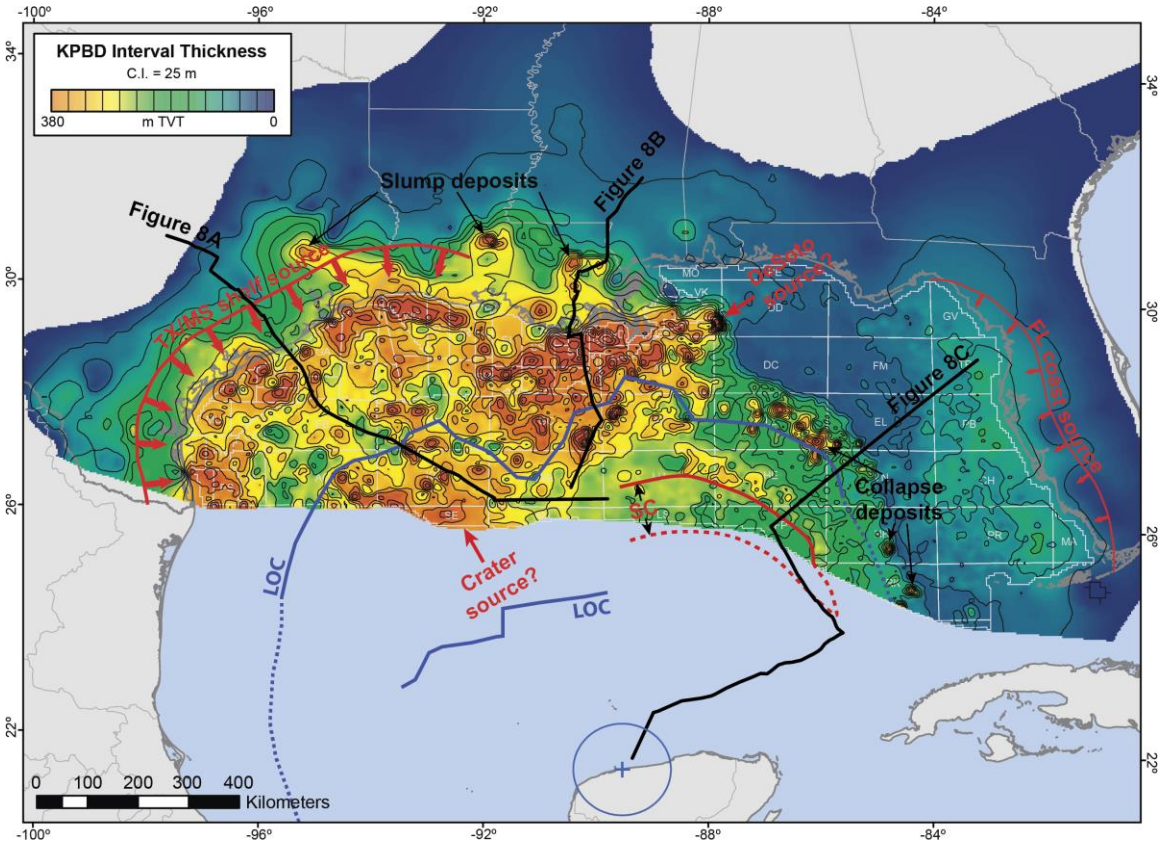

Figure 7: Interval thickness of the KPBD in the northern Gulf of Mexico, suggesting local basement and salt control. Individual and connected red arrows indicate point and line sources, respectively. SC = extinct spreading center mapped by *Snedden et al.* [2014] on (solid) and speculated from (dashed) seismic data. LOC = limit of oceanic crust per *Hudec et al.* [2013a]; [*Hudec et al.*, 2013l]. Location of seismic transects in Figure 8 are indicated by black lines.

Figure 8

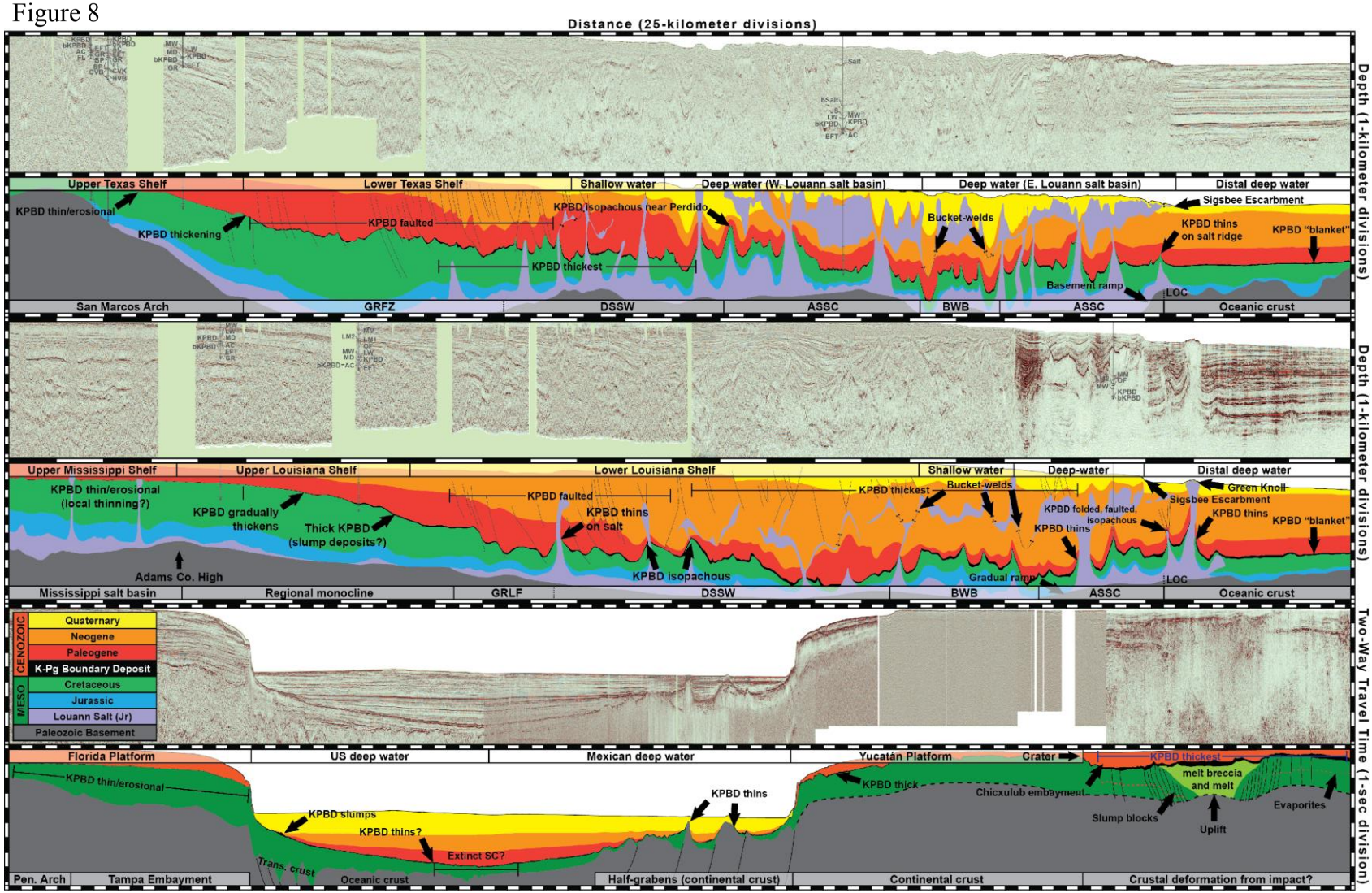
Distance (25-kilometer divisions)
Depth (1-kilometer divisions)
Upper Texas Shelf
Lower Texas Shelf
Shallow water
Deep water (W. Louann salt basin)
Deep water (E. Louann salt basin)
Distal deep water
KPBD thin/erosional
KPBD thickening
KPBD faulted
KPBD isopachous near Perdido
KPBD thickest
Bucket-welds
Sigsbee Escarbment
KPBD thins on salt ridge
KPBD "blanket"
Basement ramp
LOC
San Marcos Arch
GRFZ
DSSW
ASSC
BWB
ASSC
Oceanic crust
Depth (1-kilometer divisions)
Upper Mississippi Shelf
Upper Louisiana Shelf
Lower Louisiana Shelf
Shallow water
Deep-water
Distal deep water
KPBD thin/erosional (local thinning?)
KPBD gradually thickens
Thick KPBD (slump deposits?)
KPBD faulted
KPBD thins on salt
KPBD thickest
Bucket-welds
Green Knoll
Sigsbee Escarbment
KPBD folded, faulted, isopachous
KPBD thins
KPBD thins
KPBD "blanket"
Adams Co. High
KPBD isopachous
Gradual ramp
LOC
Mississippi salt basin
Regional monocline
GRLF
DSSW
BWB
ASSC
Oceanic crust
CENOZOIC
Quaternary
Neogene
Paleogene
K-Pg Boundary Deposit
MESO
Cretaceous
Jurassic
Louann Salt (Jr)
Paleozoic Basement
Two-Way Travel Time (1-sec division)
Florida Platform
US deep water
Mexican deep water
Yucatán Platform
Crater
KPBD thickest
KPBD thin/erosional
KPBD slumps
KPBD thins?
Extinct SC?
KPBD thins
KPBD thick
Chicxulub embayment
melt breccia and melt
Slump blocks
Uplift
Evaporites
Pen. Arch
Tampa Embayment
Trans. crust
Oceanic crust
Half-grabens (continental crust)
Continental crust
Crustal deformation from impact?

Figure 8: Uninterpreted (top) and interpreted (below) regional seismic reflection transects through the Gulf of Mexico, illustrating KPBD thickness and structure through structural provinces in the basin. Annotations at the top and base of each interpreted section indicate geographic and structural provinces, respectively. **(A)** Northwest-southeast depth-converted transect from the San Marcos Arch on the Texas shelf to the deepwater Gulf outboard of the Sigsbee Escarpment in Keathley Canyon (KC). Wells, from west to east: G.D. Vick #1, Willie Matejcek #1, Weiting #1, KC 102 #1 (Tiber Field). **(B)** North-south depth-converted transect from the Mississippi shelf to the deepwater Gulf outboard of the Sigsbee Escarpment. Wells, from north to south: Crown Zellerbach #1, Currie #1, Green Canyon (GC) 653 #3 (Shenzi Field). **(C)** North-south time transect from the Florida Platform to the Chicxulub impact basin. Note that at the crater, the mapped KPBD consists of clastic breccia ("impact breccia", "suevitic breccia", and/or "suevite") and does not include melt or melt breccia (see section 2.2 for explanation). Seismic quality on the Yucatán Platform is noticeably diminished as a result of hard and acoustically "fast" platform carbonates that occlude underlying seismic stratigraphy. GRFZ: Gulf-rim fault zone after *Klitgord and Schouten* [1986]; DSSW: disconnected salt-stock-canopy province after *Pilcher et al.* [2011]; BWB: bucket-weld-basin province after *Pilcher et al.* [2011]; ASSC: amalgamated salt-stock-canopy province after *Pilcher et al.* [2011].

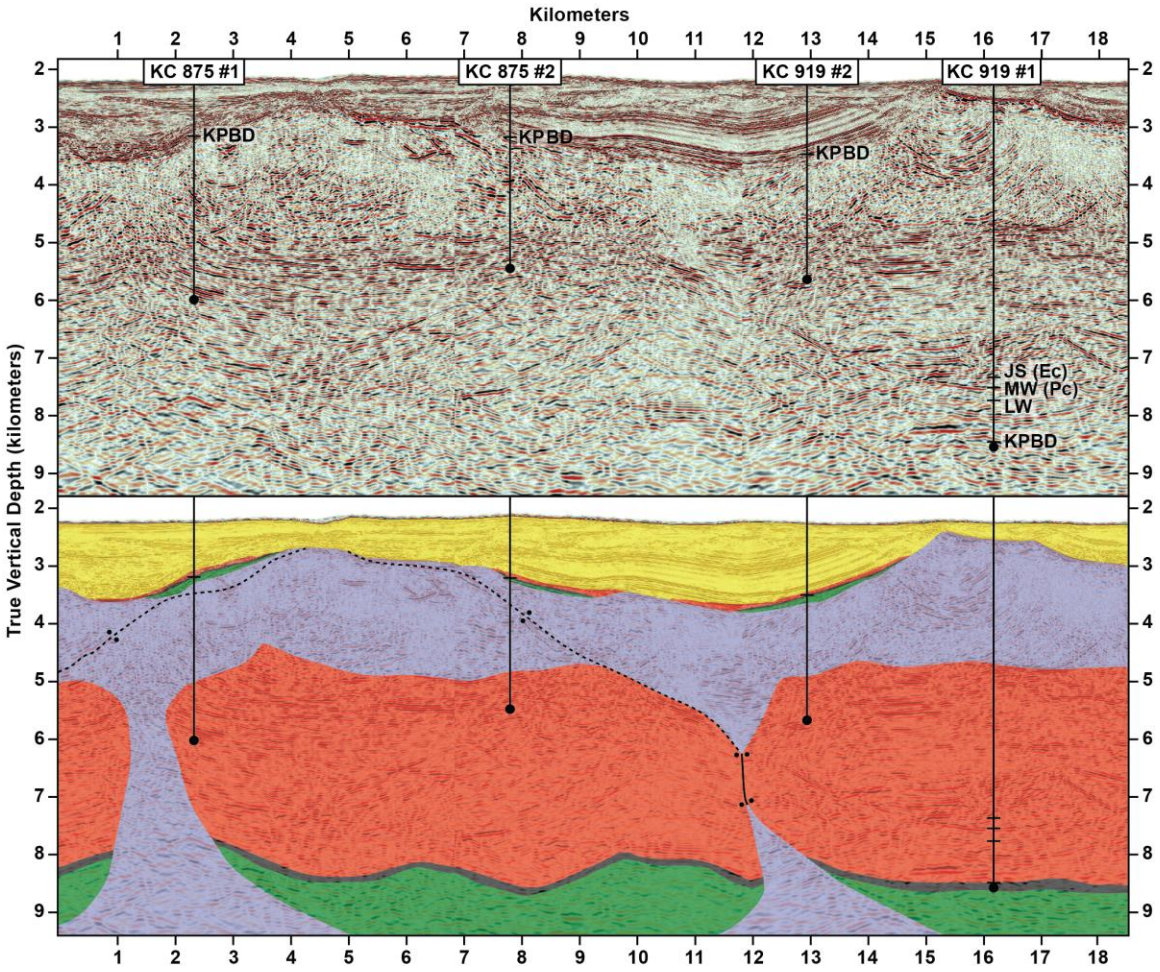

Figure 9: Uninterpreted (top) and interpreted (bottom) depth-converted seismic reflection section documenting suprasalt carapaces containing the KPBD and condensed Mesozoic and Early Cenozoic (Paleogene) strata in the Louann salt basin, Keathley Canyon (KC). As per Figure 8, purple shading indicates Callovian salt; green indicates Mesozoic (Upper Jurassic and Cretaceous) strata; black indicates KPBD; red indicates Paleogene strata; and yellow indicates secondary basin strata (Neogene and younger). Paired black circles indicate salt welds (solid line) and sutures (dashed lines). Note that the southernmost well penetrates the KPBD in-place, ~5 km below the carapaces. Wells, from north from south: KC 875 #1 and #2 (Lucius Field), KC 919 #2 and #1 (Hadrian Field).

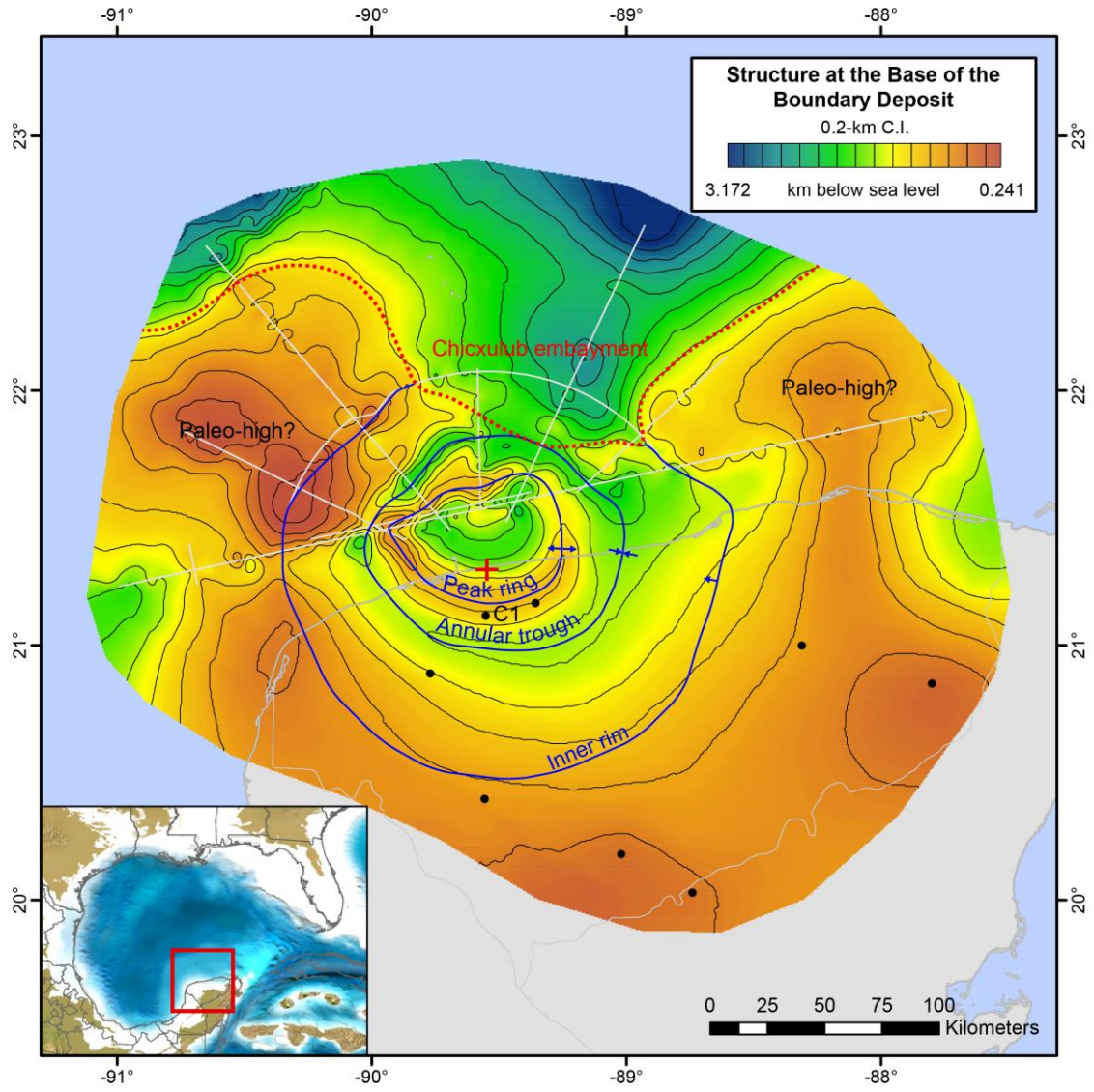

Figure 10: Structure at the base of the KPBD at the Chicxulub impact basin, illustrating crater morphology and preexisting structure. Approximate axes of the inner rim, annular trough, and peak ring are overlain in blue, and the Chicxulub embayment is indicated with a dashed red line. White lines indicate seismic control, and black circles represent borehole locations. The location of the C1 borehole is indicated (see Figures 5 and 13).

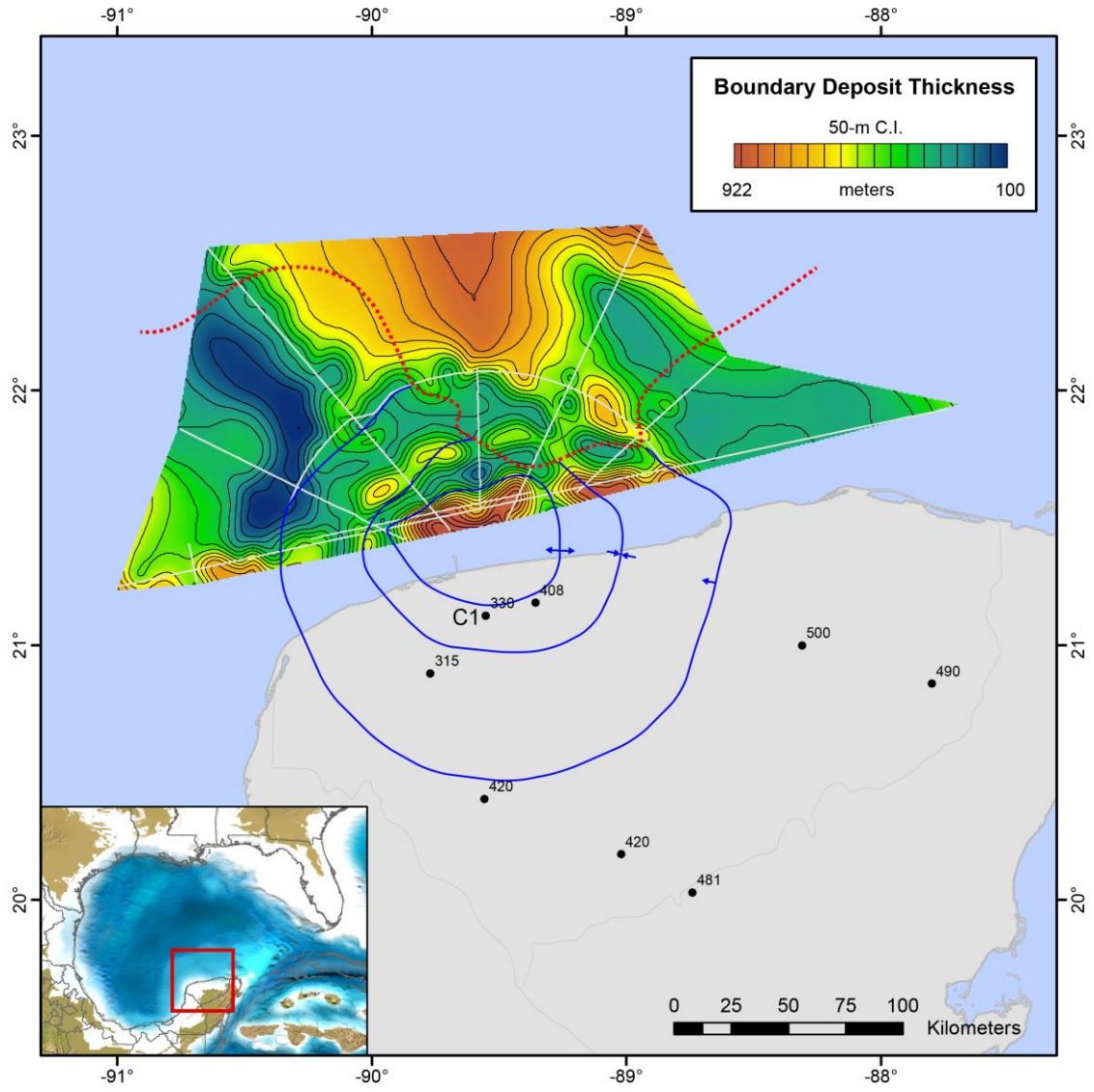

Figure 11: Interval thickness of the KPBD at the Chicxulub crater. Structural features of the crater (blue lines) and preexisting Chicxulub embayment (dashed red line) are taken from Figure 10. White lines indicate seismic control, black circles represent borehole locations, and adjacent numbers indicate KPBD thickness in boreholes. The location of the C1 borehole is indicated (see Figures 5 and 13).

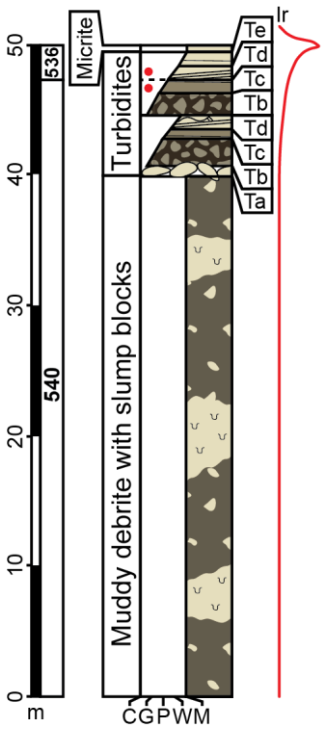

Figure 12: Idealized lithology of sites 540 and 536 cores, together interpreted to represent the entire KPBD sequence in the southeastern Gulf. The deposit can be divided into three units: poorly sorted muddy debrite, upward-fining turbidites, and massive carbonate mudstone. Red circles indicate location of spherules, and red curve at right represents idealized iridium concentration. C = cobblestone/pebblestone, G = grainstone, P = packstone, W = wackestone, M = mudstone, as per *Dunham* [1962]. See Table 1 for facies descriptions. See Appendix 2 for detailed core descriptions.

Name	Description	Interpretation
Massive mudstone	Massive cream/buff micrite; iridium enrichment reported by Alvarez *et al.* [1992]	Suspension settling
Planar-laminated mudstone	Planar-laminated to massive cream/buff mudstone to packstone	Bouma Td
Cross-bedded packstone	Greenish-gray to cream/buff planar to wavy cross-bedded packstone	Bouma Tc
Planar-laminated pebbly grainstone	Greenish-gray/brown/tan to cream/buff planar-laminated pebbly grainstone	Bouma Tb
Normal-graded pebbly grainstone	Greenish-brown to cream/buff normal-graded pebbly grainstone with smectite	Bouma Ta (Lowe S2)
Reverse-graded cobbles	Reverse-graded burrow-mottled chalk cobbles to large pebbles with little to no preserved matrix	Bouma Ta (Lowe S1)
Pebbly mudstone	Greenish-gray pebbly mudstone with unsorted floating clasts and blocks	Muddy debrite

*See Figure 12 for an idealized core interpretation and Appendices 2 and 3 for detailed core descriptions.

Table 1: KPBD facies at sites 536 and 540*

A Figure 13

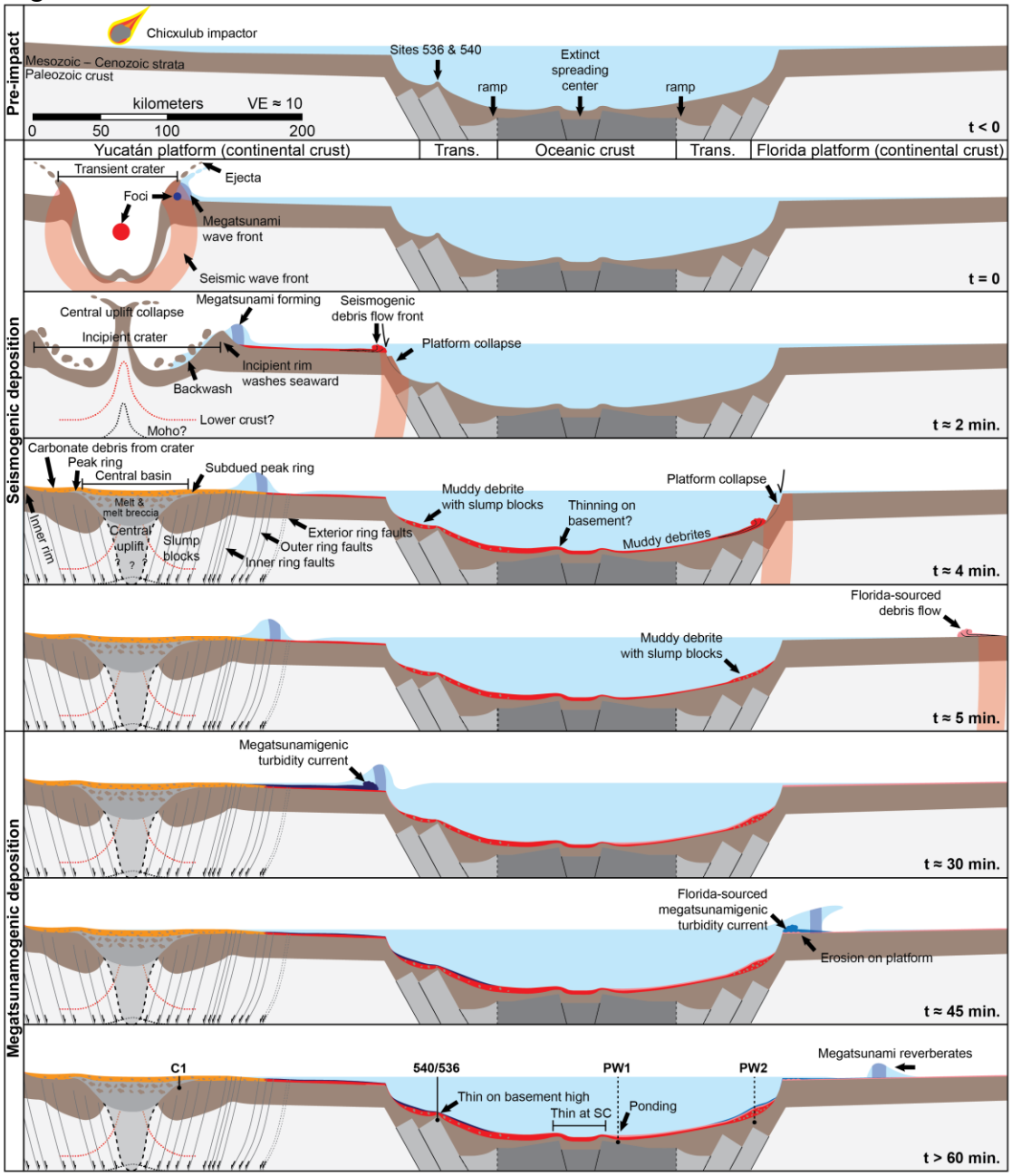
Pre-impact
Chicxulub impactor
Mesozoic – Cenozoic strata
Paleozoic crust
kilometers
VE ≈ 10
0 50 100 200
Sites 536 & 540
ramp
Extinct spreading center
ramp
t < 0
Yucatán platform (continental crust)
Trans.
Oceanic crust
Trans.
Florida platform (continental crust)
Seismogenic deposition
Transient crater
Ejecta
Foci
Megatsunami wave front
Seismic wave front
t = 0
Central uplift collapse
Incipient crater
Megatsunami forming
Seismogenic debris flow front
Platform collapse
Incipient rim washes seaward
Backwash
Moho?
Lower crust?
t ≈ 2 min.
Carbonate debris from crater
Peak ring
Central basin
Subdued peak ring
Melt & melt breccia
Inner rim
Central uplift
Slump blocks
Exterior ring faults
Outer ring faults
Inner ring faults
Muddy debrite with slump blocks
Thinning on basement?
Platform collapse
Muddy debrites
t ≈ 4 min.
Florida-sourced debris flow
Muddy debrite with slump blocks
t ≈ 5 min.
Megatsunamigenic deposition
Megatsunamigenic turbidity current
t ≈ 30 min.
Florida-sourced megatsunamigenic turbidity current
Erosion on platform
t ≈ 45 min.
C1
540/536
PW1
PW2
Megatsunami reverberates
Thin on basement high
Thin at SC
Ponding
t > 60 min.

B

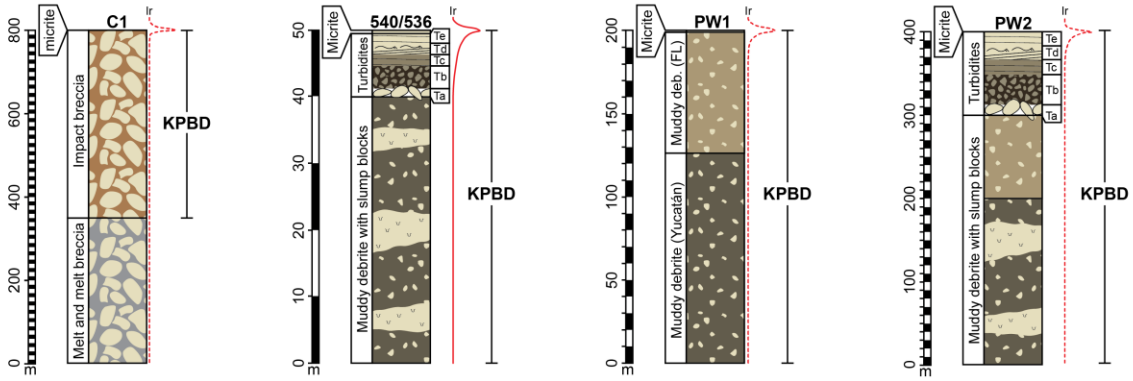
C1
micrite
Impact breccia
Melt and melt breccia
Ir
KPBD
m
540/536
Micrite
Turbidites
Muddy debrite with slump blocks
Te
Td
Tc
Tb
Ta
PW1
Muddy deb. (FL)
Muddy debrite (Yucatán)
PW2

Figure 13: Schematic model for post-impact deposition in the eastern Gulf of Mexico. The impact initiates a seismic pulse that inputs seismic energy and a megatsunami into the Gulf. As the crater is forming to the southeast, seismic ground-roll and shaking rapidly travels across the Gulf, arriving onshore Florida in about 6 minutes (see Table A1). The megatsunami wave train travels at roughly a tenth the velocity of the Rayleigh-wave-driven seismic energy, with the first wave reaching the Florida coast in about an hour and generating a separate sequence of sediment gravity flows (mostly turbidites). Note that the location of DSDP Sites 536 and 540 is a paleohigh, resulting in the relatively thin deposit (~50 m). C1 is the Chicxulub 1 borehole, the nearest borehole to the center of the impact basin [*Sharpton et al.*, 1994; *Sharpton et al.*, 1996; *W C Ward et al.*, 1995]. PW1 and PW2 are pseudowells in the deepwater eastern Gulf, indicated by dashed-line boreholes. **(B)** Schematic lithologies of the KPBD through the Gulf. The turbidite deposits in the KPBD consist of multiple turbidite sequence, derived from distinct origins (e.g., Yucatán Platform, Florida Platform) depending on location. At the impact basin, the KPBD mapped in this study includes only clastic breccia, and not underlying melt and melt breccia (see section 2.2 for an explanation). Note the scale change across wells. PW1 and PW2 lithologies are hypothesized for the pseudowell locations in **(A)**. Dashed red lines indicate hypothesized iridium curves.

Chapter 4: Discussion

REGIONAL SEDIMENT SOURCES FOR THE BOUNDARY DEPOSIT AND IMPLICATIONS FOR DEPOSITIONAL MECHANICS AND TIMING

Mapping of the KPBD in the Gulf of Mexico yields many insights regarding impact-related processes that resulted in its deposition in the wake of the Chicxulub impact. The first-order observation to be made is that the majority of sediment deposited as a result of the impact appears to have been sourced not from the impact basin, but rather from Gulf basin–proximal shelf and platform settings. In particular, the Texas and Louisiana shelf and DeSoto Canyon appear to have been significant line and point sources, respectively, for sediment generated by the impact. Furthermore, mapping and observation of seismic data in the southern Gulf suggest that the transient crater and surrounding settings (e.g., the Campeche Escarpment) were primary local sources for sediment, and perhaps exceeded sediment volumes estimated for the northern Gulf. Finally, locally elevated sediment input in basin-margin settings (e.g., the Florida Platform and Texas and Louisiana shelf–margins) appears to have derived from slump and slide deposits resultant from relatively isolated episodes of platform collapse.

The logical conclusion to be made from this first-order observation is that the primary initiators of sediment transport during deposition of the KPBD were seismic shaking and ground-roll and megatsunami wave trains, just as they were likely the two primary mechanisms for energy transfer from the impactor to the Earth. Coupling this conclusion with observations of cores of the KPBD and reasonable assumptions of seismic and tsunamic travel times, one can reconstruct the sequence and timing of KPBD deposition. Debrites, the first and most voluminous deposit, likely originated from seismic shaking and ground-roll, which would have reached the paleo–Florida and –Texas coasts within roughly seven minutes. Multiple boulders and cobbles floating in the mudstone matrix interpreted to represent muddy debrites suggest that

platform collapse likely occurred simultaneously, also triggered by seismic processes. Furthermore, the transition to turbidites observed in the upper portion of the KPBD suggests a correlative transition in triggering mechanism, and thus is speculated to represent the first arrival of the megatsunami wave train generated by the impact, which would have reached the paleo–Florida and –Texas coasts in ~75 minutes (see Table A2 in Appendix 1). Finally, the carbonate mudstone "cap" at the top of the KPBD represents a transition from catastrophic sediment gravity flows to suspended-sediment deposition through settling of both resuspended carbonate mud and the finest fraction of ejecta (silt- to mud-sized), including iridium-enriched dust. Several workers have made attempts to constrain the timing of deposition of fine-grained ejecta [e.g., *W Alvarez et al.*, 1995; *Goldin and Melosh*, 2007], the latest of which establishes a maximum of ~2 weeks for deposition by Stokesian flow [*Artemieva and Morgan*, 2009]. See Table A2 and A3 of Appendix 1 for seismic and megatsunami wave velocities and first arrival calculations used herein.

This post-impact sequence of events is illustrated in Figure 13 and is predicated on the simple fact that tsunami wave trains travel slower than seismic energy by roughly an order of magnitude. In reality, a number of factors likely complicated this scenario. Debris flows originated from several locales (e.g., the Yucatán Platform, the Florida Platform, and the Texas and Louisiana shelf) at distinct times dependent upon the first arrival of seismic energy, but all within ~10 minutes after impact. Thus, the KPBD throughout the Gulf, and particularly in the distal deep water, may contain inter-bedded muddy debrites of unique origin (e.g., pseudowells in Figure 13B). Furthermore, tsunamis likely traveled as one or more wave trains, each of which could have initiated multiple episodes of turbidity currents. Thus, similar to debris flow deposits, turbidites in the KPBD are likely incoherent and of multiple origins and timings throughout the

Gulf. Interestingly, the only component of the KPBD that is both ubiquitous and genetically selfsame is the iridium-enriched carbonate mudstone "cap", as it deposited by settling of fine-grained sediment and ejecta created or resuspended by the impact.

SALT AND BASEMENT CONTROL ON BOUNDARY DEPOSIT DISTRIBUTION

At the end of the Cretaceous, the Louann salt basin was undeformed relative to the present day [*Hudec et al.*, 2013a]. However, subsequent salt movement in the Cenozoic has left an indelible mark on the structure of the KPBD, complicating signals of depositional controls and structural features. While the amount of sediment mobilized by the impact appears to have been sufficient to blanket the entire deepwater Gulf of Mexico, regional trends in thickness of the KPBD within the Louann salt basin province nevertheless appear to reflect existing structural and source controls on deposition (Figure 7). The southwest-to-northeast trend of thinning of the KPBD in the western salt basin coincides with the speculated limit of oceanic crust of *Hudec et al.* [2013a]; [*Hudec et al.*, 2013l], suggesting regional control by basement and overlying salt structure (Figure 7).

Hudec et al. [2013a] recently document the existence of a 1–4 km-high ramp between thin, highly rifted continental (or "transitional" [e.g., *Buffler and Sawyer*, 1985; *Ibrahim et al.*, 1981]) crust and old oceanic crust in the northern Gulf of Mexico (Figure 14). Throughout the Late (post-Callovian) Jurassic, salt within the basin likely migrated basin-ward as a result of existing structure and sediment-loading on the shelf, welling within the low above thin transitional crust and buttressed by the basement ramp (Hudec *et al.* 2013a). By the start of the Cretaceous, salt may have breached the ramp, continuing its basin-ward allochthonous advance until aggradation of sediments on the salt terminus was sufficient to cease migration at the end of the Cretaceous. Thus, at the time of impact, the paleo–Sigsbee Escarpment (i.e., the seaward

extent of salt) was likely southeast of the limit of oceanic crust and a regional salt high would have been located landward of this point (Figure 14A). Farther landward of this salt buttress, there likely would have been a regional basin (or minibasin province) created by relatively recent and long-lived (roughly 100 Ma) salt evacuation.

The hypothesized Late Cretaceous ancestral salt basin is an analog or end-member to the modern Louann salt basin, in which it is helpful to define provinces by distribution and interaction of allochthonous salt as per *Pilcher et al.* [2011]. We postulate that in the Mesozoic, gravity- and sediment-loading-driven seaward migration created substantial accommodation space adjacent to the shelf, creating a relatively uniform regional salt-evacuation basin. While it is difficult to speculate as to the complexity of landward salt-evacuation basin because postdepositional salt movement has obscured any record thereof, we hypothesize that the basin was relatively uniform (and thus KPBD deposition was relatively isopachous) as a result of the immaturity of the salt province. However, the KPBD in the western Louann salt basin exhibits considerable local change in thickness, suggesting either depositional control by local salt highs within the salt-evacuation basin, postdepositional overprint due to salt movement, or a combination thereof. While it is probable that the salt-evacuation basin had minor local changes in relief that had some control on sediment distribution (Figure 13), it is unlikely that the basin had significant relief that would result in the relatively short-wavelength variability in KPBD thickness.

Aside from regional relief, salt topography within the Louann salt basin at the time of impact likely provided the greatest local bathymetric variation within the deepwater paleo-Gulf. Generally, the regionally isopachous nature of the KPBD within the salt provinces suggests two factors were involved in deposition of sediment redistributed by the impact: (1) salt topography

was relatively minor at the time of the impact and subsequent sediment gravity flows, which permitted the deposit to blanket the seafloor in the deepwater; and (2) that the sediment gravity flows were sufficiently voluminous and energetic to surmount virtually all paleobathymetric highs within the salt province, which likely contained the highest local paleobathymetric relief in the Gulf.

VOLUME OF SEDIMENT MOBILIZED BY THE CHICXULUB IMPACT IN THE GULF OF MEXICO

Denne et al. [2013] recently calculated an estimate of ~5.8×10^4 to 2.59×10^5 km^3 for the volume of global KPBD and ~4.3×10^4 to 1.16×10^5 km^3 for KPBD within the Gulf of Mexico basin. While these calculations are valuable and reasonable estimations of sediment volume deposited by the impact, they are simplistic, as they rely upon a single minimum and maximum average thickness derived from end-member wells for entire regions of the Gulf (e.g., Gulf basin floor, Florida Platform, etc.). The regional seismic mapping performed for this study affords a higher degree of accuracy for volumetric calculations, and results indicate that the volume of the KPBD in the northern Gulf of Mexico alone was ~1.05×10^5 km^3 (Table 2), roughly equivalent to the upper bound suggested by *Denne et al.* [2013] for the entire Gulf. It is conservative to assume that deposits in the southern Gulf have a similar distribution and volume to those in the northern Gulf, given proximity to the crater; nevertheless, such an assumption yields a total KPBD volume of ~1.98×10^5 km^3 (Table 2), more than twice the most recent estimate [cf., *Denne et al.*, 2013]. Given the proximity of the southern Gulf to the Chicxulub impact basin, it is likely that the southern Gulf had considerably more sediment derived from the impact basin proper, and thus it is reasonable to speculate that average KPBD thickness in the southern Gulf is greater than that in the northern Gulf. As such, total KPBD volume in the Gulf

is likely in excess of our estimate. Regardless, the KPBD represents the single most voluminous event deposit known.

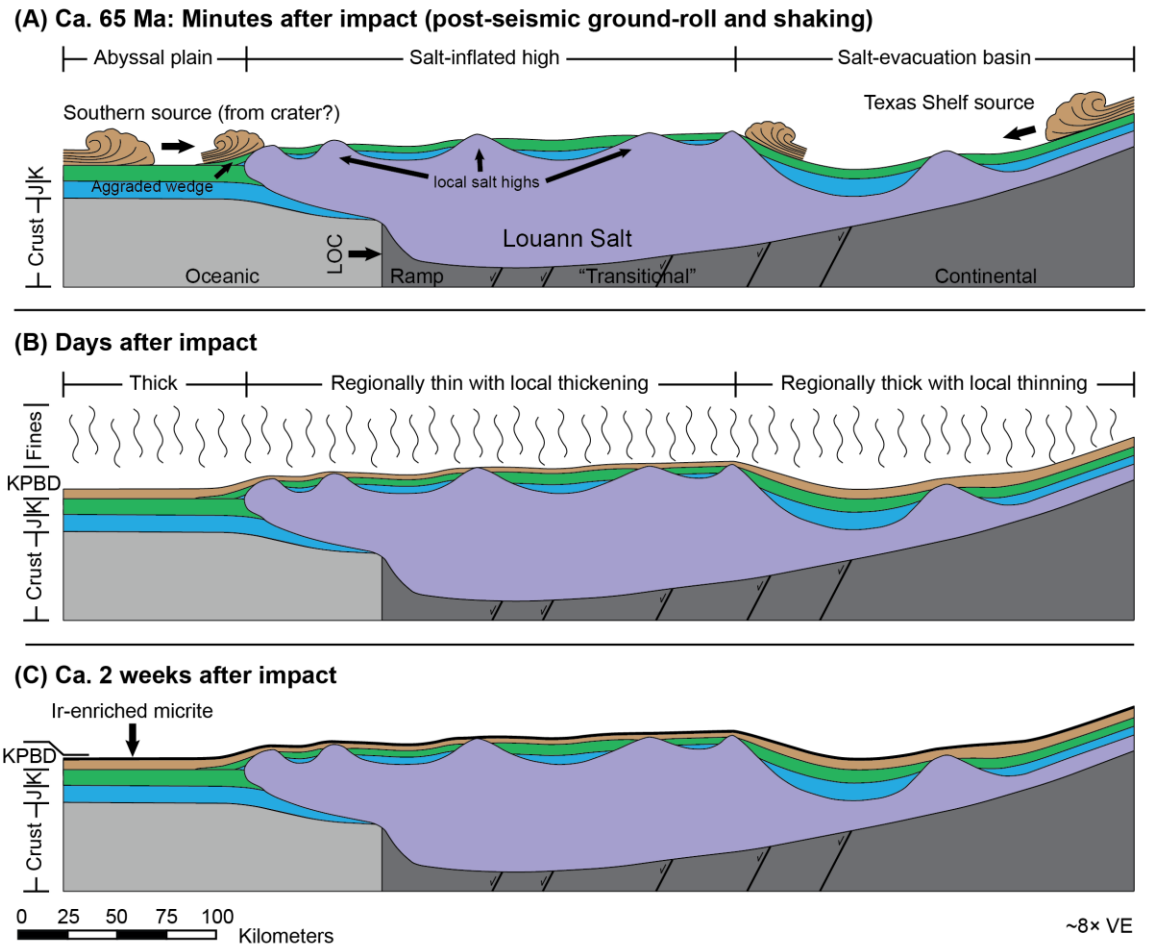

Figure 14: Schematic model for postimpact deposition in the deepwater Louann salt basin province. By the time of the impact at the end of the Cretaceous, gravity- and sediment-loading–driven seaward salt migration has overcome the basement ramp of *Hudec et al.* [2013a]; [*Hudec et al.*, 2013l] and breached the limit of oceanic crust (LOC), resulting in an outer (seaward) salt-inflation high and an inner (landward) salt-evacuation low within the salt basin. **(A)** After seismic and tsunamic energy input by the impact mobilizes sediment throughout shallow waters of the Gulf, the KPBD blankets the deepwater Gulf but is restricted within the salt basin in the region of the salt-inflation high, resulting in a regional trend of thinning in the distal salt basin (Figure 7). **(B)** After wave energy in the Gulf has dissipated, only the finest-grained fraction of remobilized carbonate sediment and iridium-enriched eject remains in the water column, which slowly deposits on the seafloor by suspension settling. **(C)** After all impact-related sedimentation has ceased, the resultant deposit preserves the original control of regional salt distribution on deposition, and normal sedimentation slowly reinstates as the ecosystem recovers. Model for salt migration and Late Cretaceous distribution modified from [*Hudec et al.*, 2013a].

Chapter 5: Summary and conclusions

Regional mapping of the KPBD in the Gulf of Mexico basin with seismic and borehole data reveals that the deposit is virtually ubiquitous in the Gulf of Mexico. Furthermore, core data and seismic correlation strongly support a genetic link to the Chicxulub impact, suggesting that the impact initiated catastrophic Gulf-wide processes that blanketed the entire basin. In particular, we present evidence of several characteristics of impact-generated depositional processes and the implications thereof:

1) Sediment in the KPBD did not originate exclusively from the Chicxulub impact basin, but rather derived from shallow-water areas throughout the Gulf, as a result of seismic and wave energy that was input into the Gulf by the impact. In particular, the Texas and Louisiana shelf and DeSoto Canyon appear to have been major sources for sediment to the KPBD. As such, the KPBD as a whole is not an impactite, *sensu stricto*, but rather an impact-related clastic deposit.
2) Sediment gravity flow was the primary mechanism for sediment transport in the Gulf as a result of seismic and tsunamic energy generated by the impact. Specifically, on the basis of KPBD sedimentology in the southeastern Gulf, muddy debris flows are speculated to be the first and dominant mechanism for sediment transport, with turbidity currents being a secondary mechanism in terms of timing and volume. Furthermore, muddy debris flows are interpreted to have been primarily seismogenic and to have been initiated within minutes of the impact. Likewise, turbidity currents are interpreted to be primarily megatsunamigenic and to have been initiated within ~1–2 hours of the impact. In platform- and shelf-marginal areas throughout the Gulf, local collapse due to seismic ground-roll and shaking resulted in slumps and slides that accompanied the debris flows.

Finally, sediment deposited by settling of suspended carbonate fines and iridium-enriched ejecta blanketed the Gulf, likely within 2 weeks of the impact.

3) Salt distribution and geometry in the ancestral Louann salt basin played a significant role in controlling sediment deposition both regionally and locally. In particular, basement control on salt migration possibly resulted in a regional landward "salt-evacuation basin" and seaward "salt-inflated high" that resulted in a thick KPBD in the interior Louann salt basin and a thin KPBD proximal to the Sigsbee Escarpment. Furthermore, smaller-scale (1–3 km-wavelength) rugosity of the para-autochthonous salt sheet possibly produced local variation of KPBD thickness throughout the Louann salt basin.
4) Mapping of KPBD thickness with seismic and borehole data throughout the northern Gulf of Mexico indicates that deposit volume in the northern Gulf is ~1.05×10^5 km^3, suggesting that total KPBD volume in the entire Gulf is greater than ~1.98×10^5 km^3.

GEOMECHANICS OF RESERVOIR-SCALE SAND INJECTITES, PANOCHE HILLS, CALIFORNIA

Chapter 6: Introduction

The Panoche Giant Injection Complex (PGIC) is exposed on the western margin of the San Joaquin Valley in central California and is the largest known exposure of reservoir-scale sand injectites in the world [*Vétel and Cartwright*, 2010] (Figure 15). The PGIC is a complete injectite system (i.e., with connected source, injected, and extruded sands) with remobilized sand spanning ~600 m of true stratigraphic thickness (TST) over ~25 km of lateral stratigraphic distance (Figures 15–16 and Table 2).

Previous publications provide a descriptive framework for injectite geometry at the PGIC. *Anderson and Pack* [1915] originally identified injectites as being characteristic of the Late Cretaceous (now recognized as Maastrichtian and Danian) foraminiferal and diatomaceous shales of the uppermost Chico Group, which they termed the Moreno Formation for its namesake and type locale, Moreno Gulch [*McGuire*, 1988]. Early studies focused on resolving the stratigraphy and depositional history of the Moreno Formation and bounding strata in the area [e.g., *Durham*, 1943; *Martin*, 1964; *McGuire*, 1988; *Natland*, 1957; *Payne*, 1951; 1962; *Stock*, 1939; *Zimmerman*, 1944]. *Jenkins* [1930] made an early attempt to address injection geomechanics in the PGIC.

Smyers and Peterson [1971] made the first effort to exhaustively characterize injectites and explain the geomechanical behavior of the PGIC. Since then, many efforts have been made to further characterize and interpret PGIC geomechanics [e.g., *Friedmann et al.*, 2002; *Minisini and Schwartz*, 2007; *Schwartz et al.*, 2003; *A Scott et al.*, 2013; *Vétel and Cartwright*, 2010; *Vigorito*, 2007; *Vigorito and Hurst*, 2010; *Vigorito et al.*, 2008; *Weberling*, 2002]. These studies

have generally taken a regional approach, synthesizing hundreds to thousands of observations and measurements over the entire PGIC.

In contrast, this study relies on detailed observation and measurement in two excellent locales in order to interpret injectite geomechanics. Moreno Gulch and Marca Canyon in the northern Panoche Hills contain stratigraphically complete exposures of the PGIC (Figures 15–16). These exposures allow us to identify trends in injectite style and orientation and therefrom infer geomechanical controls. Moreno Gulch and Marca Canyon were first reported by *Anderson and Pack* [1915] and *Payne* [1951], respectively, though no work to date has focused exclusively on injectites in these locales. We utilize outcrop observations and measurements to construct a detailed two-dimensional stratigraphic model of the PGIC at Moreno Gulch and Marca Canyon. We use this stratigraphic model to infer the plaeostress state of the PGIC. We characterize individual and cumulative aperture behavior and employ three conventional hydraulic fracture models (GdK, PKN, and penny models) to model this behavior. Finally, we invoke the results of this model to suggest that injectites in the PGIC were emplaced as radially propagating fractures.

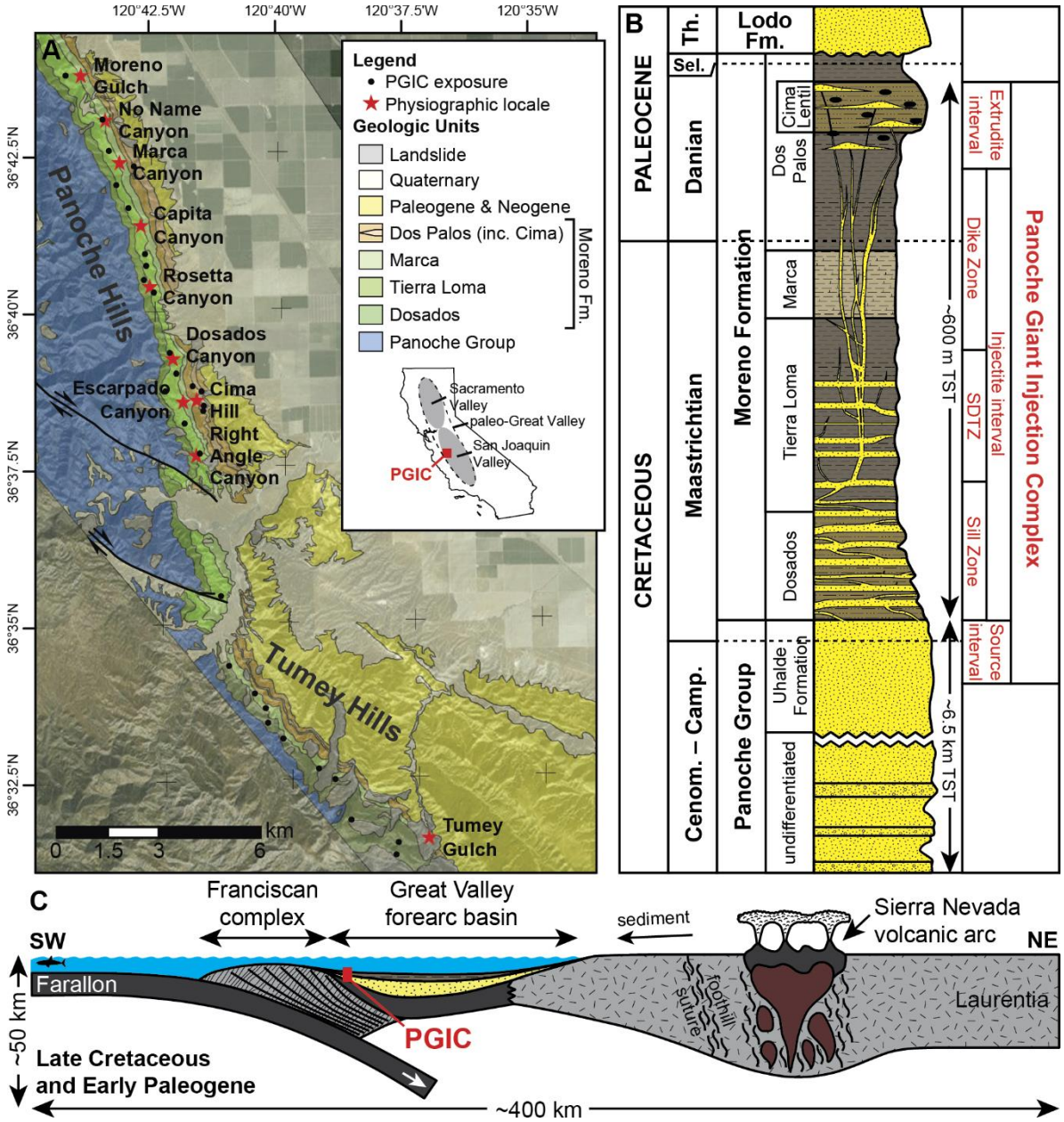

Figure 15: (A) Location map of the PGIC in the Panoche and Tumey Hills of central California. All results in this publication are from Moreno Gulch and Marca Canyon, two of the northernmost locales of the PGIC. (B) Stratigraphy of the mud-prone Moreno Formation overlying the sand-prone Uhalde Formation, as well as a generalized schematic of PGIC architecture. (C) Schematic tectonic model of the PGIC on the western margin of the Great Valley forearc basin in the Late Creteaceous and Early Paleocene. (B) is modified from *McGuire* [1988] and (C) is modified from *Ingersoll* [1979].

Figure 16

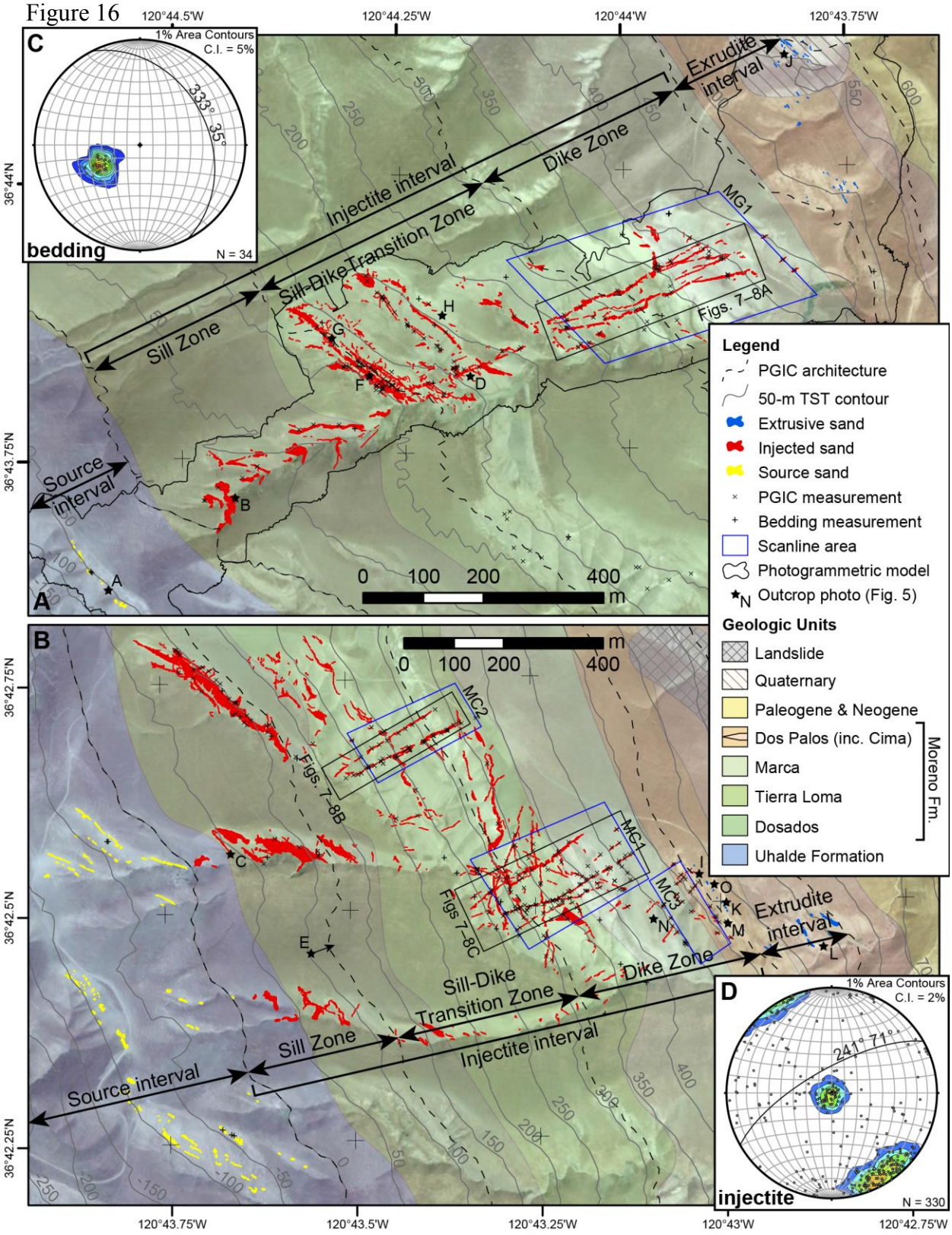
120°44.5'W
120°44.25'W
120°44'W
120°43.75'W
36°44'N
36°43.75'N
36°42.75'N
36°42.5'N
36°42.25'N
120°43.75'W
120°43.5'W
120°43.25'W
120°43'W
120°42.75'W
C
1% Area Contours
C.I. = 5%
333°, 35°
bedding
N = 34
Injectite interval
Dike Zone
Sill-Dike Transition Zone
Sill Zone
Source interval
Extrudite interval
MG1
Figs. 7–8A
A
B
C
D
E
F
G
H
I
J
0 100 200 400 m
MC2
Figs. 7–8B
MC1
Figs 7–8C
MC3
K
L
M
N
O
Sill-Dike Transition Zone
D
1% Area Contours
C.I. = 2%
241°, 71°
injectite
N = 330
Legend
PGIC architecture
50-m TST contour
Extrusive sand
Injected sand
Source sand
PGIC measurement
Bedding measurement
Scanline area
Photogrammetric model
N Outcrop photo (Fig. 5)
Geologic Units
Landslide
Quaternary
Paleogene & Neogene
Dos Palos (inc. Cima)
Marca
Tierra Loma
Dosados
Moreno Fm.
Uhalde Formation

Figure 16: Aerial imagery of (A) Moreno Gulch and (B) Marca Canyon in the northern Panoche Hills illustrating mapped source and remobilized sands of the PGIC, location of measurements and photogrammetric model acquired for this study, and stratigraphy of the Moreno Formation from [*Bartow*, 1996]. Locations of scan line areas are indicated by blue boxes and locations of Figures 7–8 are indicated by black boxes. Stars indicate approximate location of outcrop photographs in Figure 5. (C) Stereographic projection of poles to planes of all 36 bedding measurements collected in Moreno Gulch and Marca Canyon, with average bedding plotted as a great circle. (D) Stereographic projection of poles to planes of paleo-orientation of 327 injectite measurements collected in Moreno Gulch and Marca Canyon, illustrating clustering of sills paleo-oriented horizontally and high-angle dikes with an average paleo-orientation of 241° 71°.

PGIC architecture		Thickness (m)					
		Moreno Gulch			Marca Canyon		
Extrudite interval		80			90		
Injectite interval	dike zone	210	490	570	210	520	610
	SDTZ	190			190		
	sill zone	130			160		
Source interval		400			400		

Table 2: Stratigraphic thickness of the Panoche Giant Injection Complex.

Chapter 7: Geologic background

Tectonic and depositional setting

The PGIC and its host Moreno Formation are exposed in a narrow belt along the eastern limit of the Panoche Hills at the western margin of the modern San Joaquin Valley (Figure 15). There, marine sediments of Middle Cretaceous to Paleogene age comprise an easterly dipping monocline that plunges beneath Neogene and Quaternary valley-fill of the ancestral Great Valley forearc basin. The Great Valley was a long-lived forearc basin formed by subduction of the Farallon plate. Throughout the Late Jurassic and Cretaceous, this basin sustained sedimentation predominately from the easterly Sierra Nevadan magmatic-plutonic complex that is recorded by the Great Valley Sequence (Figure 15C) [*DeGraaff-Surpless et al.*, 2002; *W Dickinson and Seely*, 1979; *W R Dickinson*, 1976; *Graham*, 1987; *Ingersoll*, 1979; 1983]. During this time, sediments from the east slowly infilled the deep-marine basin as the westerly Farallon accretionary complex was a seaward paleobathymetric barrier (Figure 15C) [*W Dickinson and Seely*, 1979; *W R Dickinson*, 1976; *Graham*, 1987].

By the Late Cretaceous, the Great Valley forearc basin was a shallow sea, and by the Early to Middle Maastrichtian, uplift of the Farallon accretionary complex began contributing sediment from the west (Figure 15C) [*McGuire*, 1988; *Mitchell et al.*, 2010]. Westward progradation throughout the Late Cretaceous and Early Paleocene resulted in a transition from cyclic deposition of sand and mud in a basinal setting, recorded by the upper Panoche Group, to steady deposition of organic rich mud in slope and shelfal settings, recorded by the Moreno Formation (Figure 15B) [*McGuire*, 1988; *Payne*, 1962]. By the Selandian, the Great Valley basin had filled to shelfal depths (< ~200 m), and by ~30 Ma, Farallon plate–subduction ceased as the proto–San Andreas transform margin formed [*Atwater*, 1970; *Ingersoll*, 1979].

Stratigraphy of the Panoche Giante Injection Complex

The Moreno Formation conformably overlies the Uhalde Formation of the upper Panoche Group, which consists of sand with interbedded mud [*McGuire*, 1988; *Payne*, 1962]. Sands of the upper Uhalde Formation outcrop on a prominent ridge to the southwest of Moreno Gulch and Marca Canyon (Figure 16). This ridge represents a regional stratigraphic transition from the sand-prone Panoche Group to the mud-prone Moreno Formation, and is reflected topographically as a transition from steep and rugose to subtle and weathered terrain from west to east in the Panoche Hills.

The Moreno Formation consists predominately of red-brown to gray thinly bedded (mm-scale), but occasionally massive, brittle, and extremely friable mudstone. It is ~575 m thick in Moreno Gulch and ~700 m thick in Marca Canyon and is subdivided into 5 members according to minor paleontologic and lithologic changes [*McGuire*, 1988; *Payne*, 1962]: the basal Dosados sand and shale member, the Tierra Loma shale member, the Marca shale member, and the upper Dos Palos shale member and its constituent Cima Lentil sub-member (Table 3 and Figures 15B and 17). The Moreno Formation is unconformably overlain by sands of the late Paleocene and Eocene Lodo Formation [*McGuire*, 1988; *Payne*, 1962]. In Moreno Gulch and Marca Canyon, this unconformity is within the Cima Lentil sub-member, though elsewhere in the Panoche Hills it is reported to be in the upper Dos Palos member (i.e., above the Cima Lentil) [*Anderson and Pack*, 1915; *Bartow*, 1996; *Martin*, 1964; *McGuire*, 1988; *Payne*, 1951; 1962].

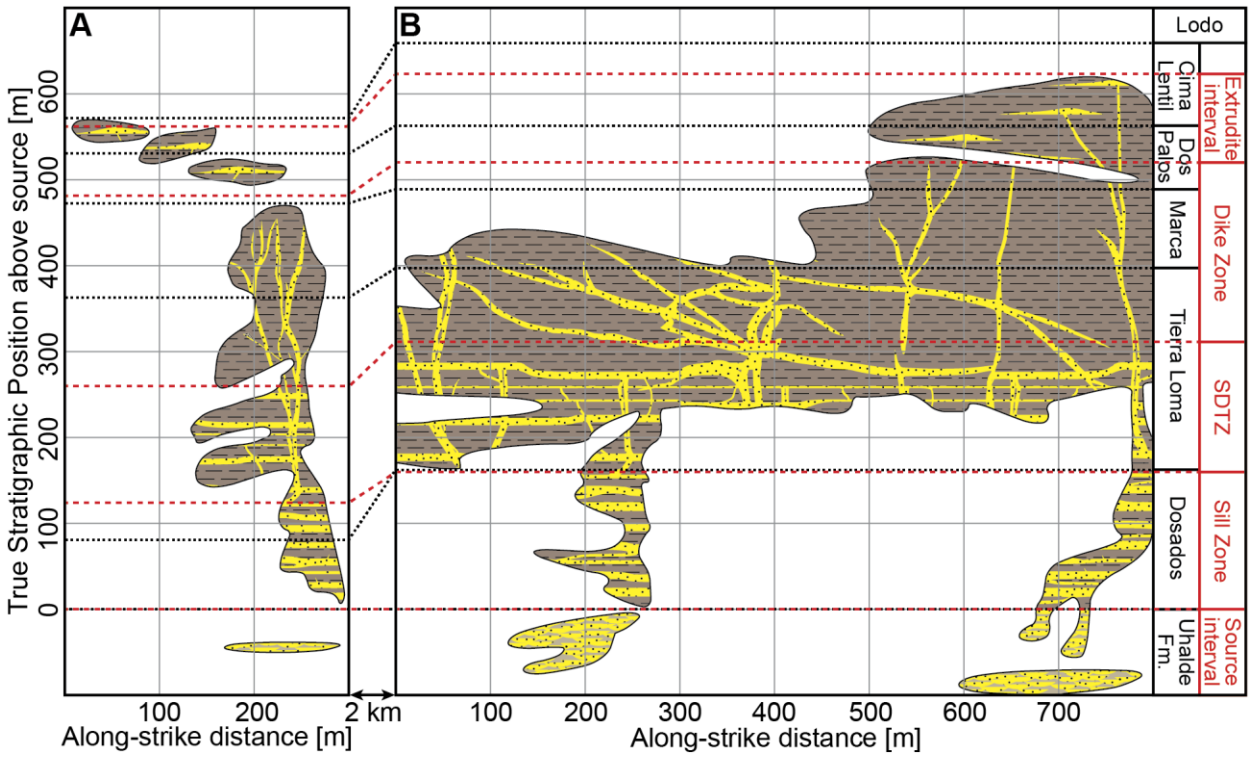

Figure 17: Schematic measured sections of (A) Moreno Gulch and (B) Marca Canyon illustrating architecture of the PGIC and stratigraphy of the Moreno Formation. Both locales expose the complete PGIC from source interval to extrudite interval. Architectural intervals and zones of the PGIC are approximately stratigraphically conformable.

Stratigraphic unit	Thickness (m)		Predominant lithology
	Moreno Gulch	Marca Canyon	
Cima sand lentil	25	125	Extrusive sand and slope-forming mud and sand
Dos Palos shale	75	75	Red-brown mud with extrusive sand
Marca shale	125	125	Red-brown mud with a white-purple hue
Tierra Loma shale	275	225	Red-brown mud
Dosados sand & shale	75	150	Red-brown mud
Uhalde Formation		1,030*	Channel sands
Undiff.		5,690*	Sand and mud

*Thicknesses from [*Payne*, 1962]

Table 3: Stratigraphic thickness of the Moreno Formation and underlying Panoche Group.

Chapter 8: Materials and methods

Field measurement

We measured the orientation (i.e., strike and dip) of 120 injectites and the aperture (i.e., thickness normal to the plane of orientation) of 117 injectites at Moreno Gulch (Figure 16A–B and Table 4). We measured the orientation of 210 injectites and the aperture of 230 injectites in Marca Canyon (Table 4). We measured bedding orientation at 15 locations in Moreno Gulch and 19 locations in Marca Canyon (Figure 16 and Table 4). All measurements and observations were georeferenced with a handheld GPS unit (1–5 m accuracy). At both locales, we made systematic measurements along "scan lines" at successive stratigraphic levels in order to resolve stratigraphic changes in injectite orientation and aperture (Figure 16A–B). Scan lines are oriented roughly along-strike (145–150° bearing) [cf., *Vétel and Cartwright*, 2010]. We acquired a large, sparse scanline grid (0.082 km^2, 8 lines) at Moreno Gulch and three small, dense grids at Marca Canyon (~0.023–0.054 km^2, 5–10 lines each; Figure 16A–B and Table 5). We report orientations as azimuthal strike and dip according to the right-hand rule (e.g., bedding is oriented 333° 35°). We tabulate all measurement results in Table A6 of Appendix 3.

Stereonet3D was used to stereographically project bedding and injectite orientation data [*Allmendinger et al.*, 2012; *Cardozo and Allmendinger*, 2013]. Average (i.e., mean vector) bedding orientation was determined by the method of *Fisher* [1953] using Stereonet3D. Contouring of orientation data was also performed with Stereonet3D. In order to estimate paleo-orientation of injectites, all data were rectified to bedding-horizontal by rotating 35° counterclockwise around an axis trending 333° and plunging 0° (i.e., the average bedding plane; Figure 16C).

In order to plot paleo-orientation and aperture data by True Stratigraphic Position (TSP), we converted data from Cartesian coordinates (i.e., UTM coordinates with elevation values) into TSP with basic trigonometric transforms. This methodology is detailed in Appendix 3.

Unmanned aerial vehicle photogrammetry

We acquired photogrammetric data of Moreno Gulch with a DJI Phantom 2 UAV unit gimbal-mounted with a GoPro Hero3. We used Agisoft PhotoScan Pro to process photogrammetric data and export processed models to Applied Imagery Quick Terrain Modeler and ArcGIS Desktop for laboratory mapping. Acquisition and processing methodology is detailed in Appendix 4.

Grain size analysis

We collected 10 samples of depositional and remobilized sand for quantitative grain size analysis. Samples were disaggregated by water dissolution and sonication and analyzed using a Malvern Mastersizer 3000 laser diffraction particle size analyzer.

Laboratory mapping

We mapped the PGIC on aerial imagery in Moreno Gulch and Marca Canyon to evaluate locale- and regional-scale architecture (Figure 16). Parent, injected, and extruded sands and accessory elements (e.g., mudstone mounds and carbonate concretions) were mapped by coupling field observations and measurements with aerial imagery. The photogrammetric data acquired for this study were used for mapping in Moreno Gulch (5–10-cm resolution), whereas Spot Image imagery via Google Earth Pro was used in Marca Canyon (~2.5-m resolution).

Locale	Bedding orientation	Injectite orientation	Injectite aperture	Scan lines
Moreno Gulch	15	120	117	4
Marca Canyon	19	210	230	20
Total	34	330	347	24

Table 4: Number of orientation and aperture measurements and scan lines.

Locale	Name	Line spacing (m)	Lines/grid	Area (km^2)
Moreno Gulch	MG1	80	5	0.082
	MC1	30	10	0.054
Marca Canyon	MC2	30	9	0.027
	MC3	30	5	0.023

Table 5: Scan line grid geometries and logistics

Chapter 9: Results

Stratigraphy of the Panoche Giant Injection Complex

Contacts between most members of the Moreno Formation are impossible to ascertain in the field as a result of the lithologic homogeneity of the formation. Two exceptions are the Marca member, which is distinct in outcrop and aerial imagery for its purple-white hue, and the Dos Palos member and Cima Lentil submember, which are distinct for sands therein (Figure 16). The majority of thinning of the Moreno Formation from Marca Canyon to Moreno Gulch is in the Cima Lentil sub-member (~100 m; Figure 17 and Table 3). This change in thickness is likely at least in part due to the overlying erosional unconformity at the base of the Lodo Formation (Figures 16B and 17), though thinning also occurs in the Tierra Loma (~50 m) and Dosados members (~75 m; Table 3). Other members of the Moreno Formation are isopachous across the two locales (Table 3).

Bedding measurements of the Moreno Formation are difficult to acquire due to the friability of mudstones, except in the upper Dosados and lower Tierra Loma, where bedding is more fissile and planar. Consequently, bedding measurements are concentrated in this interval. The average orientation of the 36 bedding measurements is 333° 35°, with a standard deviation of 9° strike and 7° dip. (Figure 16C). Bedding orientation is remarkably homoclinal throughout the PGIC in Moreno Gulch and Marca Canyon and does not exhibit any significant change with stratigraphy or locale.

Architecture of the Panoche Giant Injection Complex

The PGIC is a complete injectite system composed of three intervals: a source sand interval, an injected sand (i.e., injectite) interval, and an extruded sand (i.e., extrudite) interval. In Moreno Gulch and Marca Canyon, the entire PGIC (including the source interval) is less than

~1.1 km thick, whereas the interval of remobilized (i.e., injected and extruded) sand is ~600 m thick (Table 2).

Source interval

The upper Uhalde Formation outcrops on the ridge to the southwest of Moreno Gulch and Marca Canyon (Figure 16) and is the inferred source for the PGIC based upon grain size, composition, and proximity to injectites. This inference has been made by previous authors [e.g., *Friedmann et al.*, 2002; *Jenkins*, 1930; *Payne*, 1951; *Smyers and Peterson*, 1971; *Vigorito*, 2007] but is corroborated here by quantitative grain size analysis of samples from the middle and upper Uhalde Formation and from remobilized sands (Figure 18). Sandstone of the upper Uhalde Formation consists of carbonate-cemented, gray-brown to tan sands. Sands are well sorted, unimodal, and upper-fine to lower-medium–grained (Figure 18 and Table A6). Grain size decreases to very fine ~400 m below the top of the Uhalde Formation (in the middle Uhalde Formation according to thicknesses reported by [*Payne*, 1962]), indicating that the source sand interval is limited to the upper Uhalde Formation and is less than ~400 m thick (Figure 18).

Most outcrops of the upper Uhalde Formation in Moreno Gulch and Marca Canyon contain one or more of three distinct lithofacies: an upward-fining basal unit, a planar-laminated middle unit, and an upper wavy- to ripple-laminated unit with climbing ripples, convolute laminae, and flame structures (Figure 19). Individual units are decimeters thick and together comprise a partial Bouma turbidite sequence (i.e., T_a–T_c). Individual Bouma sequences are stacked throughout the upper Uhalde Formation, with contacts that often exhibit soft-sediment deformation (Figure 19). On an outcrop scale, stacked sequences frequently have cuneiform bases and are typically 2–4 m thick.

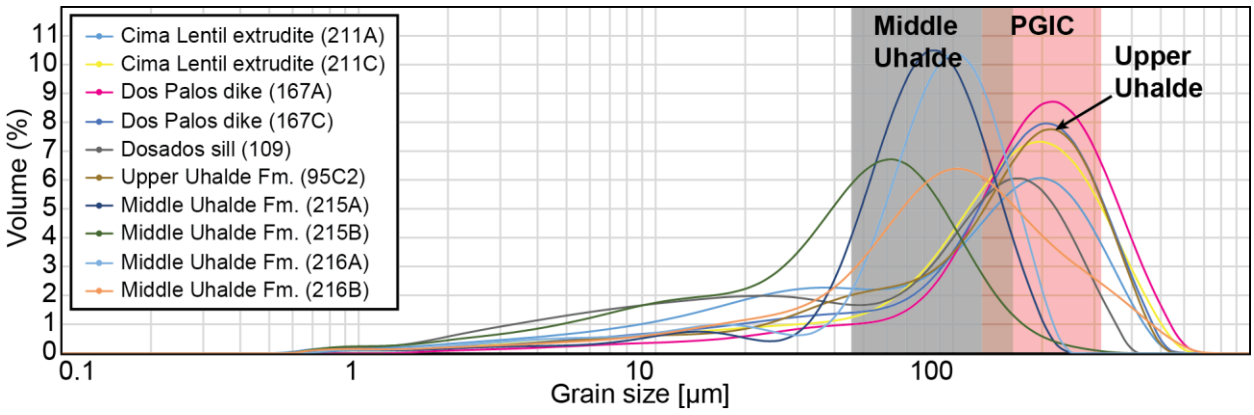

Figure 18: Quantitative grain size of 10 samples of remobilized and depositional sands in Moreno Gulch Marca Canyon. Grain size of the upper Uhalde Formation is very similar to that of remobilized sand from the PGIC, while that of the middle Uhalde Formation is not, indicating that the source sand interval is limited to the upper Uhalde Formation. Samples from the middle Uhalde Formation were obtained in the large canyon west of Marca Canyon.

Injectite interval

Injectites are abundant throughout the Moreno Formation and intrude mudstones at virtually all angles and a wide range of apertures (mm- to dm-scale). The injectite interval is ~490 m thick in Moreno Gulch and ~520 m thick in Marca Canyon (Table 1 and Figure 17). Rarely, mudstone rip-up clasts (~1–30 cm in the largest dimension) are entrained in injected sand (Figure 19B). Sands are poorly carbonate-cemented, well sorted, and range in color from brown to orange to yellow to gray, but are typically light gray and/or orange. Grain size is fine and unimodal, though most sands contain a substantial amount of medium to coarse silt (Figure 18). Injectites are typically massive, but very rarely exhibit planar laminations that are always subparallel to contacts and typically reside on the periphery of injectites and border a massive central core (Figure 19C).

We define three populations of injectites based on the dip of their paleo-orientation (i.e., paleodip): sills (< 15° paleodip), low-angle dikes (15–65° paleodip), and high-angle dikes (< 65° paleodip; Table 5). We encountered 55 sills, 61 low angle dikes, and 211 high angle dikes in

Moreno Gulch and Marca Canyon (Table 6). The population size of high-angle dikes in Moreno Gulch and Marca Canyon is possibly biased by the higher probability of encountering a high-angle feature than a low-angle feature when moving roughly along-strike in the field, as well as the degradation in outcrop quality in the lower Moreno Formation, where sills are most common.

The majority of injectites are approximately planar but occasionally vary significantly in orientation (i.e., strike and dip) and aperture in outcrop. Dikes, particularly the low-angle variety, are the most irregular and often kink, curve, and step, particularly when adjacent to another dike or injection (Figure 19D). Low-angle dikes are also the least continuous where traceable. Many dikes locally interact by noticeably changing orientation or trajectory in close proximity to other injectites, and often crosscut each other (Figure 19D–E).

Injectite styles cluster and exhibit paleo-orientation preferences (Figure 16D). Average paleo-orientation of all sills is horizontal (306° 2°) and average paleo-orientation of all high-angle dikes is 241° 71° (Table 6 and Figure 16D). The low-angle dike population exhibits no paleo-orientation preference (Table 6 and Figure 16D). The high-angle dike orientation preference has been reported previously [e.g., *Friedmann et al.*, 2002; *Smyers and Peterson*, 1971; *Weberling*, 2002].

The injectite interval is composed of a basal sill zone, an intermediate sill-dike transition zone (SDTZ), and an upper dike zone (Figures 17 and 20). Contacts between these zones are gradational and record the upward transition from sills to high-angle dikes. The ~241° 71° paleo-orientation preference of high-angle dikes is consistent across the dike zone and SDTZ (Figure 20B–C and Table 6). High-angle dikes are virtually absent in the sill zone.

The injectite interval is 30 m thinner at Moreno Gulch than at Marca Canyon as a result of thinning of the sill zone (Table 2 and Figure 17). The SDTZ and the dike zone exhibit only

minor changes in thickness (< ~5 m) between the two locales (Table 2 and Figure 17). Architectural zones are roughly stratigraphically conformable, despite relatively minor changes in thickness between locales: the sill zone resides within the Dosados and lower Tierra Loma members (only the former in the case of Marca Canyon); the SDTZ resides within the lower to middle Tierra Loma; and the dike zone resides within the upper Tierra Loma, Marca, and lower Dos Palos members (Figure 17).

Previous authors have proposed various architectures for the injectite interval of the PGIC [e.g., *Friedmann et al.*, 2002; *Smyers and Peterson*, 1971; *Vétel and Cartwright*, 2010; *Vigorito and Hurst*, 2010; *Vigorito et al.*, 2008]. Most identify a lower sill-prone zone and an upper dike-prone zone, though none distinguish a SDTZ between the two. [*Vigorito et al.*, 2008] propose a tripartite architecture based on net-to-gross sand content rather than injectite style.

Sill zone

The sill zone is an ~130–160-m thick zone where thick (~2–10 m) sills predominate (Figures 3 and 6 and Table 2). Sills are the most abundant style of injection in this zone (N = 33), though low-angle dikes are also common (N = 15; Table 6). High-angle dikes are virtually absent (N = 2; Table 6). In the sill zone, the primary means of stratigraphic transgression by injectites is stratigraphic stepping of sills, where part or all of a sill bends upward to connect with an overlying sill (Figure 19F). Thick (~2–10 m) sills often commingle in this fashion, resulting in decimeter-thick networks of interconnected sills (Figure 19F). This phenomenon has been described by several authors [*Hurst et al.*, 2011; *A Scott et al.*, 2013; *Vigorito et al.*, 2008]. Occasionally very thin (mm- to cm-thick) sills accompany thick sills (~3–10 m), and often are concentrated in areas where larger sills step up-section (Figure 19G). Injection of these features is evidenced by irregular, thicknesses and stratigraphic discordance (Figure 19G). Millimeter- to

cm-thick sills are not exclusively associated with thick sills in the sill zone, and are focused in at least one horizon in the SDTZ (middle Tierra Loma) in Marca Canyon. Sills are concentrated in the upper ~50 m of the sill zone, though this may be due to the scarcity and quality of exposures in the lower sill zone in both Moreno Gulch and Marca Canyon (Figures 16 and 20).

Sill-dike transition zone

The SDTZ is a 190-m thick zone where sills, low-angle dikes, and high-angle dikes commingle (Figures 17 and 20 and Table 2). High-angle dikes are most common in this zone (N = 90), and low-angle dikes are slightly more numerous than sills (N = 29 and 22, respectively; Table 6). Many high-angle dikes extend over decimeters to hectometers and ascend into part or all of the dike zone (Figures 21–22). These stratigraphically extensive high-angle dikes often cluster, with two to three dikes originating from a single nexus in the SDTZ and extending upward into the overlying dike zone (Figures 21–22). Low- and high-angle dikes often intersect and connect sills in the SDTZ (Figure19D). Occasionally, very thin (< 1 mm) sill and dike features exist that exhibit no macroscopic aperture, but rather are light-colored streaks in mudstone with high silt to very fine sand content (Figure 19H). In the upper SDTZ and lower dike zone, low-angle injectites often appear to be sills in outcrop but upon measurement are revealed to be low-angle dikes (Figures 16B and 21C). The relative abundance of sills, low-angle dikes, and high-angle dikes is roughly constant throughout the SDTZ (Figure 20A).

Dike zone

The dike zone is approximately 210 m thick (Figures 17 and 20 and Table 2). High-angle dikes predominate this zone (N = 119; Table 6). Low-angle dikes are scarce in the dike zone (N = 17) but are concentrated in the lower half (Table 6). Sills are entirely absent (Figures 20 and Table 6). Stratigraphically extensive dikes in this zone typically cluster and originate the middle

or upper SDTZ (Figures 16 and 21). The dike zone of the Moreno Gulch exposure exhibits one such cluster, while the dike zone of the Marca Canyon exposure exhibits at least two (Figures 16–17, and 21).

In Marca Canyon, thin (< 10 cm) high-angle dikes are present within ~1 m of the lowest extrudite horizon in the Dos Palos member (Figure 16 and 19I). In Moreno Gulch, the last observed dike is ~50 m beneath the extrudite horizon. However, the apparent absence of injectites in this interval at Moreno Gulch may be due to the very poor exposures there (Figure 16).

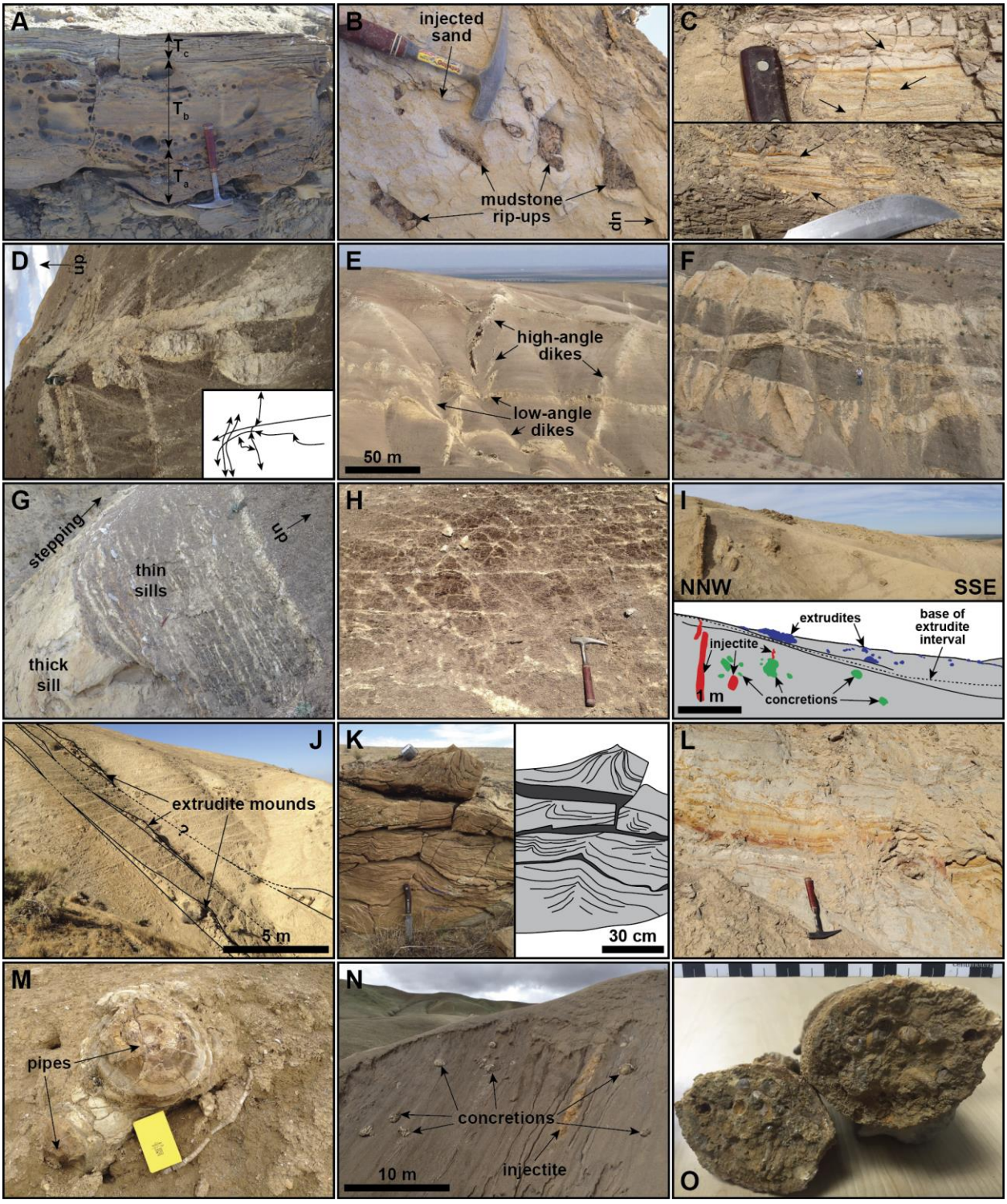
A
T_c
T_b
T_a
B
injected sand
mudstone rip-ups
up
C
D
up
E
high-angle dikes
low-angle dikes
50 m
F
G
stepping
up
thin sills
thick sill
H
I
NNW
SSE
extrudites
base of extrudite interval
injectite
1 m
concretions
J
extrudite mounds
?
5 m
K
30 cm
L
M
pipes
N
concretions
injectite
10 m
O

Figure 19

Figure 19: Field photographs of (A) source, (B–I) injected, and (J–O) extruded sand in Moreno Gulch and Marca Canyon. (A) Outcrop of the upper Uhalde Formation in Moreno Gulch with stacked turbidite sequences associated sedimentary structures. (B) Mudstone rip-up clasts in a sill in the sill zone of Moreno Gulch. (C) Linear flow structures at the boundaries of a ~15- (top) and ~3-cm (bottom) sill in the sill zone of Marca Canyon. (D) Sill and high-angle dike interaction in the SDTZ of Moreno Gulch. (E) Large-scale crosscutting of low- and high-angle dikes in the dike zone of Marca Canyon. (F) A sill complex in the sill zone of Moreno Gulch illustrating the phenomenon of stratigraphic stepping. (G) Thin (cm-scale) sills adjacent to a large sill at a point of stratigraphic stepping. (H) Micro-sills and -dikes with high silt to very fine sand content and no macroscopic aperture in the SDTZ. (I) Outcrop of the upper Marca and lower Dos Palos member documenting high-angle injectites in close proximity to the lowest extrudite horizon in Marca Canyon. (J) Outcrop of the Cima Lentil submember exposing three to four horizons of mounded extrudites in Moreno Gulch. (K) Soft-sediment deformation indicative of focused upward transport at the core of a mounded extrudite horizon in Marca Canyon. (L) Slope-forming sands of unknown origin in the Cima Lentil submember of Marca Canyon. (M) Pipe-like sand bodies in the Cima Lentil submember of Marca Canyon. (N) Outcrop with several distinctive concretions in the upper Marca member of Marca Canyon. (O) A small concretion with abundant tubeworm fossils from the Dos Palos member of Marca Canyon. Approximate locations of photographs are indicated in Figure 16.

Injectite style	Dip	Architectural zone	Number of measurements	Average paleo-orientation		Standard deviation	
				Strike	Dip	Strike	Dip
Sill	< 15°	all	55	216°	88°	99°	4°
		Dike Zone	0	–	–	–	–
		SDTZ	22	208°	87°	89°	4°
		Sill Zone	33	314°	2°	103°	4°
Low-angle dike	15–65°	All	61	–	–	113°	16°
		Dike Zone	17	–	–	128°	17°
		SDTZ	29	–	–	109°	14°
		Sill Zone	15	–	–	91°	15°
High-angle dike	> 65°	All	211	241°	71°	81°	6°
		Dike Zone	119	240°	71°	83°	6°
		SDTZ	90	242°	72°	79°	6°
		Sill Zone	2	–	–	–	–

Table 6: Injectite paleo-orientation by style and architectural zone.

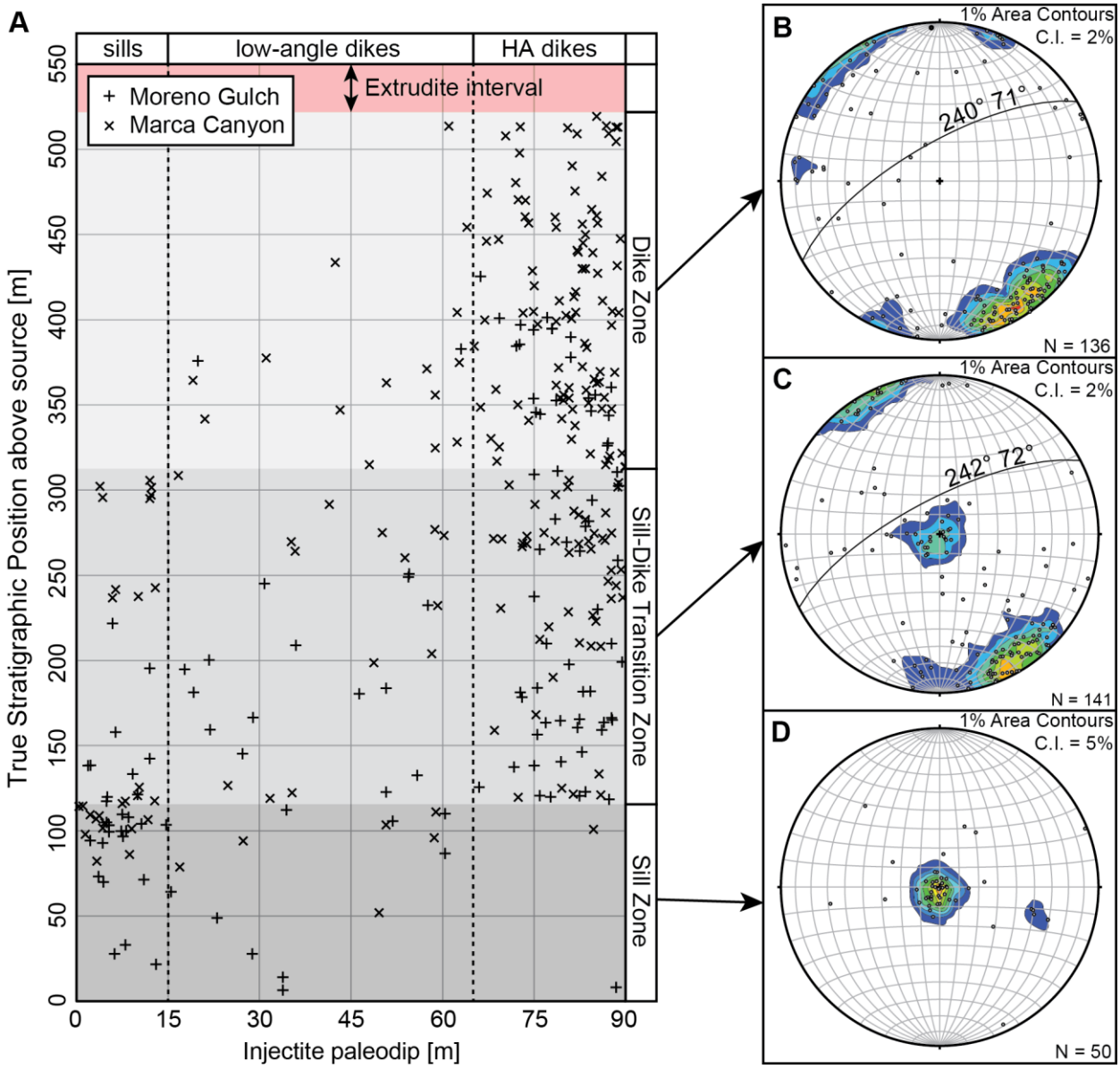

Figure 20: (A) Injectite paleodip versus TSP above PGIC source for all injectites measured in Moreno Gulch and Marca Canyon. Stereographic projections of poles to planes of injectite paleo-orientation in the (B) dike zone, (C) SDTZ, and (D) sill zone.

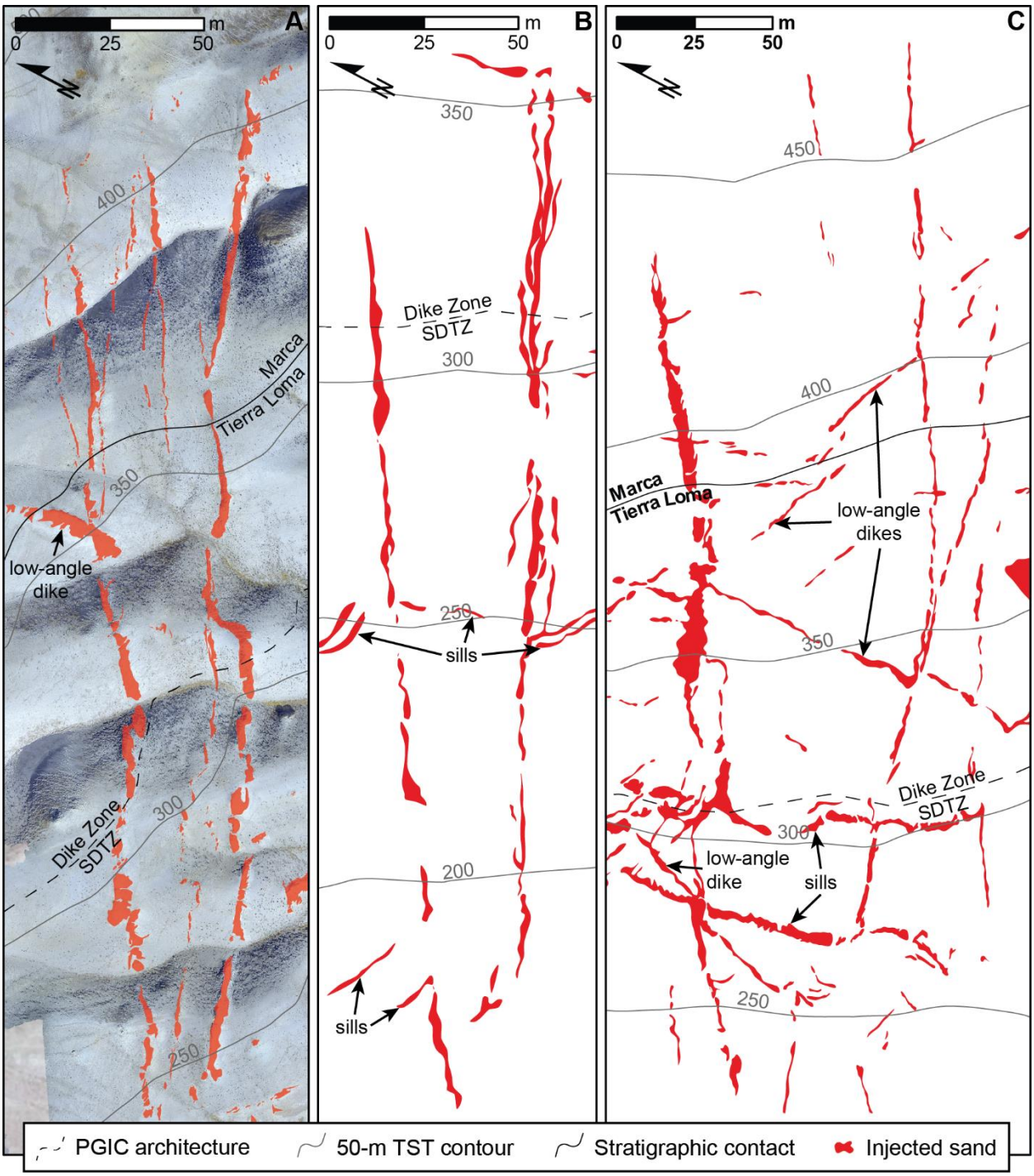

Figure 21: Stratigraphically extensive high-angle dikes and associated sills and low-angle dikes mapped in the middle to upper SDTZ and dike zone in (A) Moreno Gulch and (B–C) Marca Canyon. See Figure 2 for location.

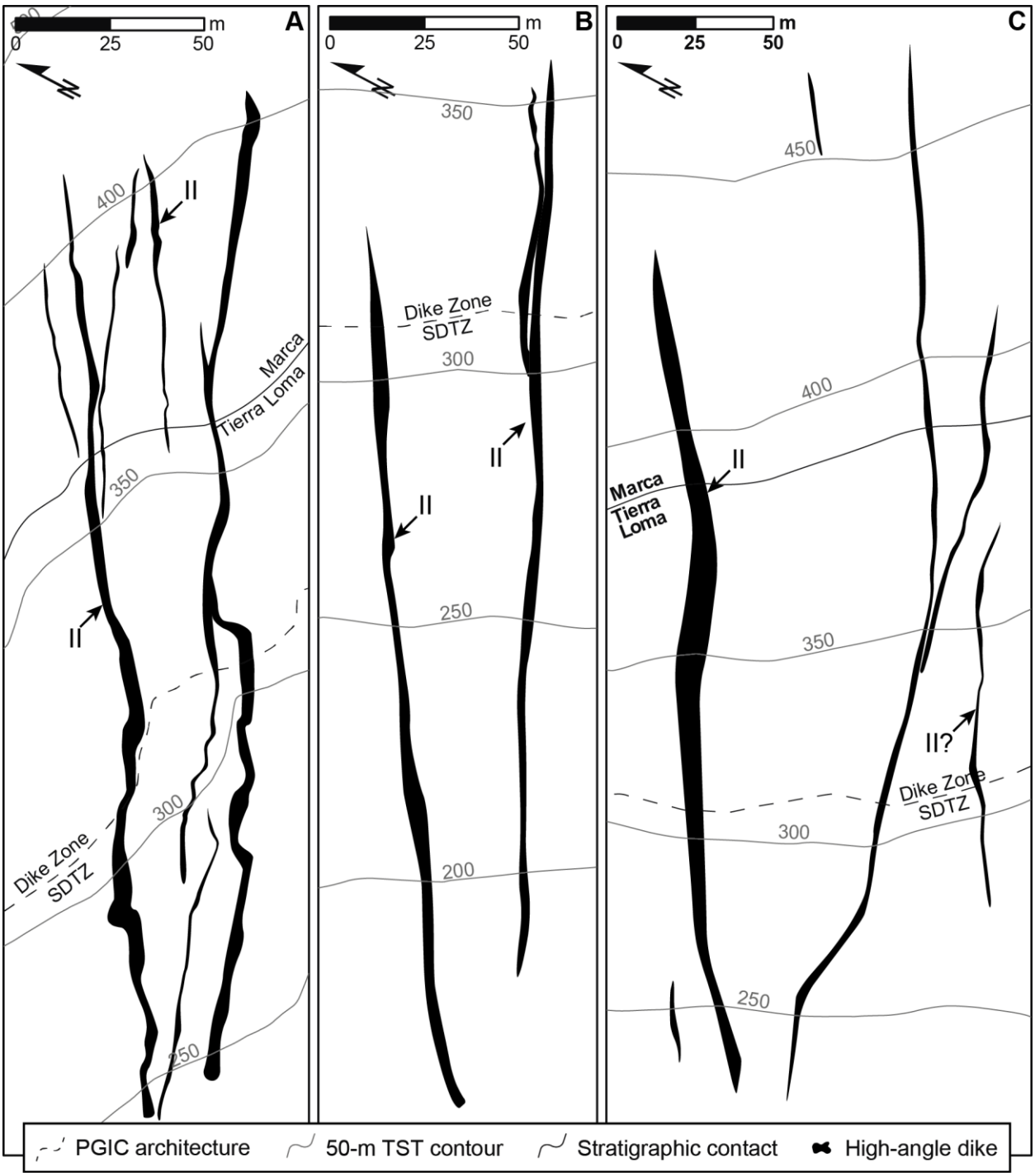

Figure 22: Simplified stratigraphically extensive high-angle dikes in (A) Moreno Gulch and (B–C) Marca Canyon documenting several examples of Type II injectite aperture behavior.

Extrudite interval

Discrete mounded and sheet-like sandstone bodies are common in an interval within the Dos Palos member and Cima Lentil sub-member in both locales. This interval is ~80 m thick in Moreno Gulch and ~90 m thick in Marca Canyon (Figure 16 and Table 2). Sands within these bodies are well sorted, fine-grained, and similar in grain-size distribution to sandstones of the upper Uhalde Formation (Figure 18). Sandstones exhibit massive to planar-, wavy-, ripple-, and cross-laminated fabrics, with contorted laminae and soft-sediment deformation commonly present (Figure 19K). At the thickest point of mounded sandstone horizons, flame structures typically commingle in a stacked fashion (Figure 19K). Small (~2–100-cm diameter) spherical to oblate sandstone bodies with pipe-like morphologies accompany extrudite horizons throughout the Cima Lentil submember (Figure 19M). In cross section, these sandstone bodies often exhibit concentric weathering. These features are particularly common subjacent to the lowest tabular sand horizon in Marca Canyon (at ~650 m TST in Figure 16B). Tan to pale yellow vuggy concretions are common in the upper Marcos and Dos Palos members and Cima Lentil submember (Figure 19N). Concretions occasionally contain common to abundant tubeworm fossils (Figure 19O). These fauna are reported to be vestimentiferan and have been studied in detail by *Schwartz et al.* [2003].

We interpret the mounded and sheet sand bodies of the Dos Palos member and Cima Lentil submember to be extrudites based on the presence of stacked flame structures indicating upward flow, similarity in grain size and composition to subjacent injected sands, and sand volcano–like mound morphologies. Extrudites in Marca Canyon were previously reported by *Vigorito et al.* [2008] and *A Scott et al.* [2013], and are associated with cold-seep carbonates throughout the Panoche Hills reported by *Schwartz et al.* [2003] and *Minisini and Schwartz* [2007]. We interpret that the extrudites extend into the Dos Palos member below the Cima Lentil

submember, in contrast to previous authors who have either mapped or inferred extrudites to be exclusively within the Cima Lentil (Figures 16–17) [e.g., *A Scott et al.*, 2013; *Vigorito et al.*, 2008].

HIGH-ANGLE INJECTITE BEHAVIOR IN THE UPPER INJECTITE INTERVAL

We calculated average and cumulative aperture of high-angle dike measurements and plotted them versus true stratigraphic position to characterize aperture and frequency of high-angle dikes in the upper SDTZ and dike zone (Figure 23). We calculated average aperture from all aperture measurements (347 total; Table 4) in Moreno Gulch and Marca Canyon, whereas we used only scan line aperture measurements (125 total over 24 scan lines) in Moreno Gulch and Marca Canyon to calculate cumulative aperture. Both cumulative and average aperture decrease linearly with proximity to the paleoseafloor (Figure 23).

Average aperture decreases linearly from 2.3 m in the upper SDTZ to 0.25 m at the top of the dike zone (Figure 23A). The linear correlation of average aperture with depth is strong (R^2 = 0.92), though average aperture near to the extrudite zone is approximately constant for ~50 m (475–525 m in Figure 23A). Standard deviation of average aperture also decreases with stratigraphic position, from 2 m at the top of the SDTZ to 0.13 m at the top of the dike zone (bars in Figure 23A). Standard deviation does not behave linearly, but rather steps down from ~1–2 m to less than 1 m within a ~40 m interval in the middle dike zone (350–490 m in Figure 23A).

Normalized cumulative aperture is a direct measure of the minimum horizontal strain due to injection. This ranges from ~5% at the top of the SDTZ to less than 1% at the top of the dike zone (Figure 23B). The linear correlation of normalized cumulative aperture with depth is not as strong as that of average aperture (R^2 = 0.78), though this could be partly due to differences in sample size and calculation methodology (see caption in Figure 23). Normalized cumulative

aperture is also approximately constant in the upper ~50 m of the dike zone, similar to average aperture (475–525 in Figure 23B). Standard deviation of normalized cumulative aperture decreases with depth, from ~0.75–1.25 m at the top of the SDTZ to ~0.12–0.17 m at the top of the dike zone (bars in Figure 23B). Standard deviation does not behave linearly, and some of the largest standard deviations (~2 m) are in the lower to middle dike zone (310–400 m in Figure 23B).

Although average and cumulative aperture decreases upwards, individual dikes do not always follow this bulk behavior (Figure 21). We observed dikes that thin unidirectionally upwards ("Type I") and those that thicken and then thin upwards ("Type II"; Figure 21–22).

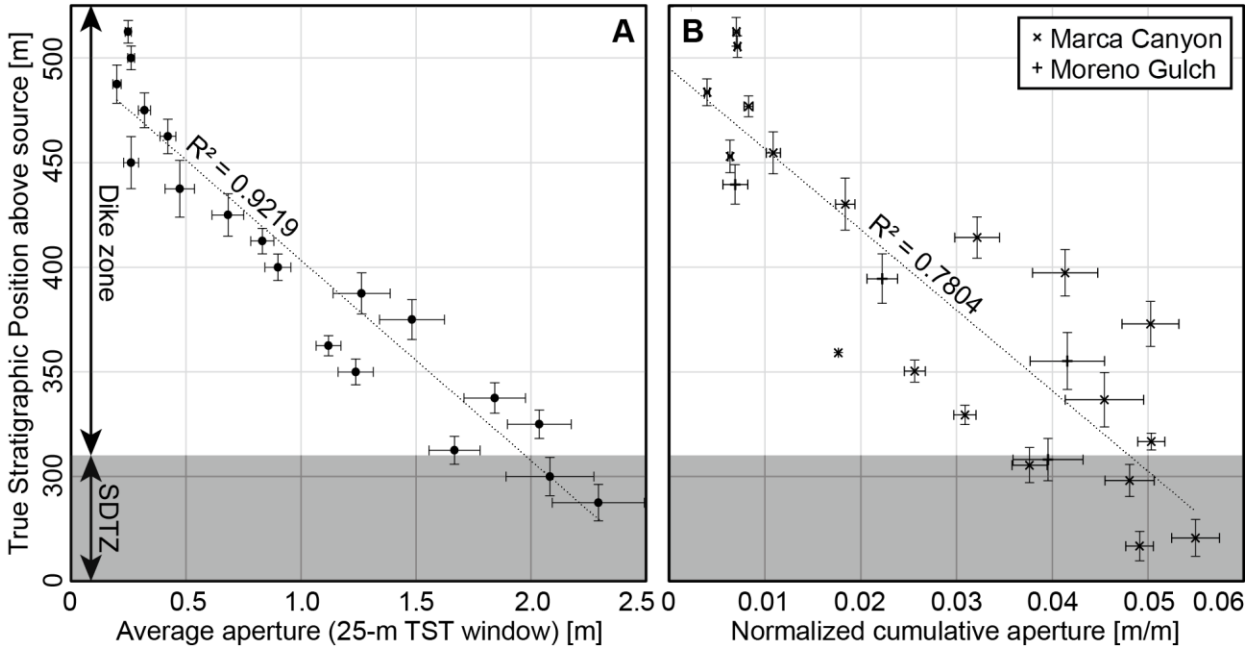

Figure 23: High-angle dike aperture versus stratigraphic position. The "source" is the top of the Uhalde Formation. (A) Average aperture is calculated from all injectite measurements (360 total; Table 2) within a 25-m TST window in 12.5-m intervals. Horizontal bars indicate standard deviation, with the largest being 2.00 m. Vertical bars indicate normalized standard deviation (i.e., coefficient of variation), with the largest being 1.35 (B) Normalized cumulative aperture is calculated from scan lines (Figure 2), with each point representing one scan line. Horizontal bars indicate standard deviation, with the largest being 2.04 m. Vertical bars indicate normalized standard deviation, with the largest being 1.24.

PALEO-ORIENTATION OF EXPOSURES

It is tempting to view an outcrop exposure (e.g., Figures 21–22) as a vertical cross section of injectites. In fact, field exposures are at a low angle relative to paleovertical (Figure 24). The angle of the exposure relative to paleovertical is 53° in Moreno Gulch and 45° in Marca Canyon (Figure 150A). In other words, a field exposure traverses 100–132 m laterally for every 100 m it climbs vertically. Therefore, exposures record any lateral change in injectite behavior that may exist, as well as vertical change. This implies that aperture behavior observed in the field (e.g., Figures 7–9) is a composite of lateral and vertical behavior.

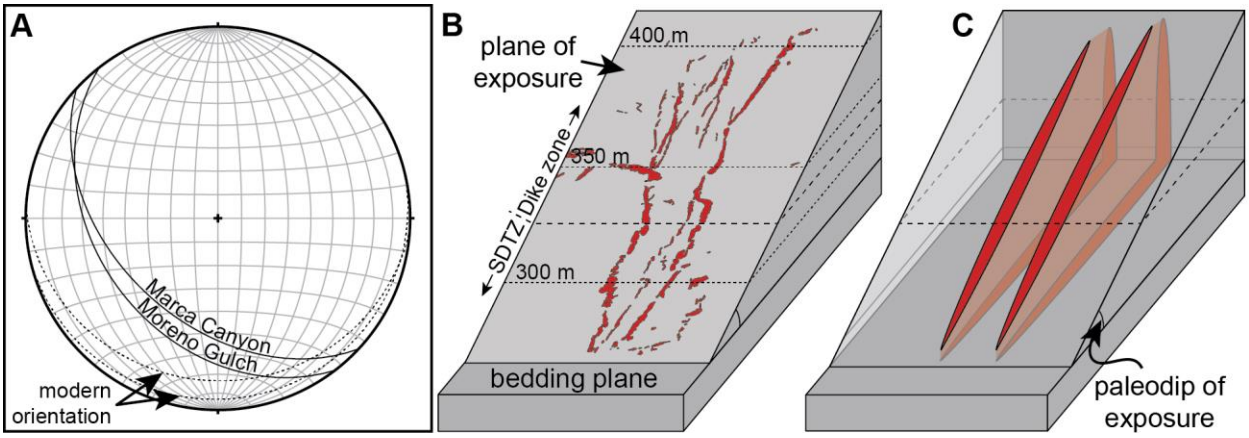

Figure 24: (A) Paleo-orientation (solid) and modern orientation (dashed) of planes representing exposures in Marca Canyon and Moreno Gulch. Paleodip of exposures ranges between 37° and 45°. (B) Schematic of paleo-exposure of stratigraphically extensive high-angle dikes in Moreno Gulch (c.f. Figure 21A) and (C) simplified model of injectites intersected by paleo-exposure.

TWO-DIMENSIONAL INJECTITE MODELS

Conventional two-dimensional hydraulic fracture models rely on propagation of a crack by linear elastic deformation under plane-strain conditions as established by *England and Green* [1963]:

$$W(x) = \frac{2(1-\nu)L\Delta p}{G}\sqrt{1-\left(\frac{x}{L}\right)^2} \qquad (1)$$

Where *W(x)* is the fracture width in the propagation direction, $\Delta p = \sigma - p$ is the pore pressure, *p*, in excess of an external stress, *σ,* L is the extent of the fracture in the propagating direction, and *G* and *v* are the linear elastic rock properties shear modulus and Poisson's ratio, respectively. Models assume that pore pressure distribution in the propagation direction is defined by laminar Newtonian flow through a narrow channel. Width in the propagation direction therefore varies as a function of the pressure drop within that channel.

Two classic two-dimensional hydraulic fracture models are the Perkins-Kern-Nordgren (PKN) and Geertsma–de Klerk (GdK) models (Figure 25) [*J Geertsma and De Klerk*, 1969; *Nordgren*, 1972; *Perkins and Kern*, 1961]. Both models assume that the height, H, of the fracture is fixed and that the fracture propagates linearly (Figure 25A–B). Another model, the "penny" model, is similar to the PKN and GdK models but assumes that the fracture propagates radially (Figure 25C) [*Abe et al.*, 1976; *J Geertsma and De Klerk*, 1969]. The PKN model assumes that the fracture channel is elliptical in cross-section. The shape of the fracture in the propagating direction is therefore:

$$\frac{W(x,y)}{W_{max}} = \left(1 - \frac{y}{H}\right)^{\frac{1}{2}} \left(1 - \frac{x}{L}\right)^{\frac{1}{4}} \tag{2}$$

In contrast, the GdK model assumes that the fracture channel is rectangular in cross-section. The shape of the fracture in the propagating direction is therefore elliptical and independent of *y*:

$$\frac{W(x)}{W_{max}} = \left[1 - \left(\frac{x}{L}\right)^2\right]^{\frac{1}{2}} \tag{3}$$

Finally, the penny model is parabolic in the radial propagation direction, r:

$$\frac{W(r)}{W_{max}} = \left(1 - \frac{r}{R}\right)^{1/2} \tag{4}$$

Where R is the extent of the fracture and is equivalent to L in equations (1–3).

The differing assumptions of these three models result in unique physical implications. All models taper significantly in fracture width with distance from the fracture origin (Figure 25D). The PKN model tapers marginally more than the GdK model from 0 to ~0.6 times the fracture extent, but then tapers significantly less for the remainder of the fracture length (Figure 25D). The parabolic shape of the penny model tapers the most throughout the fracture length (Figure 25D). The physical implication the penny model is that this parabolic taper is the result of flow divergence via outward propagation of the fracture in all directions in the x-z plane due to radial propagation (Figure 25C).

We use these three model geometries (i.e., equations [2-4]) to replicate high-angle dike behavior observed Moreno Gulch and Marca Canyon (Figure 26). We assume that the PGIC can be represented by a number of randomly placed, vertically oriented injectites of the same size (Figure 150C). By approximating PGIC exposures as planes that cut injectites at 37–45° relative to bedding (i.e., paleohorizontal), we can easily model injectite behavior in the field as a series of traverses intersecting a single injectite at the same angle, but at different positions (Figure 26A-D). Individual traverse apertures can then be summed and averaged in order to model bulk aperture behavior to compare to field results.

We modeled injectite geometry and aperture behavior for PKN, GdK, and penny geometries (Figures 26–27). Models result in unique exposure geometries dependent upon the location of the traverse on the injectite face (Figure 26D–F). Exposure geometries are analogous to injectite geometries seen in outcrop (e.g., Figures 21 and 22). The GdK model fails to reproduce the Type II geometry (Figure 26D). The PKN and the penny models reproduce both injectite geometries (Figure 26E–F).

All models result in decreasing average and cumulative aperture with stratigraphic distance from the point of injection (Figure 27). However, none of the models exhibit a truly linear correlation between aperture and stratigraphic position. The penny model exhibits the most linear correlation for average and cumulative aperture (R^2 = 0.91 and 0.96, respectively). The PKN model exhibits a more linear correlation than the GdK model for average aperture (R^2 = 0.85 vs. 0.80) and cumulative aperture (R^2 = 0.90 vs. 0.85).

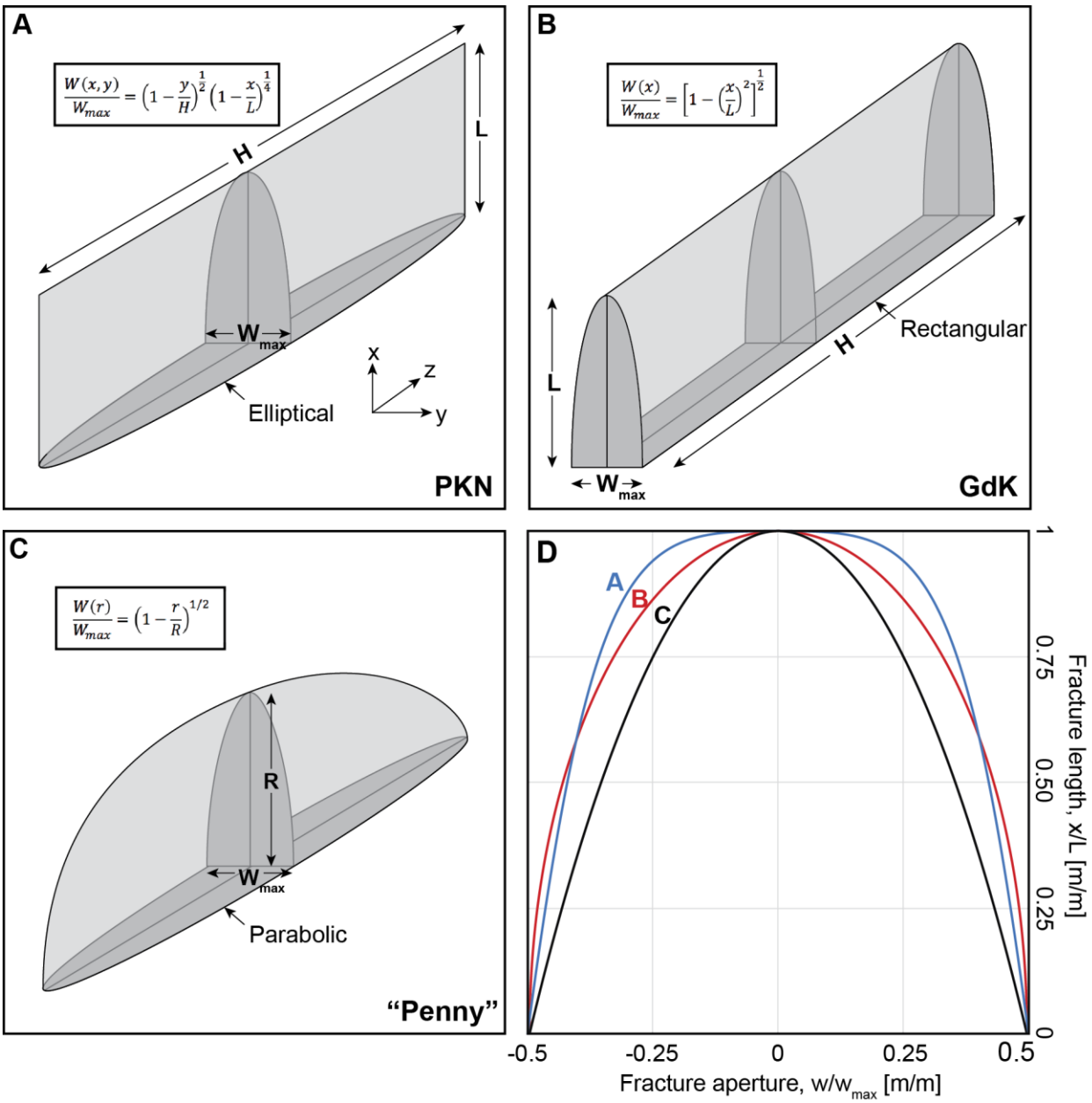

Figure 25: Illustration of fracture geometries in (A) PKN, (B) GdK, and (C) penny fracture models. (D) Fracture aperture versus fracture length for the three fracture models, defined by equations for width in (A–C).

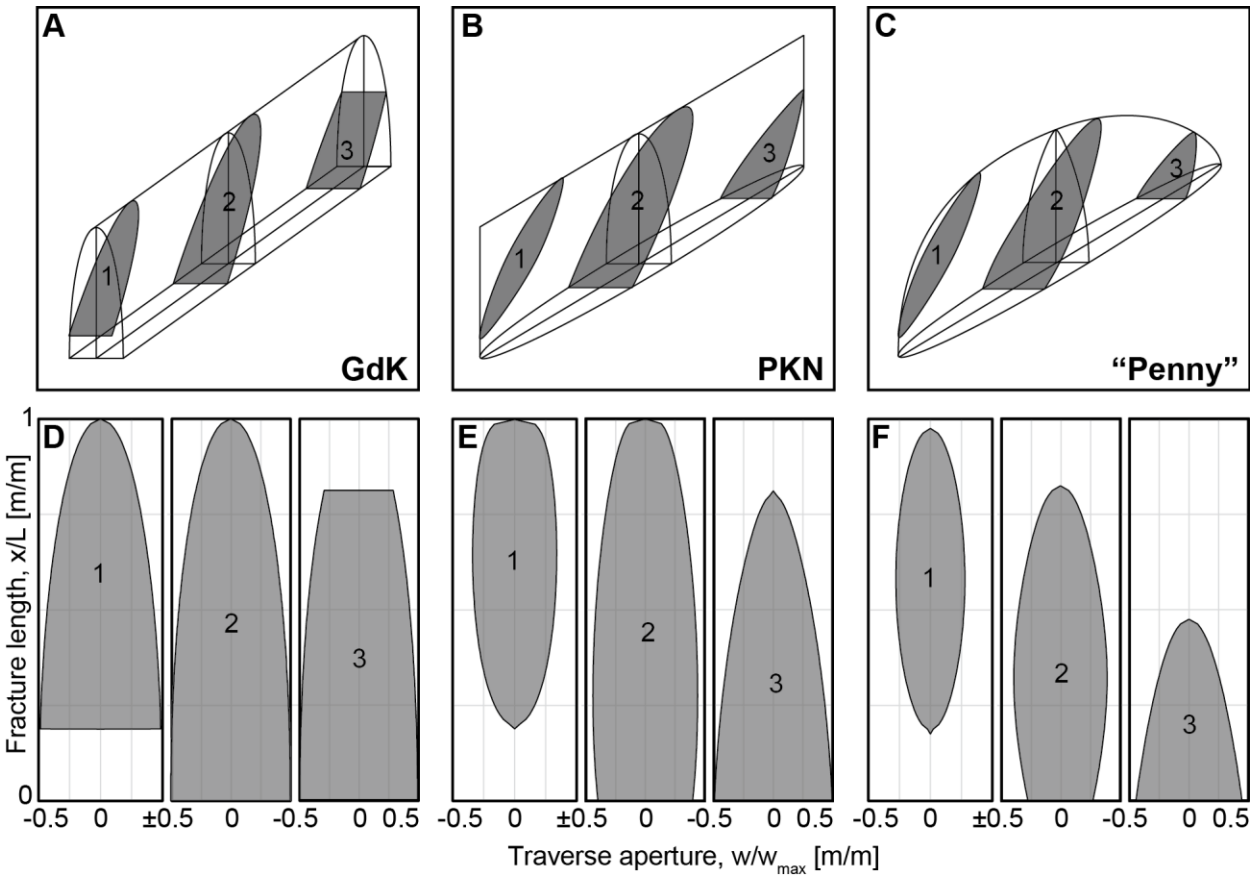

Figure 26: Traverse geometries for the three fracture models. (A–C) Cartoons of injectite geometries for GdK, PKN, and penny fracture models. (D–F) Aperture versus true stratigraphic position (TSP) for four traverses at at different points of the injectite geometries. These plots area analogous to injectite exposures in the field. Traverses are oriented 40° from horizontal.

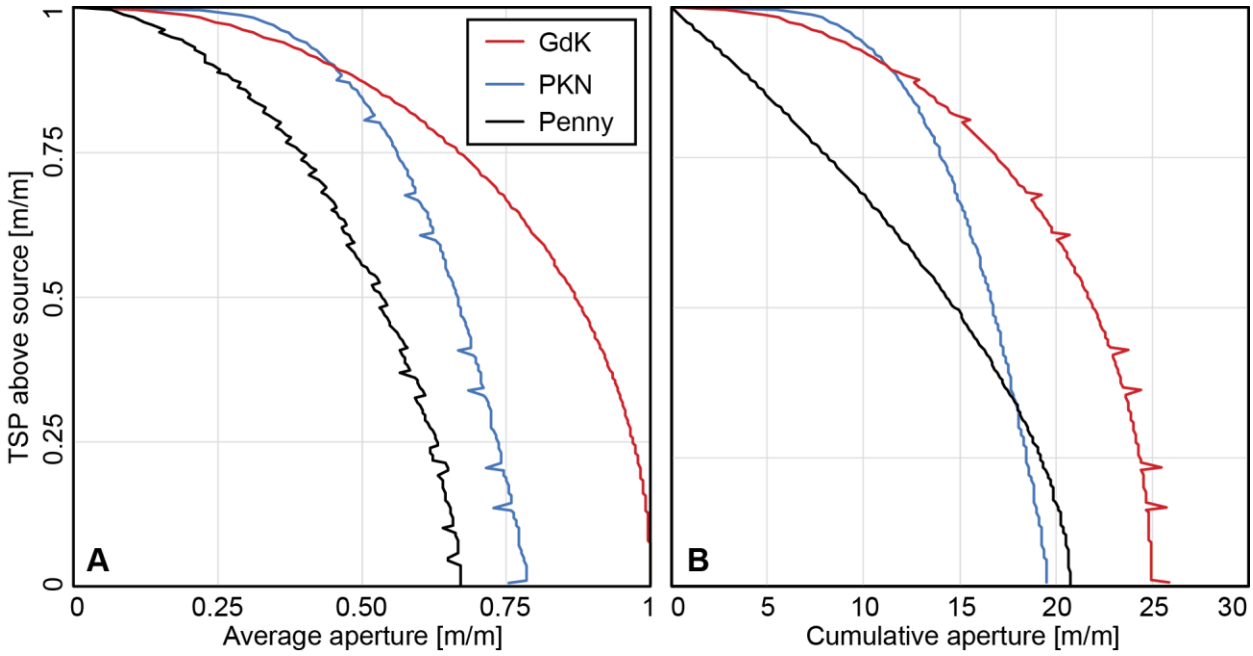

Figure 27: (A) Average and (B) normalized cumulative aperture of GdK (red), PKN (blue), and penny (black) geometries. Average and cumulative aperture are calculated from 40 equally spaced traverses oriented 40° from horizontal.

Chapter 10: Discussion

INJECTION GEOMECHANICS

Analysis of cumulative and individual aperture behavior of high-angle dikes in Moreno Gulch and Marca Canyon yields four insights:

1. Outcrop exposures traverse as much or more lateral stratigraphic distance than vertical, indicating that bulk aperture behavior is a composite of lateral and vertical changes away from the source.
2. Average aperture decreases linearly with distance from the injection source, indicating that individual injectites thin and diminish in number on a stratigraphic scale.
3. Cumulative aperture decreases linearly with proximity to the seafloor, indicating that bulk strain of injection diminishes from ~5% at the base of the dike zone to less than 1% near the paleoseafloor.
4. Individual injectites do not always conform to bulk trends, but rather exhibit Type I and II geometries.

An injectite model must replicate individual and cumulative aperture behavior. Specifically, a model must be able to reproduce both injectite geometries (i.e., Type I and II) and exhibit linearly decreasing average and cumulative aperture with distance from the source. We consider the GdK injectite model to be unsatisfactory because it fails to reproduce Type II injectite geometry. We deem the PKN and penny models to be valid because they reproduce both injectite geometries and roughly approximate average and cumulative aperture behavior (Figure 26 and 28). However, we favor the penny model because it produces a more linear correlation between aperture and stratigraphic position. Interestingly, a simpler radial model with a linear

taper approximates the field data far better than the parabolic penny model ("linear penny" in Figure 28).

We interpret that the PKN and penny models are valid because they incorporate laterally varying aperture behavior. The PKN model achieves lateral variation via vertical linear propagation of a crack that is elliptical in horizontal cross-section and fixed in length, whereas the penny model achieves lateral variation via radial flow divergence [*Abe et al.*, 1976; *J. Geertsma*, 1989; *Nordgren*, 1972; *Perkins and Kern*, 1961]. Therefore, the PKN model implies a linear source and the penny model implies a point source (Figure 29). While it is possible that injection initiates from a line source, it is implausible that an elliptical fracture would propagate vertically without diminishing in length with distance from the source. We therefore favor the penny model as the more geologically plausible model because it incorporates radial flow divergence away from a point source.

Though we favor the penny model, it exaggerates average aperture and, to a lesser degree, cumulative aperture relative to field data (Figure 28). We propose that this is due to the failure of the model to account for changing stress with depth. A model that accounts for changing stress with depth would result in a more pronounced taper. Consequently, average and cumulative aperture behavior of such a model would likely better approximate field behavior. Nevertheless, average and cumulative aperture behavior of the penny model approximate field results, indicating that the penny model is compatible with injectite geomechanics in the PGIC. We therefore conclude that injectites in the PGIC formed through radial propagation of fractures from a point source of injection.

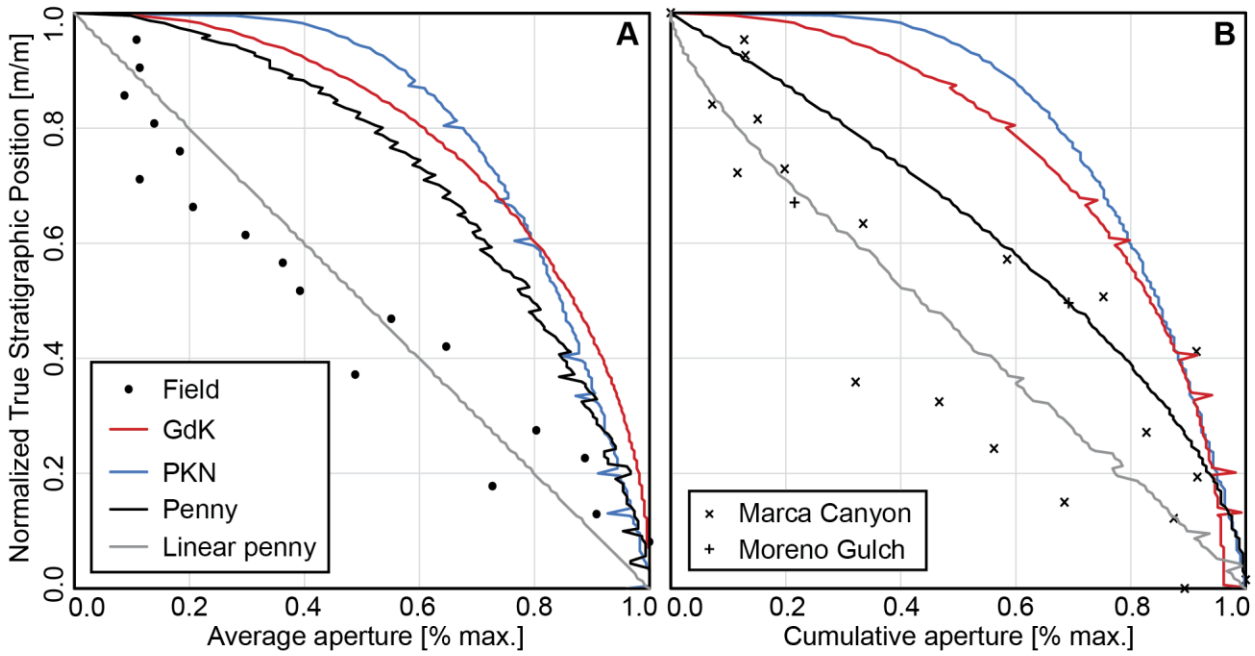

Figure 28: (A) Average and (B) normalized cumulative aperture of model geometries and field data. The grey line is the result of a linearly tapering penny model.

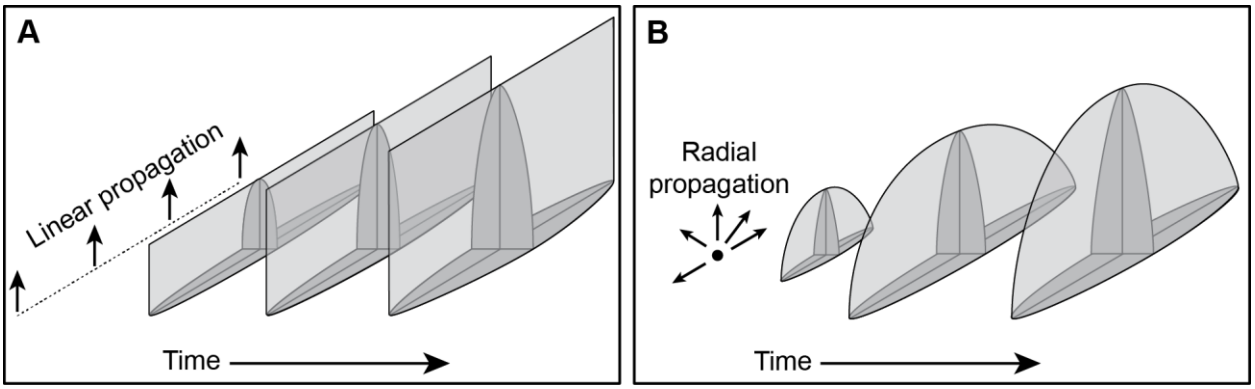

Figure 29: Illustration of (A) linear propagation from a linear source as per the PKN fracture model and (B) radial propagation from a point source as per the penny model.

TECTONIC CONTROL FOR INJECTION

High-angle dikes in Moreno Gulch and Marca Canyon are generally oriented NE-SW (~241° 71°). We interpret that dikes opened normal to the least principle stress [e.g., *Hubbert and Willis*, 1957; 1972; *Zoback et al.*, 1985], suggesting that the maximum horizontal stress at the time of injection was also oriented NE-SW. This NE-SW orientation of the maximum stress

is coincident with the trajectory of the Farallon plate in the Late Cretaceous and early Paleogene [*Bunge and Grand*, 2000; *Engebretson et al.*, 1985]. Likewise, the inferred NW-SE minimum horizontal stress orientation (~150°) is parallel to the margin of the westerly subduction zone in the Late Cretaceous and Early Paleogene [*Blakey*, 2013; *W R Dickinson*, 1976; *Ingersoll*, 1979]. We therefore conclude that the stress regime at the time of injection was tectonically controlled.

PALEOSTRESS REGIME AT THE PANOCHE GIANT INJECTION COMPLEX

We assume that tensile failure of hydraulic fractures occurs perpendicular to the orientation of the least principal stress (σ_3) [e.g., *Hubbert and Willis*, 1957; *Hubbert and Willis*, 1972] and infer the stress regime at the time of injection (Figure 30). Sills predominate the sill zone, indicating that the least principal stress was oriented vertically ($\sigma_3 = \sigma_v$) therein during injection. The presence of both dikes and sills in the SDTZ indicates that the vertical and minimum horizontal stresses were roughly isotropic ($\sigma_3 = \sigma_v \approx \sigma_h$). Finally, the predominance of high-angle injectites in the dike zone suggests that the minimum stress was oriented horizontally ($\sigma_3 = \sigma_h$) there. We therefore conclude a reverse stress state ($\sigma_v = \sigma_3$) in the sill zone, a reverse/strike-slip stress state ($\sigma_v \approx \sigma_h = \sigma_3$) in the SDTZ, and a normal or strike-slip stress state ($\sigma_h = \sigma_3$) in the dike zone at the time of injection (Figure 30).

These conclusions indicate a transition in stress state from reverse to normal or strike-slip with proximity to the seafloor at the time of injection. We propose that stress state was generally static (i.e., stress state at a given depth did not change over the duration of PGIC injection) but varied as a function of depth. In this model, stress state rotates from reverse to normal/strike-slip with proximity to the seafloor (Figure 30). Injectites propagate first as subhorizontal sills within the reverse stress regime of the sill zone, perpendicular to overburden (i.e., the least principal stress). These sills occasionally step up along planes of weakness (i.e., existing fractures) or

mechanical anisotropy (i.e., lithologic heterogeneity), gradually ascending the Moreno Formation as the magnitude of σ_h relative to that of σ_v decreases. As σ_h approaches σ_v in magnitude, injection style transitions gradually from sills to low-angle and high-angle injections, with the latter becoming increasingly predominant as σ_h continues to decrease relative to σ_h (Figure 30).

The strong NE-SW orientation preference of high-angle dikes in the SDTZ and dike zone indicates that the horizontal stresses were anisotropic ($\sigma_H >> \sigma_h$) at the time of injection in both intervals (Figure 30). While we cannot definitively conclude the same for the sill zone, it is logical to assume that this horizontal stress anisotropy would only increase with depth, given the tectonic setting. We cannot distinguish the stress regime of the dike zone as normal ($\sigma_v > \sigma_H > \sigma_h$) or strike-slip ($\sigma_H > \sigma_v > \sigma_h$), as we are unable to evaluate the magnitude of σ_H relative to σ_v.

No previous work has invoked a stress-state reversal to explain PGIC architecture. Alternatively, some authors have explained architecture with changes in pore pressure magnitude relative to magnitude of the vertical stress. *Vigorito and Hurst* [2010] propose that pore pressure was supralithostatic lower in the PGIC, resulting in sill emplacement there. *Vétel and Cartwright* [2010] report that sills are present throughout the PGIC, and therefore interpret that pore pressure was supralithostatic throughout injected interval.

The proposed phenomenon of stress-state reversal with depth has precedent in other forearc basins. *Chang et al.* [2010] report a similar phenomenon in the modern Kumano forearc basin and Nankai accretionary wedge, offshore Japan (Figure 156B). By in situ stress estimation from wellbore failures (i.e., borehole breakouts and drilling-induced tensile fractures) in four vertical boreholes, *Chang et al.* [2010] demonstrate that the stress state generally transitions from normal to strike-slip with depth. In one borehole (C0001), they demonstrate that stress state

transitions from normal to reverse over virtually the same scale (~600 m) proposed in the PGIC (Figure 156). *Chang et al.* [2010] propose stress partitioning across geologic domains (i.e., forearc basin versus accretionary wedge) as a potential cause of this phenomenon of stress-state reversal. Similarly, the proposed stress-state reversal in the PGIC could be explained by the increasing influence of gravity-driven extension and decreasing influence of subduction-driven compression with proximity to the seafloor.

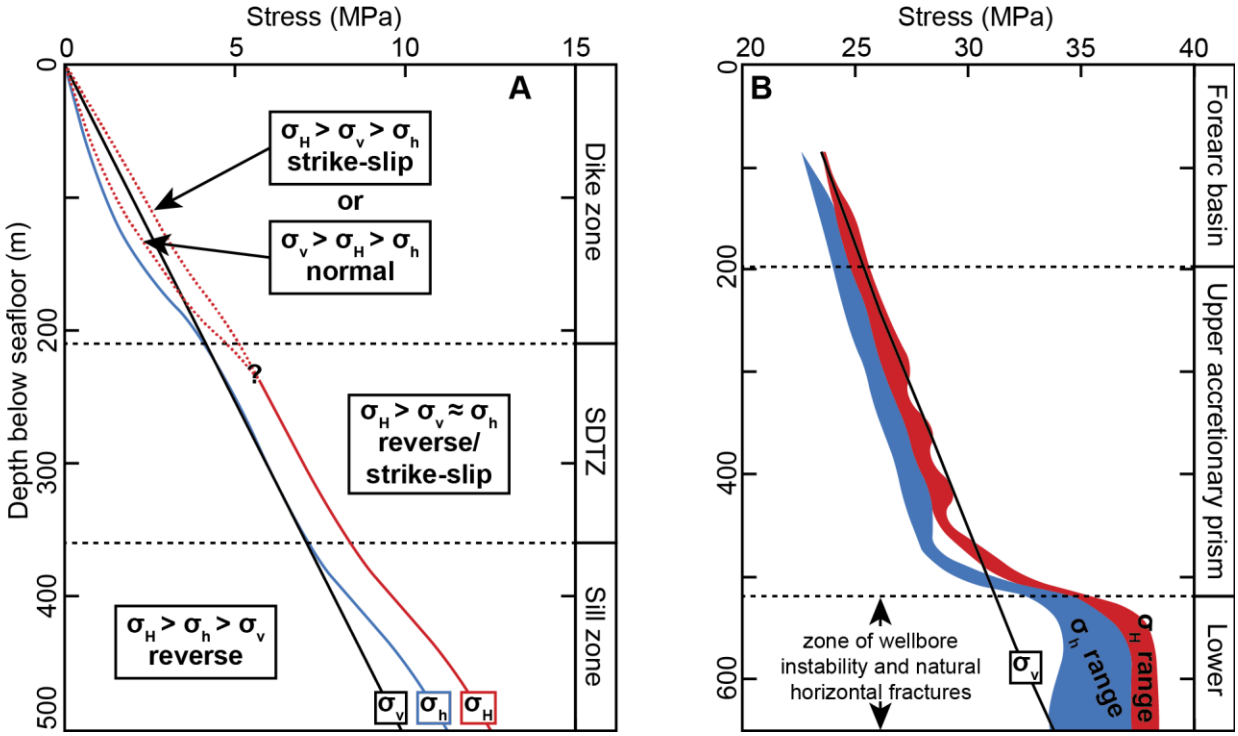

Figure 30: (A) Schematic pore pressure profile of the PGIC illustrating rotation of stress state from reverse to normal or strike-slip with proximity to the seafloor. Vertical stress is based on an assumed bulk density of 2,000 kg/m^3. (B) Pore pressure profile of the Kumano forearc basin and Nankai accretionary prism calculated from borehole failures by *Chang et al.* [2010]. Vertical stress is determined from bulk density logs. Modified from *Chang et al.* [2010].

DURATION AND PERIODICITY OF INJECTION

We estimate that the PGIC was a complete and active system for ~0.8–1 My in the Danian. This estimate is based on an 80–100 m thick extrudite interval and a compacted sedimentation rate of 100 m/Ma for the Dos Palos Shale Member as per *McGuire* [1988], and is within the range of 0.5–2 My reported by *Schwartz et al.* [2003] and *Minisini and Schwartz* [2007] based on carbonate paleoseep deposits in the PGIC. Furthermore, thickness between discrete extrudite horizons indicates that activity was punctuated by ~20–150 ky periods of quiescence. Given the poor quality of outcrops in the Dos Palos and constituent Cima Lentil, as well as the unknown origin (i.e., depositional or extruded) of slope-forming sands hosting extrudite mounds in the Cima Lentil, the upper bound of this range is possibly inflated.

Chapter 11: Summary and conclusions

Through field observation, measurement, and mapping of the PGIC we produce several important insights regarding architecture of the PGIC and geomechanical controls thereon:

1) The PGIC is a complete injectite system, with source, injectites, and extrudites readily observable in the field. This system was complete and episodically extruding sand onto the paleoseafloor over ~1 My in the Danian, punctuated by ~20–150 ky-long periods of quiescence.
2) The NE-SW orientation preference of high-angle dikes indicate that subduction of the Farallon plate controlled the stress regime at the site of injection.
3) The PGIC exhibits a tripartite injectite architecture that indicates a stress state reversal from reverse to normal or strike-slip with proximity to the seafloor. We propose that this was a static stress state imposed on Late Cretaceous sediments by competition of gravity-driven extension in the shallow subsurface of the forearc basin and subduction-driven compression at depth, similar to the modern Kumano forearc basin.
4) Injectites were emplaced via radial propagating hydraulic fractures. Because injectites are radial features and were formed via flow divergence, injectite aperture and bulk strain decreases radially away from the injection source.

Appendices

APPENDIX 1: DETAILED MAPPING METHODOLOGY OF THE CRETACEOS-PALEOGENE BOUNDARY DEPOSIT

Landmark DecisionSpace Desktop was used for seismic and borehole data interpretation and grid generation. Specifically, the Frameworks to Fill module was used to define surfaces by a single seismic horizon, relate it to a single well surface, and output a grid that synthesized and interpolated seismic and borehole data. Furthermore, the Frameworks to Fill module allowed the top and base of the boundary unit to be hierarchically and stratigraphically "linked" via the module's "Conformance" feature, so that the base of the KPBD horizon conformed to that of the top when the former was null. Such a method essentially automates the assumption that interval thickness is constant unless defined otherwise by data.

The paucity and variability of well and seismic control for mapping in certain areas (e.g., Louann salt basin, inland of the seismic data limit, etc.) made it necessary to tailor methods of mapping to maximize coverage while ensuring reliability. After experimentation and comparison of results, spline interpolation was determined to honor and interpolate the data best, and thus was used for all computer-generated maps (Table A1). In the case of maps of the deposit within the impact basin, it was deemed appropriate to interpretively hand-contour seismic and borehole data together and then grid seismic and borehole data with the contours as an added control.

Generally, density of data used in this study is higher in the eastern Gulf than in the western Gulf, and density onshore is generally lower and much more variable, as borehole data comprise virtually all onshore control (Figure 1). For this reason, cell size used for gridding was smallest in the eastern Gulf, moderate in the western Gulf, and largest onshore (Table A5). Given

the limited extent of data within the impact basin and control by interpretive contours, mapping at the crater employed the smallest cell size (Table A5).

After grids were generated with Landmark DecisionSpace, they were imported into ESRI ArcGIS for minor processing, including grid merging, up-sampling of grid size, unit conversion, and contour generation. In the case of maps with multiple grids with unique cell sizes, cell size of grids were upsampled and smoothed as necessary prior to merging into a single grid. For example, in the case of the regional structure map, the grid in the western Gulf (approx. 84 km cell size) was upsampled to match the cell size of the eastern Gulf grid (approx. 9 km cell size), then smoothed using the Focal Statistics tool and merged with the other grids. This process is cosmetic (i.e., to eliminate a "pixelated" appearance), and does not appreciably distort the grid.

Volumetric calculation from the resultant interval thickness map was performed using the Zonal Statistics tool in ArcMap. In order to determine total volume of sediment from the results of the Zonal Statistics tool, average thickness was determined by dividing the cumulative thickness of all cells (the sum of the "SUM" field) by the total number of cells (the sum of the "COUNT" field), and grid area was determined by multiplying the total number of cells by the cell size (Table A5). Average thickness was then multiplied by the calculated grid area to calculate the total sediment volume. For volumetric estimate in the southern Gulf, the area of the southern paleo-Gulf was determined from the 65 Ma North American paleogeographic map of *Blakey* [2011], and the average KPBD thickness determined for the northern Gulf was applied to the resultant area.

	Thickness (m)	Proximity (m)	Paleogeographic setting	Reference publication
Shell Creek	0.75	<5000	shallow-water	[*King and Petruny*, 2007]
Brazos River	1	<5000	shallow-water	[*Smit et al.*, 1996]
Crowley's Ridge	1.85	<5000	shallow-water	[*Campbell et al.*, 2007]
El Penon	7.5	<5000	shallow-water	[*Smit et al.*, 1996; *Stinnesbeck et al.*, 1993]
Moscow Landing	9	<5000	shallow-water	[*Hart et al.*, 2013]
Mussel Creek	9.5	<5000	shallow-water	[*Hart et al.*, 2013]
Braggs	10	<5000	shallow-water	[*Hart et al.*, 2013]
El Tecolote	12	<5000	shallow-water	[*Soria et al.*, 2001]
New Madrid	1	<5000	shallow-water	[*Frederiksen et al.*, 1982]
Coxquihui	0.88	<1000	shallow-water	[*Smit et al.*, 1996]
Lajilla	1.1	<1000	shallow-water	[*Smit et al.*, 1996]
La Ceiba	1.7	<1000	shallow-water	[*Smit et al.*, 1996]
El Mimbral	3	<1000	shallow-water	[*Smit et al.*, 1996]
Actela	15	<1000	shallow-water	[*Fourcade et al.*, 1998]
Guayal	51	<1000	shallow-water	[*Grajales-Nishimura et al.*, 2000]
Bochil	61*	<1000	shallow-water	[*Grajales-Nishimura et al.*, 2000; *Smit et al.*, 1996]
Moncada	1.9	<500	shallow-water	[*Tada et al.*, 2002]
Armenia	13	<500	shallow-water	[*Pope et al.*, 2005]
Albion Island	16	<500	shallow-water	[*Ocampo et al.*, 1996]
DSDP Leg 77	50	<1000	deepwater†	[*W Alvarez et al.*, 1992; *Bralower et al.*, 1998] and this study
Penalver	180	<1000	deepwater	[*Tada et al.*, 2003]
Cantarell	275	<500	deepwater	[*Cantu-Chapa and Landeros-Flores*, 2001]
Cacarajicara	750	<500	deepwater	[*Kiyokawa et al.*, 2002]

*_Smit et al._ [1996] does not consider <50 m breccia unit as part of KPBD.
†DSDP Leg 77 sites are on uplifted basement blocks, and therefore likely condensed (see text).

Table 7: Thickness, proximity, and paleogeographic setting of KPBD locales in the circum-Gulf region.

Type	Wave velocity (km/s)	Wave velocity (km/min)
P-wave*	5.0	300
S-wave†	3.0	180
Rayleigh wave‡	2.7	160
Megatsunami wave§	0.25	15

*Approximate average acoustic velocity for carbonates [e.g., *Burger et al.*, 2006; *Milsom*, 2007].
†Taken to be 60% of P-wave as per *Burger et al.* [2006].
‡Taken to be 90% of S-wave velocity as per *Burger et al.* [2006].
§Per *S N Ward* [2011] for maximum tsunami velocity in 6-km water depth.

Table 8: Velocities for seismic and megatsunami waves used for first arrival calculation.

Locale	Distance from crater (km)	Ground-roll arrival (min)	Megatsunami arrival (min)
Campeche Escarpment	210	1.3	14
Yucatán Platform margin (at DSDP Leg 77 Sites)	510	3.1	34
Florida Platform margin	800	4.9	53
Paleo–Florida coast*	1,120	6.9	75
Paleo–Texas coast*	1,130	7.0	76

*Rayleigh wave energy (i.e., ground-roll) is assumed to be the primary destructive seismic energy.
†Measured from 65 Ma North American paleogeographic map of *Blakey* [2011].

Table 9: Data sources for seismic and borehole data used in this study.

Locale	Sub-locale*	Type	Source (dataset name)	Location
Offshore northern Gulf	All	2-D seismic depth	IonGeoventures (GulfSPAN)	Proprietary
	All	2-D seismic depth	Fugro (DeepEast & DeepFocus)	Proprietary
	All	Borehole	U.S. Bureau of Ocean Energy Management	data.boem.gov
	GC, WR, AT	3-D seismic depth	WesternGeco (E-Dog)	Proprietary
	All	2-D seismic depth	IonGeoventures (LandSPAN)	Proprietary
Onshore northern Gulf	TX	Borehole	Texas Railroad Commission	rrc.state.tx.us
	LA	Borehole	Louisiana Department of Natural Resources	sonris.com
	MS	Borehole	Mississippi Oil & Gas Board	ogb.state.ms.us
	AL	Borehole	Alabama State Oil & Gas Board	gsa.state.al.us
	FL	Borehole	Florida Department of Environmental Protection	dep.state.fl.us
	MO	Borehole	U.S. Geological Survey	[*Frederiksen et al.*, 1982]
	All	2-D seismic time	University of Texas Institute for Geophysics Seismic Data Center	Restricted (ig.utexas.edu/sdc) [*Shipley et al.*, 2013]
Southern Gulf	Chicxulub Crater	2-D seismic time†	University of Texas Institute for Geophysics Seismic Data Center	ig.utexas.edu/sdc (Cruise #96L676 & EW0501) [*Gulick and Barton*, 2005; *Gulick et al.*, 2008; *Morgan et al.*, 2005]
		Borehole	Petróleos Mexicanos (Pemex)	[*Sharpton et al.*, 1994; *Sharpton et al.*, 1996; *W C Ward et al.*, 1995]
	DSDP Leg 77	Core	Integrated Ocean Drilling Project (IODP)	Gulf Coast Repository (iodp.tamu.edu)

*GC = Green Canyon; WR = Walker Ridge; AT = Atwater Valley; TX = Texas; LA = Louisiana; MS = Mississippi; AL = Alabama; FL = Florida; MO = Missouri
†Depth-converted for this study

Table 10: Sources of seismic and borehole data used in this study.

Locale	Map	Cell size (km^2)			Gridding method
		Onshore	West	East	
Northern Gulf	Structure (Figure 7)	83.61	37.16	9.29	Spline
	Interval thickness (Figure 8)	83.61	37.16	9.29	Spline
Chicxulub impact basin	Structure (Figure 10)		2.32		Hand-contour, spline
	Interval thickness (Figure 11)		2.32		Hand-contour, spline

Table 11: Mapping parameters used in this study

APPENDIX 2: CORE DESCRIPTION OF THE CRETACEOUS-PALEOGENE BOUNDARY DEPOSIT AT DSDP LEG 77 SITES 536 AND 540

Core descriptions of the KPBD at DSDP Leg 77 Sites 536 and 540 begin on the following page.

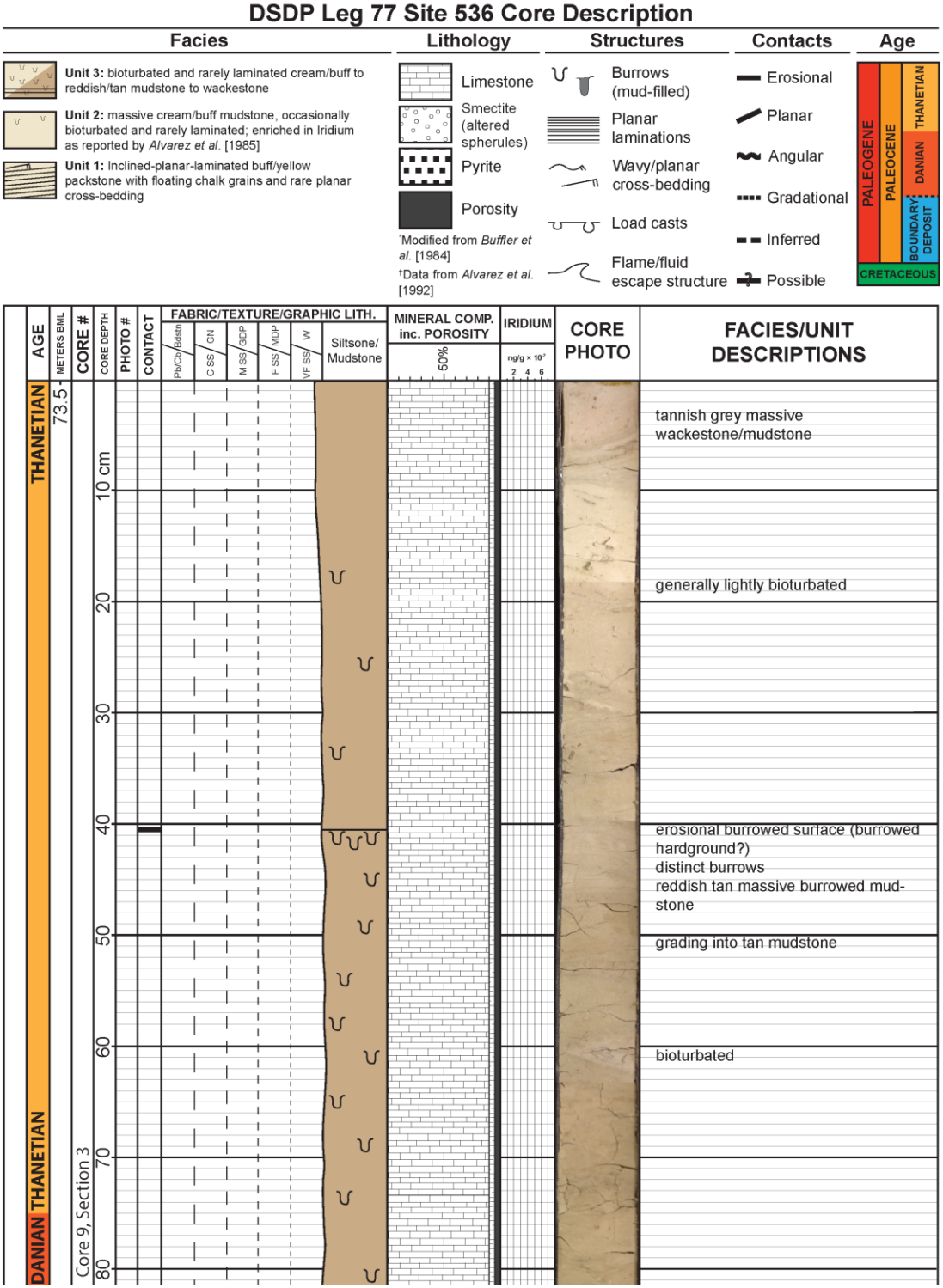
DSDP Leg 77 Site 536 Core Description
Facies
Unit 3: bioturbated and rarely laminated cream/buff to reddish/tan mudstone to wackestone
Unit 2: massive cream/buff mudstone, occasionally bioturbated and rarely laminated; enriched in Iridium as reported by Alvarez et al. [1985]
Unit 1: Inclined-planar-laminated buff/yellow packstone with floating chalk grains and rare planar cross-bedding
Lithology
Limestone
Smectite (altered spherules)
Pyrite
Porosity
*Modified from Buffler et al. [1984]
†Data from Alvarez et al. [1992]
Structures
Burrows (mud-filled)
Planar laminations
Wavy/planar cross-bedding
Load casts
Flame/fluid escape structure
Contacts
Erosional
Planar
Angular
Gradational
Inferred
Possible
Age
PALEOGENE
PALEOCENE
THANETIAN
DANIAN
BOUNDARY DEPOSIT
CRETACEOUS
AGE
METERS BML
CORE #
CORE DEPTH
PHOTO #
CONTACT
FABRIC/TEXTURE/GRAPHIC LITH.
Pb/Cb/Bdstn
C SS/GN
M SS/GDP
F SS/MDP
VF SS/W
Siltsone/ Mudstone
MINERAL COMP. inc. POROSITY
50%
IRIDIUM
ng/g × 10⁻⁷
2 4 6
CORE PHOTO
FACIES/UNIT DESCRIPTIONS
THANETIAN
DANIAN
73.5
Core 9, Section 3
10 cm
20
30
40
50
60
70
80
tannish grey massive wackestone/mudstone
generally lightly bioturbated
erosional burrowed surface (burrowed hardground?)
distinct burrows
reddish tan massive burrowed mud-stone
grading into tan mudstone
bioturbated

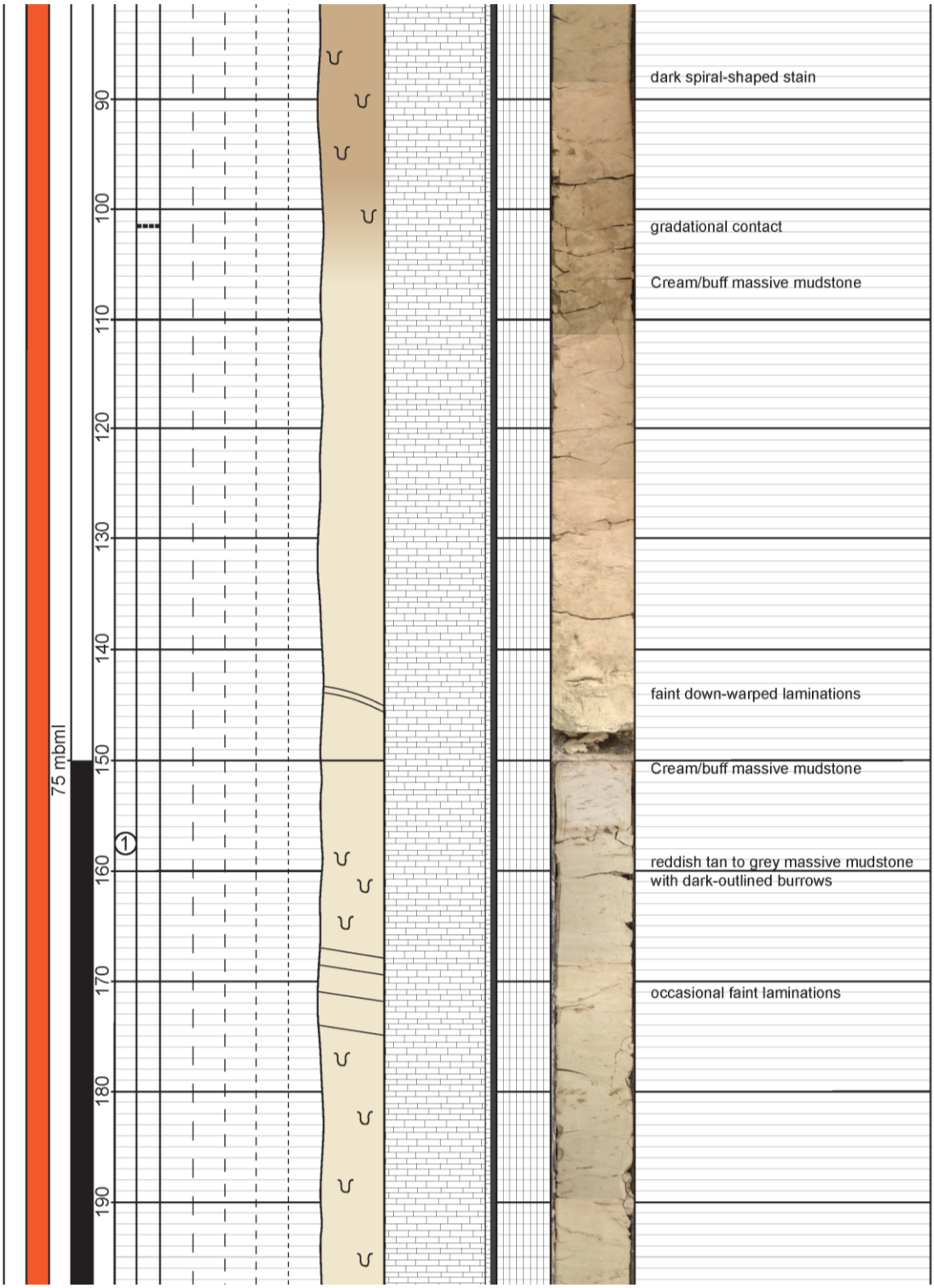
75 mbml
90
100
110
120
130
140
150
160
170
180
190
dark spiral-shaped stain
gradational contact
Cream/buff massive mudstone
faint down-warped laminations
Cream/buff massive mudstone
reddish tan to grey massive mudstone
with dark-outlined burrows
occasional faint laminations

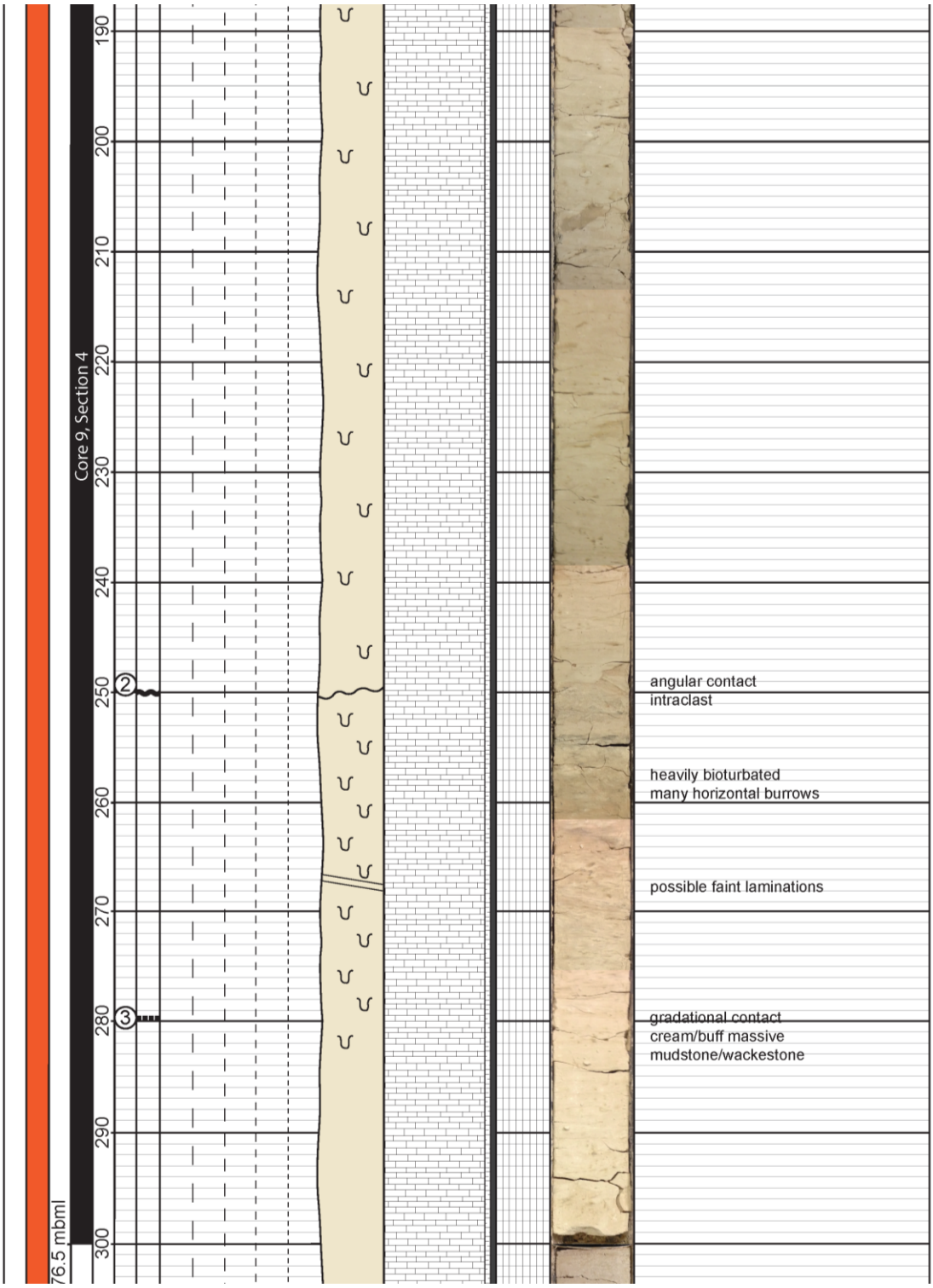
Core 9, Section 4
176.5 mbml
190
200
210
220
230
240
250
260
270
280
290
300
2
3
angular contact
intraclast
heavily bioturbated
many horizontal burrows
possible faint laminations
gradational contact
cream/buff massive
mudstone/wackestone

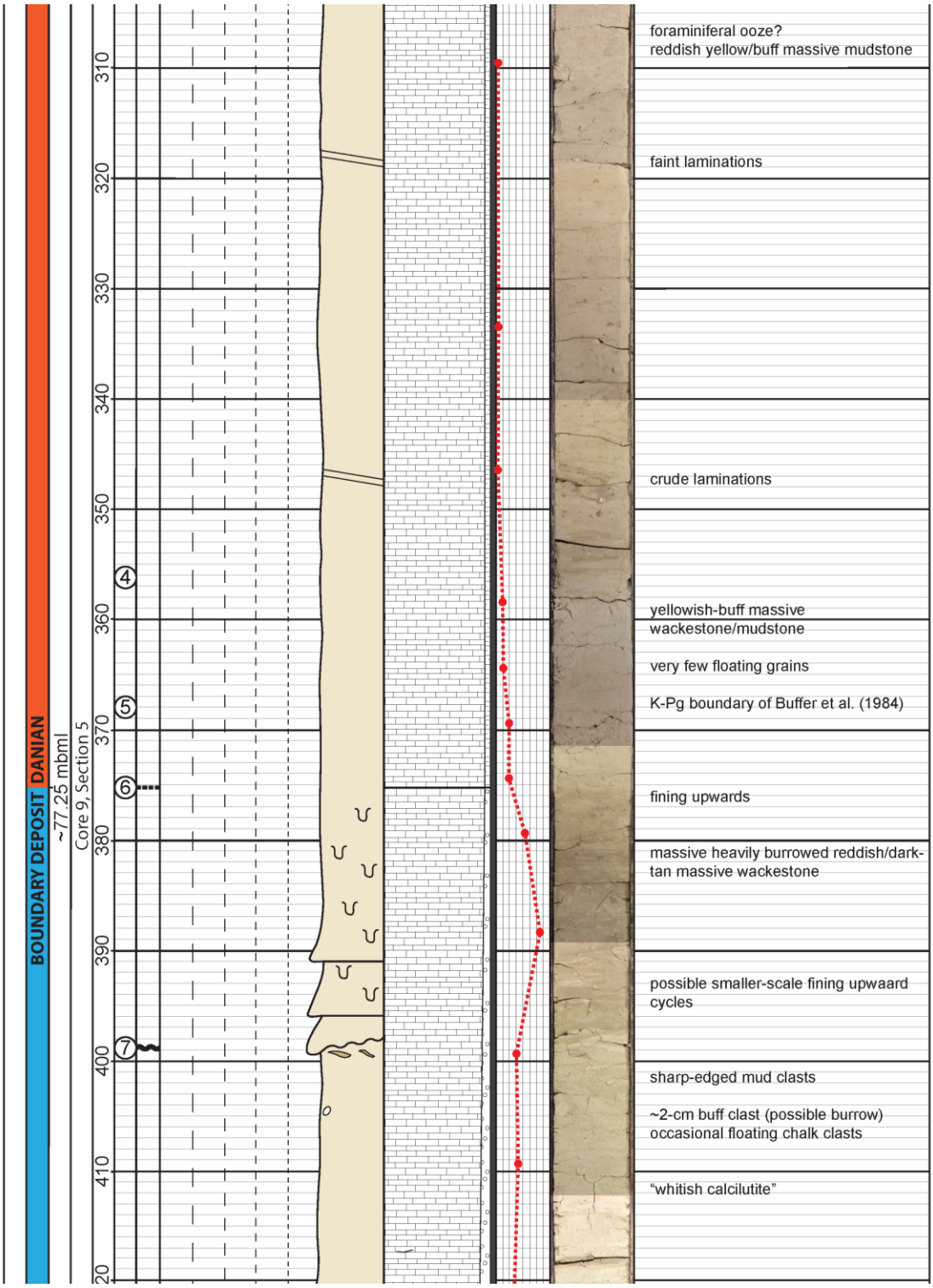
BOUNDARY DEPOSIT DANIAN
~77.25 mbml
Core 9, Section 5
310
320
330
340
350
360
370
380
390
400
410
420
4
5
6
7
foraminiferal ooze?
reddish yellow/buff massive mudstone
faint laminations
crude laminations
yellowish-buff massive
wackestone/mudstone
very few floating grains
K-Pg boundary of Buffer et al. (1984)
fining upwards
massive heavily burrowed reddish/dark-
tan massive wackestone
possible smaller-scale fining upwaard
cycles
sharp-edged mud clasts
~2-cm buff clast (possible burrow)
occasional floating chalk clasts
"whitish calcilutite"

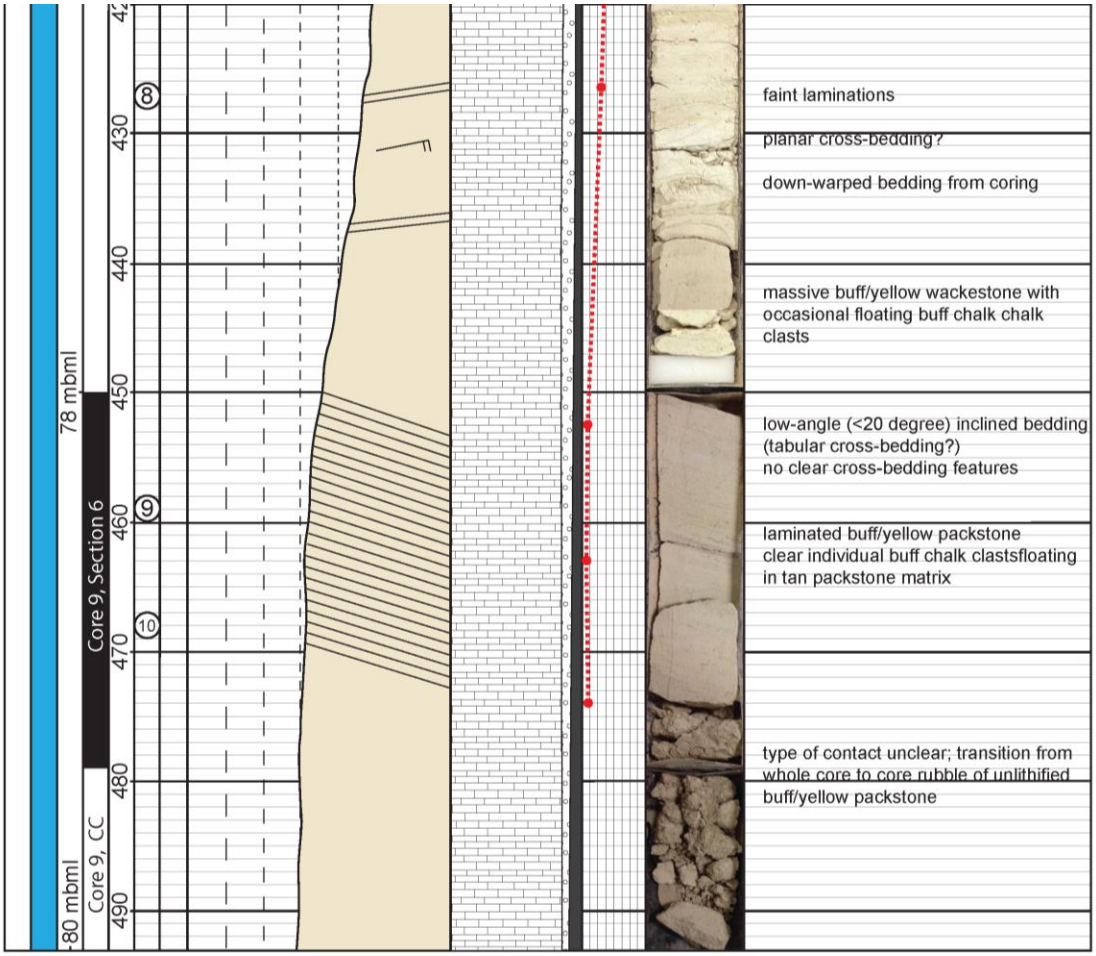
78 mbml
80 mbml
Core 9, Section 6
Core 9, CC
430
440
450
460
470
480
490
faint laminations
planar cross-bedding?
down-warped bedding from coring
massive buff/yellow wackestone with occasional floating buff chalk chalk clasts
low-angle (<20 degree) inclined bedding (tabular cross-bedding?)
no clear cross-bedding features
laminated buff/yellow packstone
clear individual buff chalk clastsfloating in tan packstone matrix
type of contact unclear; transition from whole core to core rubble of unlithified buff/yellow packstone

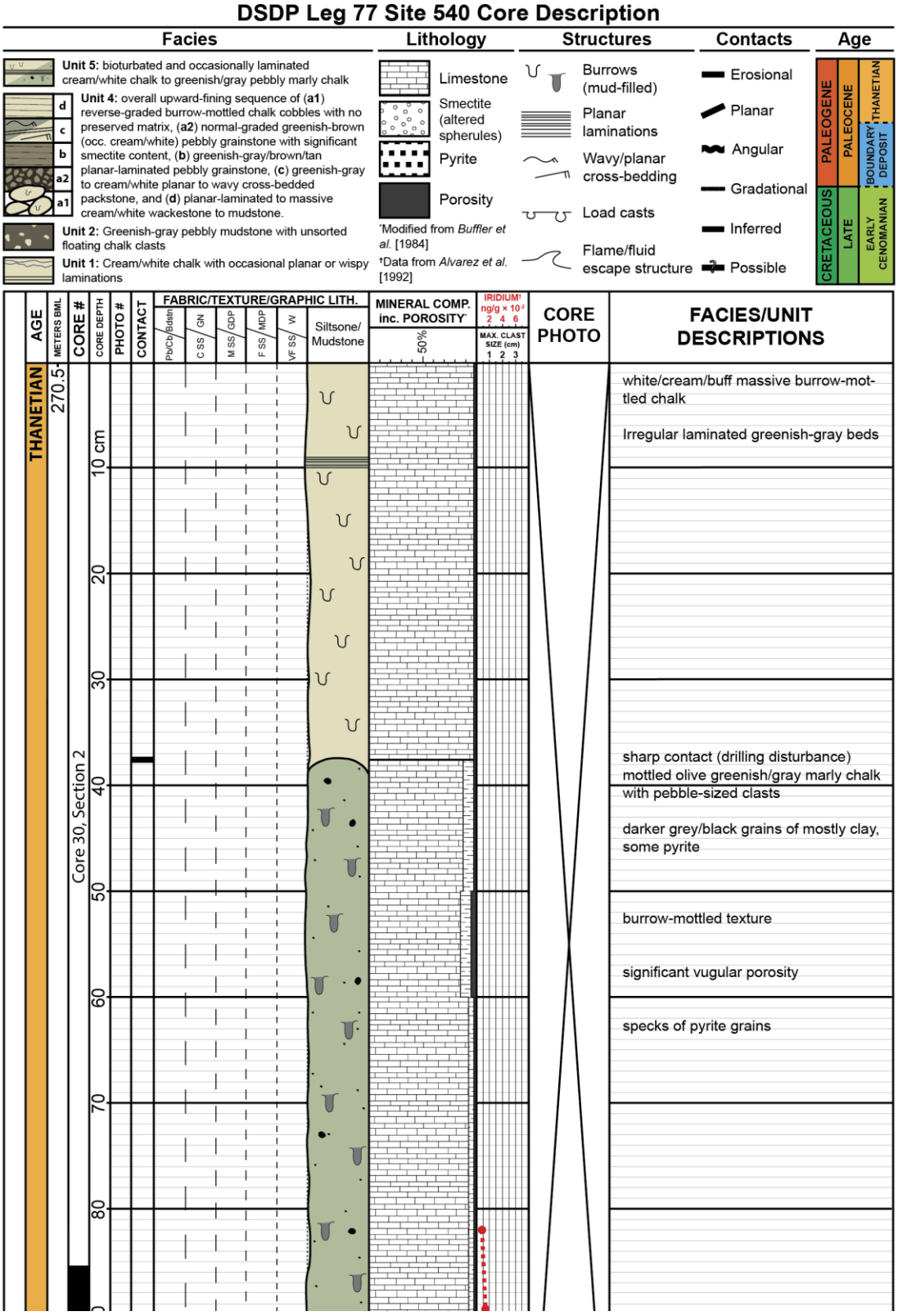
DSDP Leg 77 Site 540 Core Description
Facies
Unit 5: bioturbated and occasionally laminated cream/white chalk to greenish/gray pebbly marly chalk
Unit 4: overall upward-fining sequence of (a1) reverse-graded burrow-mottled chalk cobbles with no preserved matrix, (a2) normal-graded greenish-brown (occ. cream/white) pebbly grainstone with significant smectite content, (b) greenish-gray/brown/tan planar-laminated pebbly grainstone, (c) greenish-gray to cream/white planar to wavy cross-bedded packstone, and (d) planar-laminated to massive cream/white wackestone to mudstone.
Unit 2: Greenish-gray pebbly mudstone with unsorted floating chalk clasts
Unit 1: Cream/white chalk with occasional planar or wispy laminations
Lithology
Limestone
Smectite (altered spherules)
Pyrite
Porosity
*Modified from Buffler et al. [1984]
†Data from Alvarez et al. [1992]
Structures
Burrows (mud-filled)
Planar laminations
Wavy/planar cross-bedding
Load casts
Flame/fluid escape structure
Contacts
Erosional
Planar
Angular
Gradational
Inferred
Possible
Age
PALEOGENE
PALEOCENE
THANETIAN
BOUNDARY DEPOSIT
CRETACEOUS
LATE
EARLY CENOMANIAN
AGE
METERS BML
CORE #
CORE DEPTH
PHOTO #
CONTACT
FABRIC/TEXTURE/GRAPHIC LITH.
Pb/Cb/Bdstn
C SS/GN
M SS/GDP
F SS/MDP
VF SS/W
Siltsone/ Mudstone
MINERAL COMP. inc. POROSITY*
50%
IRIDIUM† ng/g × 10⁻²
2 4 6
MAX. CLAST SIZE (cm)
1 2 3
CORE PHOTO
FACIES/UNIT DESCRIPTIONS
THANETIAN
270.5-
Core 30, Section 2
10 cm
20
30
40
50
60
70
80
white/cream/buff massive burrow-mottled chalk
Irregular laminated greenish-gray beds
sharp contact (drilling disturbance)
mottled olive greenish/gray marly chalk with pebble-sized clasts
darker grey/black grains of mostly clay, some pyrite
burrow-mottled texture
significant vugular porosity
specks of pyrite grains

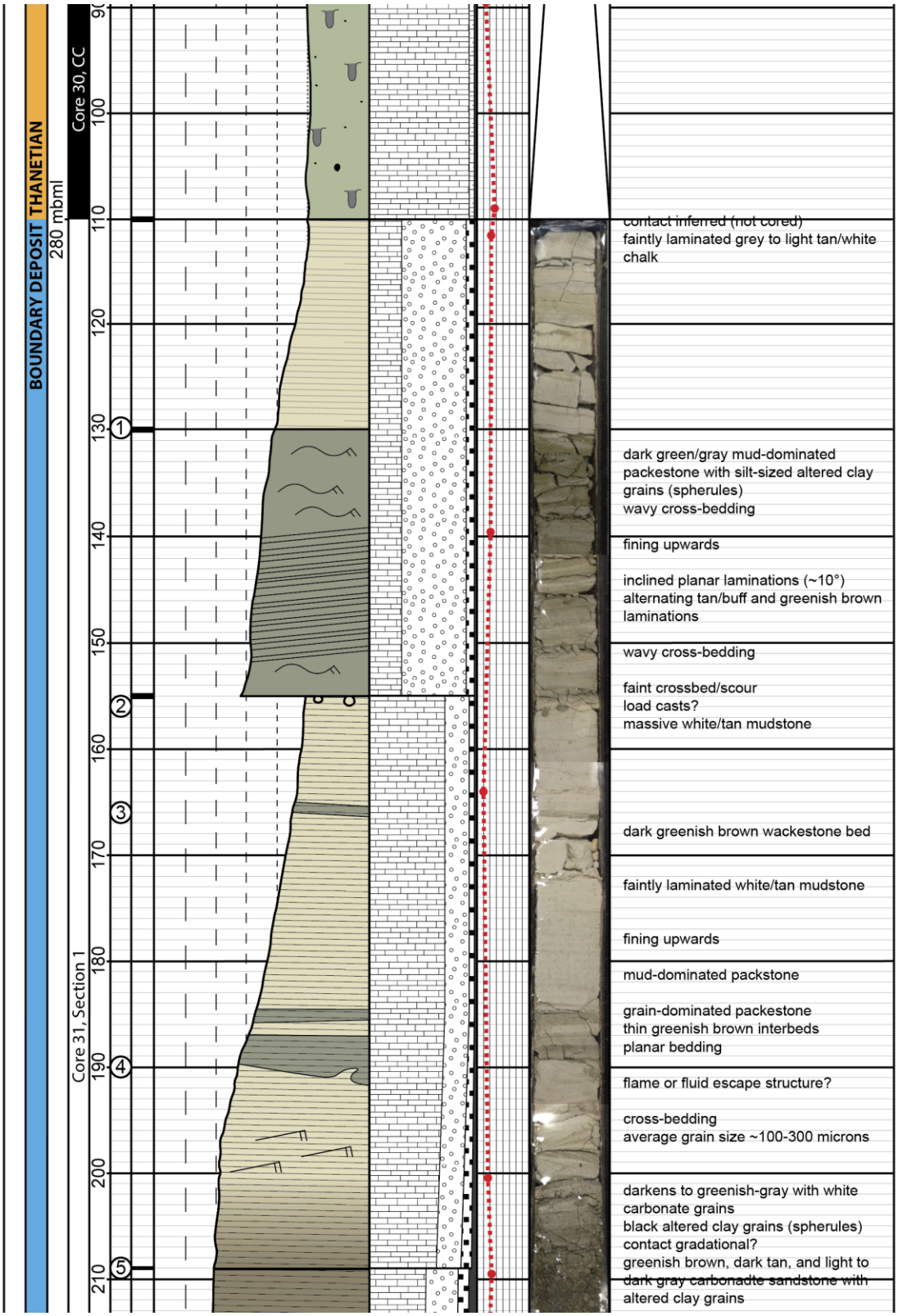
BOUNDARY DEPOSIT THANETIAN
280 mbml
Core 30, CC
Core 31, Section 1
90
100
110
120
130
140
150
160
170
180
190
200
210
1
2
3
4
5
contact inferred (not cored)
faintly laminated grey to light tan/white chalk
dark green/gray mud-dominated packestone with silt-sized altered clay grains (spherules)
wavy cross-bedding
fining upwards
inclined planar laminations (~10°) alternating tan/buff and greenish brown laminations
wavy cross-bedding
faint crossbed/scour
load casts?
massive white/tan mudstone
dark greenish brown wackestone bed
faintly laminated white/tan mudstone
fining upwards
mud-dominated packstone
grain-dominated packestone
thin greenish brown interbeds
planar bedding
flame or fluid escape structure?
cross-bedding
average grain size ~100-300 microns
darkens to greenish-gray with white carbonate grains
black altered clay grains (spherules)
contact gradational?
greenish brown, dark tan, and light to dark gray carbonadte sandstone with altered clay grains

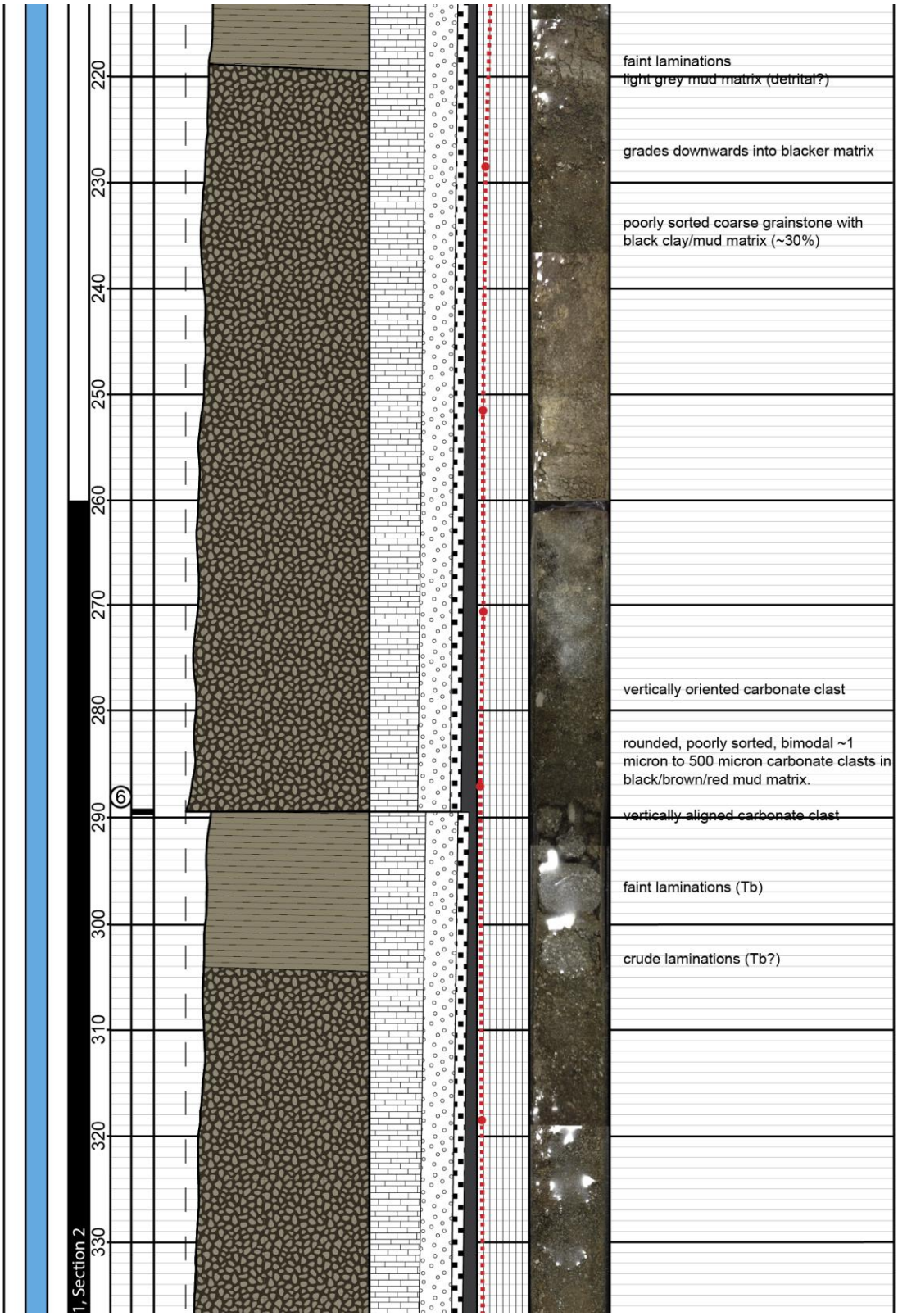
faint laminations
light grey mud matrix (detrital?)
grades downwards into blacker matrix
poorly sorted coarse grainstone with
black clay/mud matrix (~30%)
vertically oriented carbonate clast
rounded, poorly sorted, bimodal ~1
micron to 500 micron carbonate clasts in
black/brown/red mud matrix.
vertically aligned carbonate clast
faint laminations (Tb)
crude laminations (Tb?)
220
230
240
250
260
270
280
290
300
310
320
330
⑥
1, Section 2

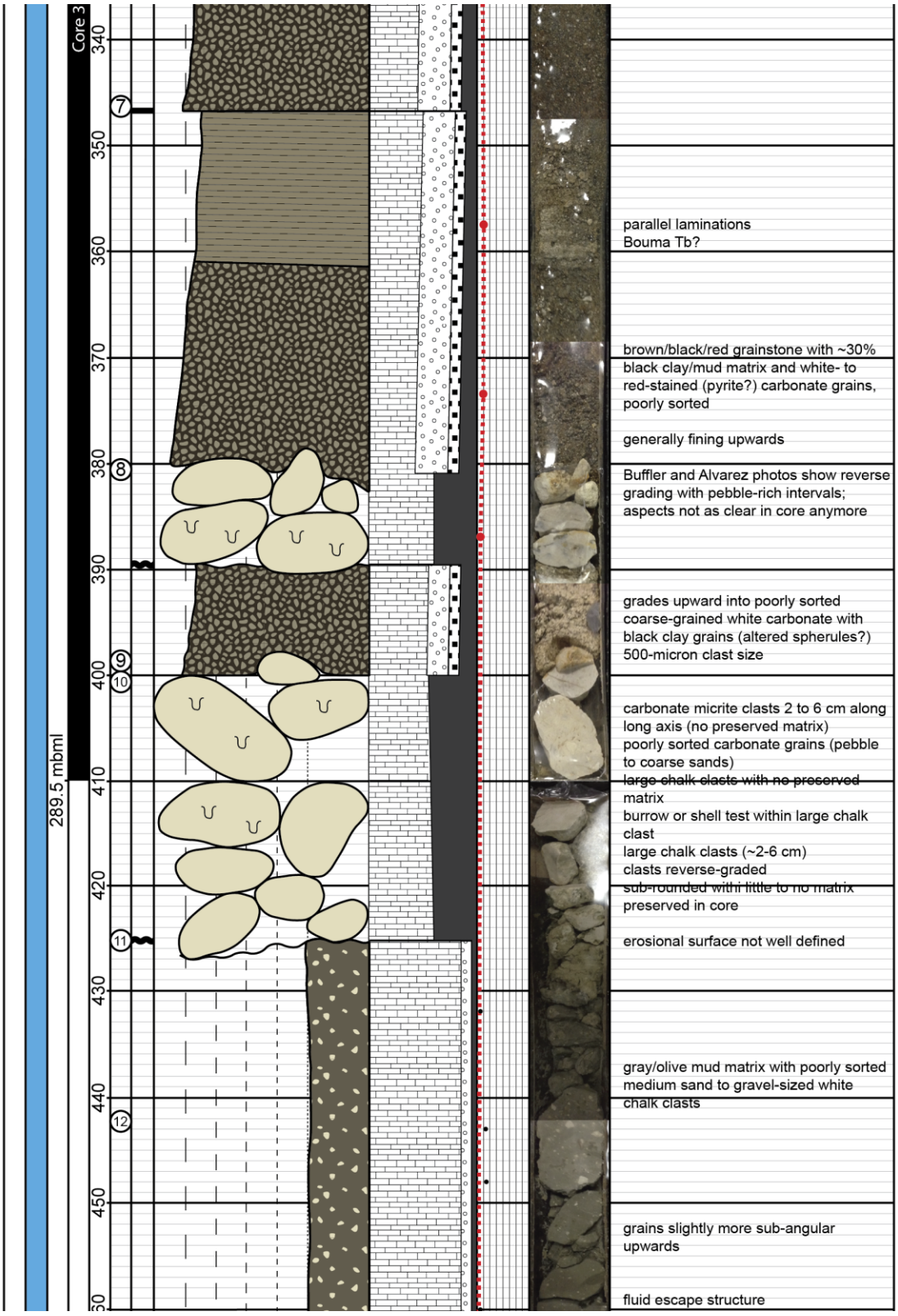
Core 3
289.5 mbml
340
350
360
370
380
390
400
410
420
430
440
450
7
8
9
10
11
12
parallel laminations
Bouma Tb?
brown/black/red grainstone with ~30% black clay/mud matrix and white- to red-stained (pyrite?) carbonate grains, poorly sorted
generally fining upwards
Buffler and Alvarez photos show reverse grading with pebble-rich intervals; aspects not as clear in core anymore
grades upward into poorly sorted coarse-grained white carbonate with black clay grains (altered spherules?)
500-micron clast size
carbonate micrite clasts 2 to 6 cm along long axis (no preserved matrix)
poorly sorted carbonate grains (pebble to coarse sands)
large chalk clasts with no preserved matrix
burrow or shell test within large chalk clast
large chalk clasts (~2-6 cm)
clasts reverse-graded
sub-rounded with little to no matrix preserved in core
erosional surface not well defined
gray/olive mud matrix with poorly sorted medium sand to gravel-sized white chalk clasts
grains slightly more sub-angular upwards
fluid escape structure

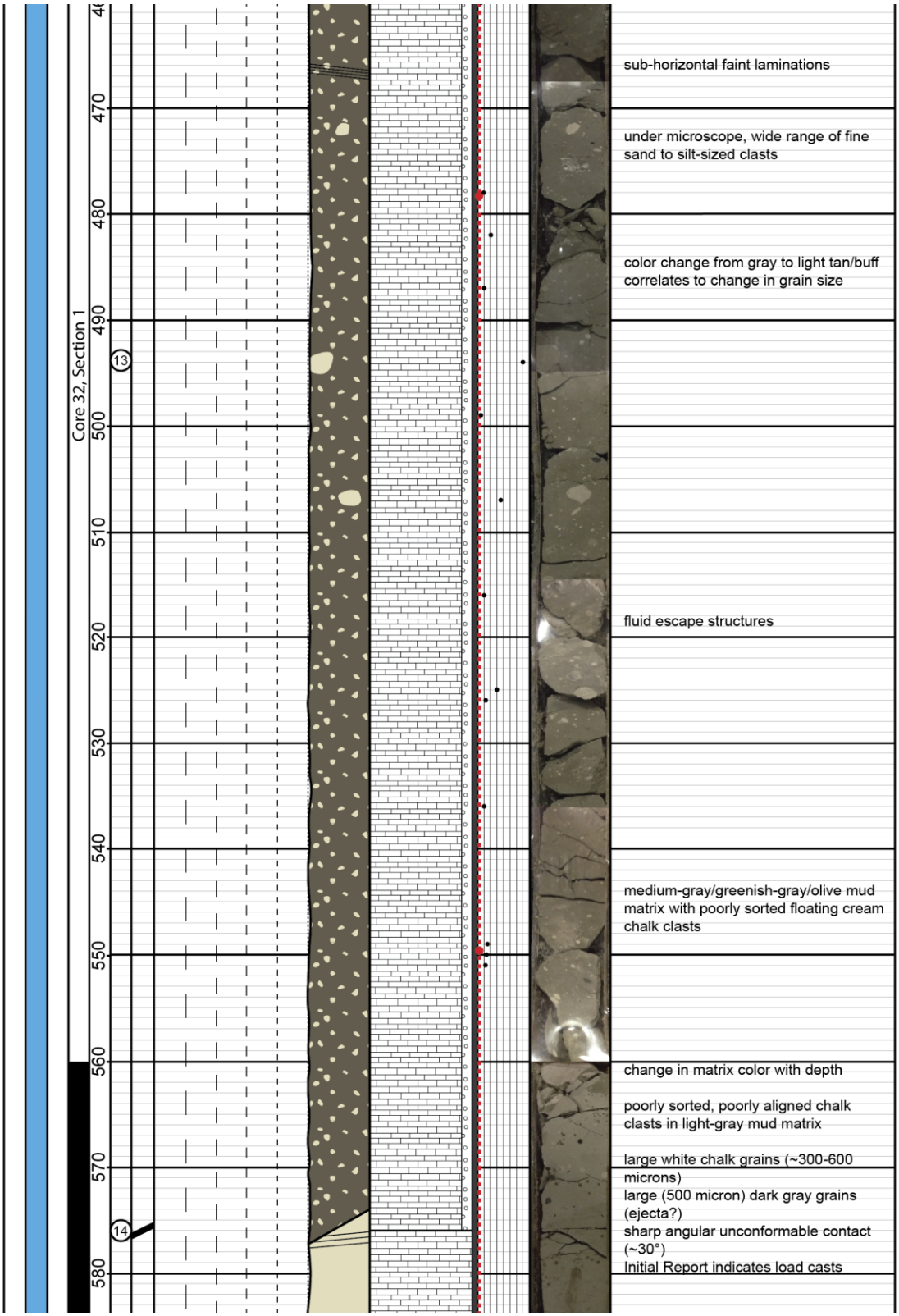
Core 32, Section 1
470
480
490
500
510
520
530
540
550
560
570
580
13
14
sub-horizontal faint laminations
under microscope, wide range of fine sand to silt-sized clasts
color change from gray to light tan/buff correlates to change in grain size
fluid escape structures
medium-gray/greenish-gray/olive mud matrix with poorly sorted floating cream chalk clasts
change in matrix color with depth
poorly sorted, poorly aligned chalk clasts in light-gray mud matrix
large white chalk grains (~300-600 microns)
large (500 micron) dark gray grains (ejecta?)
sharp angular unconformable contact (~30°)
Initial Report indicates load casts

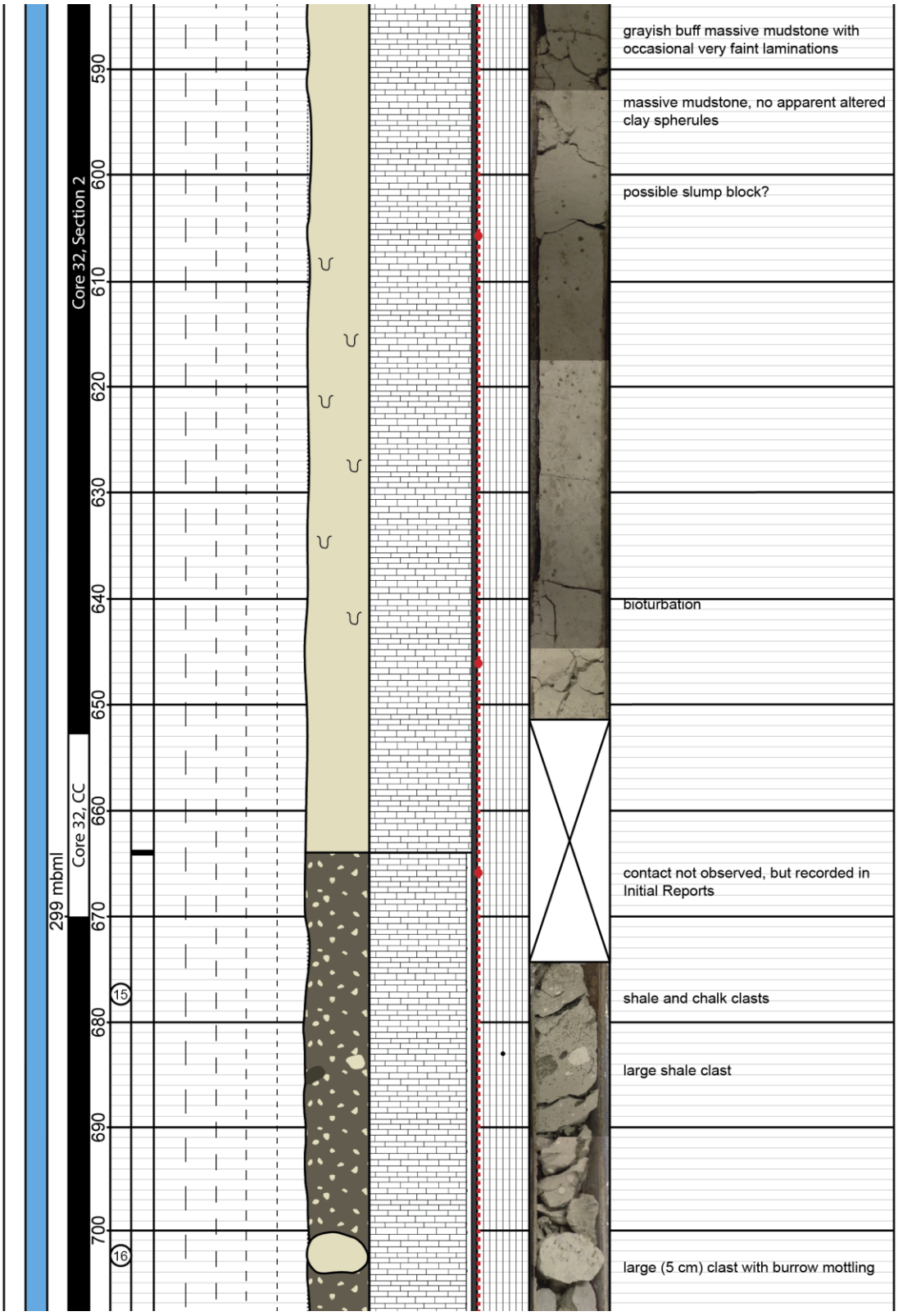
299 mbml
Core 32, Section 2
Core 32, CC
590
600
610
620
630
640
650
660
670
680
690
700
15
16
grayish buff massive mudstone with occasional very faint laminations
massive mudstone, no apparent altered clay spherules
possible slump block?
bioturbation
contact not observed, but recorded in Initial Reports
shale and chalk clasts
large shale clast
large (5 cm) clast with burrow mottling

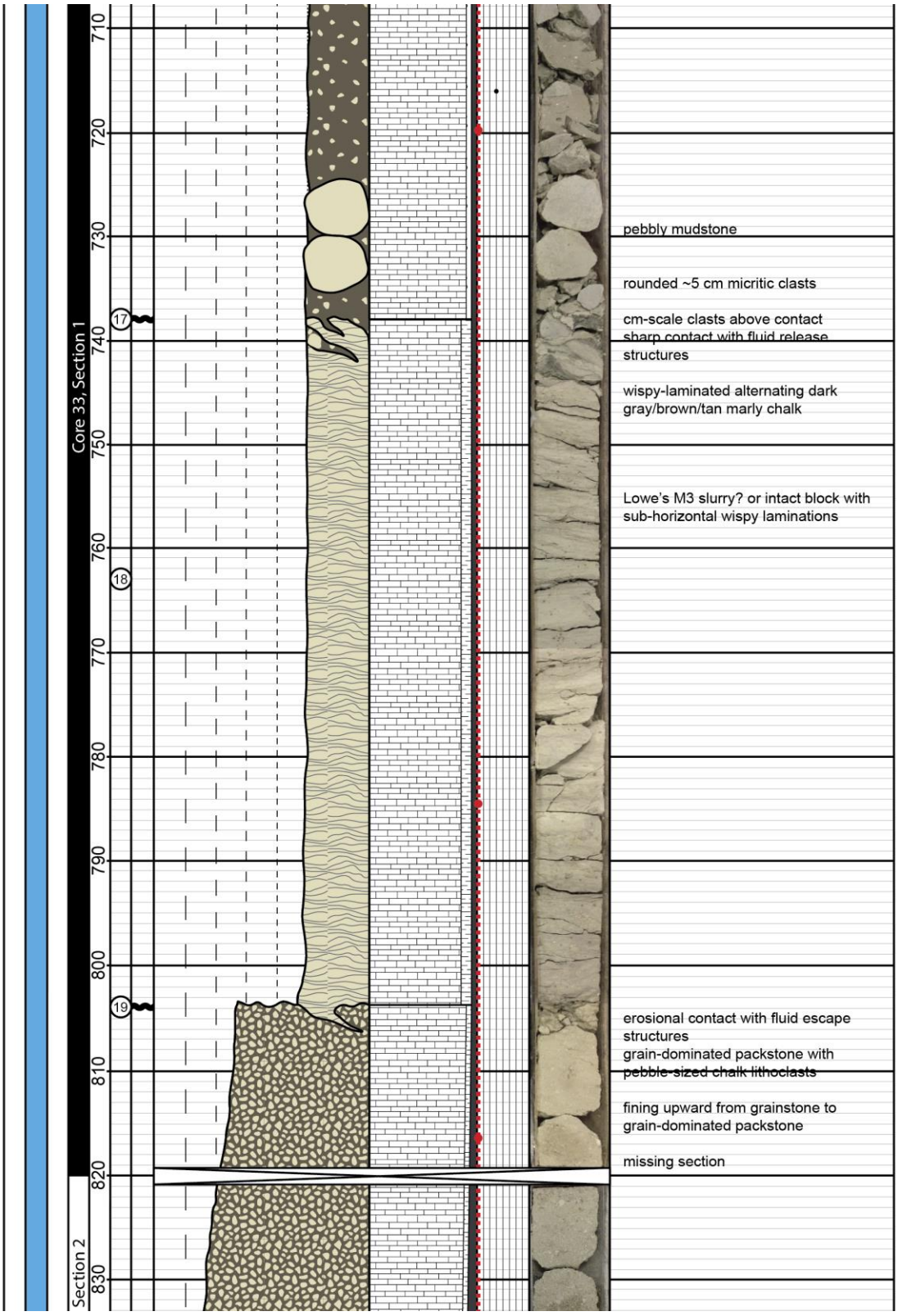
Core 33, Section 1
Section 2
710
720
730
740
750
760
770
780
790
800
810
820
830
17
18
19
pebbly mudstone
rounded ~5 cm micritic clasts
cm-scale clasts above contact
sharp contact with fluid release structures
wispy-laminated alternating dark gray/brown/tan marly chalk
Lowe's M3 slurry? or intact block with sub-horizontal wispy laminations
erosional contact with fluid escape structures
grain-dominated packstone with pebble-sized chalk lithoclasts
fining upward from grainstone to grain-dominated packstone
missing section

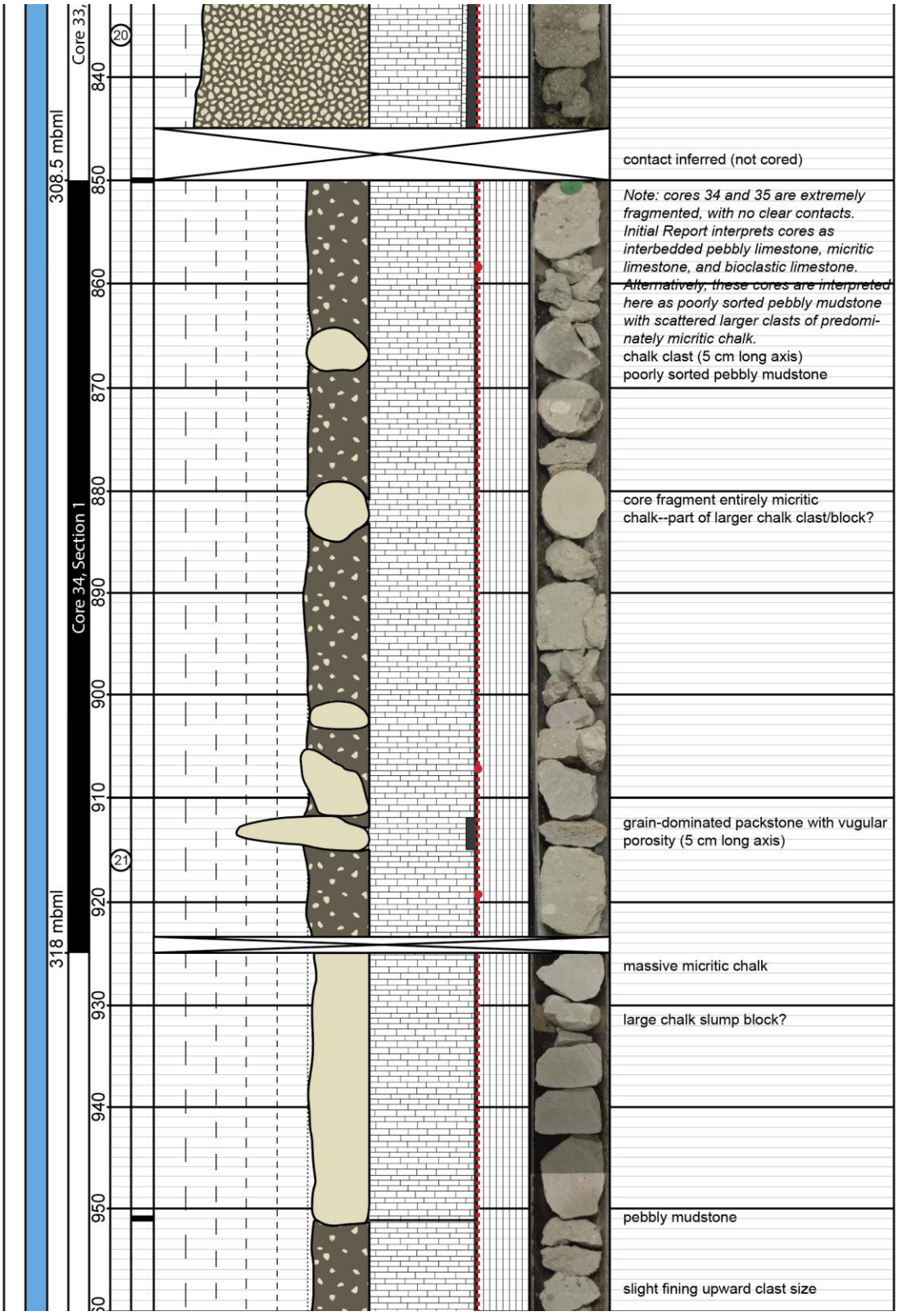
Core 33
308.5 mbml
Core 34, Section 1
318 mbml
20
21
840
850
860
870
880
890
900
910
920
930
940
950
contact inferred (not cored)
Note: cores 34 and 35 are extremely fragmented, with no clear contacts. Initial Report interprets cores as interbedded pebbly limestone, micritic limestone, and bioclastic limestone. Alternatively, these cores are interpreted here as poorly sorted pebbly mudstone with scattered larger clasts of predominately micritic chalk.
chalk clast (5 cm long axis)
poorly sorted pebbly mudstone
core fragment entirely micritic chalk--part of larger chalk clast/block?
grain-dominated packstone with vugular porosity (5 cm long axis)
massive micritic chalk
large chalk slump block?
pebbly mudstone
slight fining upward clast size

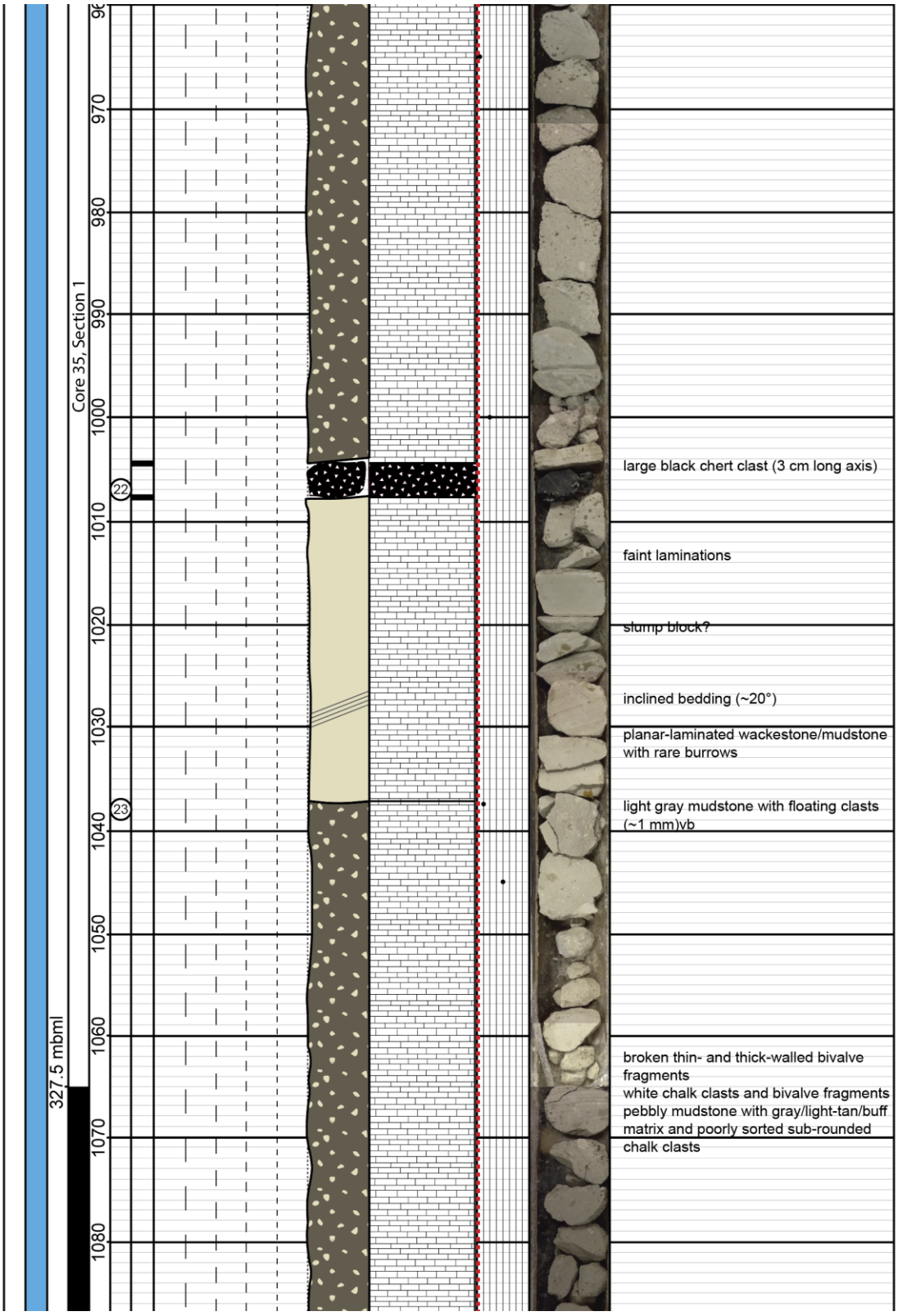
Core 35, Section 1
327.5 mbml
970
980
990
1000
1010
1020
1030
1040
1050
1060
1070
1080
22
23
large black chert clast (3 cm long axis)
faint laminations
slump block?
inclined bedding (~20°)
planar-laminated wackestone/mudstone with rare burrows
light gray mudstone with floating clasts (~1 mm)yb
broken thin- and thick-walled bivalve fragments
white chalk clasts and bivalve fragments
pebbly mudstone with gray/light-tan/buff matrix and poorly sorted sub-rounded chalk clasts

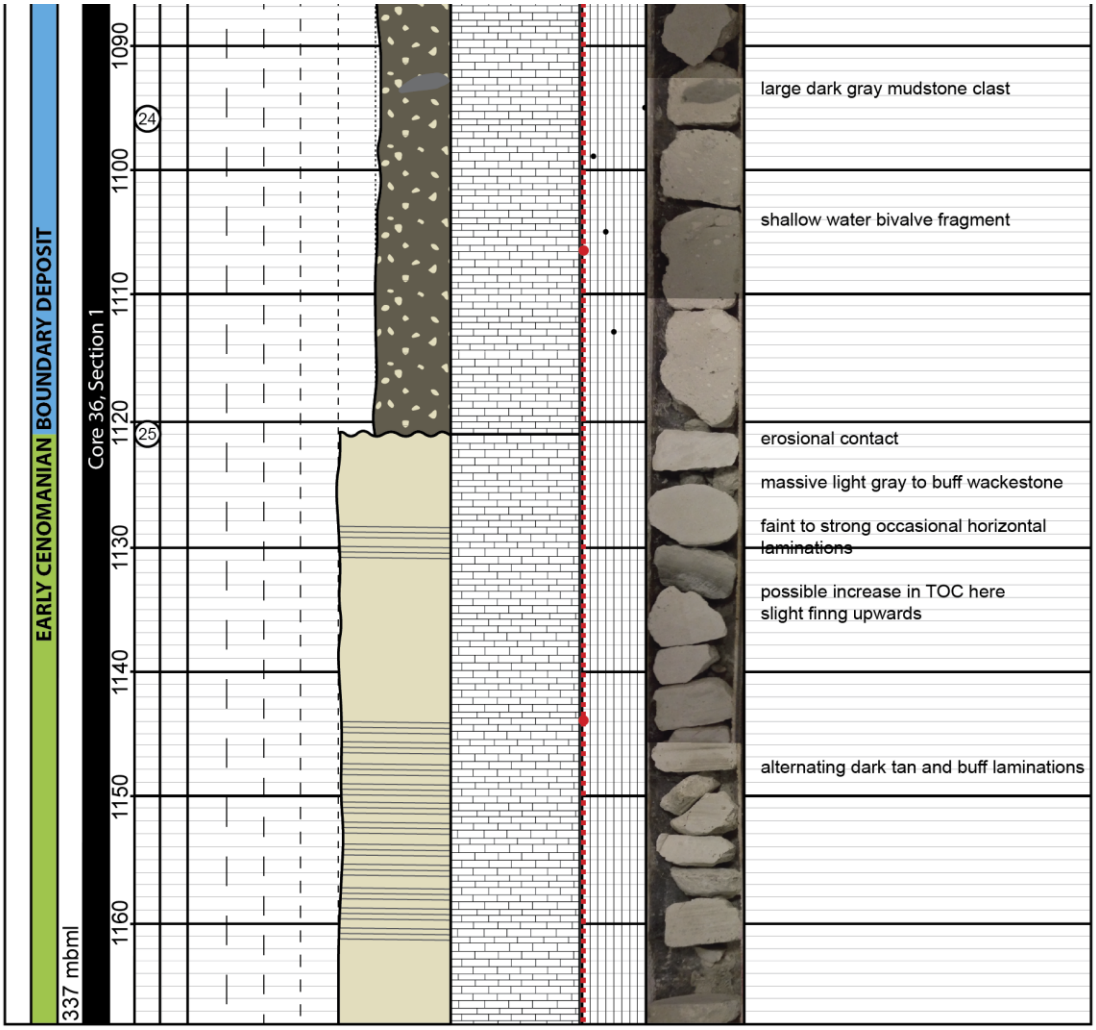
EARLY CENOMANIAN BOUNDARY DEPOSIT
337 mbml
Core 36, Section 1
1090
1100
1110
1120
1130
1140
1150
1160
24
25
large dark gray mudstone clast
shallow water bivalve fragment
erosional contact
massive light gray to buff wackestone
faint to strong occasional horizontal laminations
possible increase in TOC here
slight finng upwards
alternating dark tan and buff laminations

APPENDIX 3: TRUE STRATIGRAPHIC POSITION TRANSFORMATION FOR FIELD MEASUREMENTS OF THE PANOCHE GIANT INJECTION COMPLEX

For analysis of stratigraphic trends in the PGIC, True Stratigraphic Thickness (TST) between points of measurement and the top of the Panoche Formation was calculated in order to plot points by True Stratigraphic Position (TSP; Figure A1 and Table A6). Prior to transformation, Digital Elevation Model (DEM)–derived elevation data was attached to UTM coordinates of data. Given a point along a datum (e.g., the top of the Panoche Formation) and a point of measurement, the horizontal distance between the two is:

$$D_{traverse} = \sqrt{(x_{measurement} - x_{datum})^2 + (y_{measurement} - y_{datum})^2} \quad (5)$$

Where ($x_{measurement}$, $y_{measurement}$) and (x_{datum}, y_{datum}) are the horizontal Cartesian coordinates of the measurement and datum points, respectively. The bearing of the traverse from the datum point to the measurement point, $\Phi_{traverse}$, is:

$$\phi_{traverse} = 90° - \tan\left(\frac{x_{measurement} - x_{datum}}{y_{measurement} - y_{datum}}\right) \quad (6)$$

Given a bedding orientation of strike, $\Phi_{bedding}$, and dip bearing, Φ_{dip}, the absolute value of the difference between the traverse bearing and the dip bearing, θ_{TSP}, is:

$$\theta_{TSP} = |\phi_{traverse} - \phi_{dip}| \quad (7)$$

And the horizontal distance normal to the strike of bedding, Y_{TSP}, is:

$$Y_{TSP} = D_{traverse} \times \cos\theta_{TSP} \quad (8)$$

The horizontal Cartesian coordinates of the resulting point (i.e., measurement point rectified along-strike to dip-normal) are (x_{TSP}, y_{TSP}), where:

$$x_{TSP} = Y_{TSP} \times \sin\phi_{dip} \quad (9)$$

$$y_{TSP} = Y_{TSP} \times \cos \phi_{dip} \tag{10}$$

The measurement point is now transformed such that it and the datum point can be viewed in a true-dip–section (Figure A1B). The apparent thickness of the stratigraphic section, $T_{apparent}$, is:

$$T_{apparent} = \sqrt{Y_{TSP}^2 + Z_{TSP}^2} \tag{11}$$

Where Z_{TSP} is the vertical distance between the transformed measurement point and the datum point. The slope of the apparent thickness, $\alpha_{apparent}$, and the sum of the slope of the apparent thickness and the dip of bedding, $\theta_{apparent}$, are:

$$\alpha_{apparent} = \arctan\left(\frac{Z_{TSP}}{Y_{TSP}}\right) \tag{12}$$

$$\theta_{apparent} = \alpha_{apparent} + \text{dip} \tag{13}$$

The true stratigraphic thickness, TST, is then:

$$TST = T_{apparent} \times \sin \theta_{apparent} \tag{14}$$

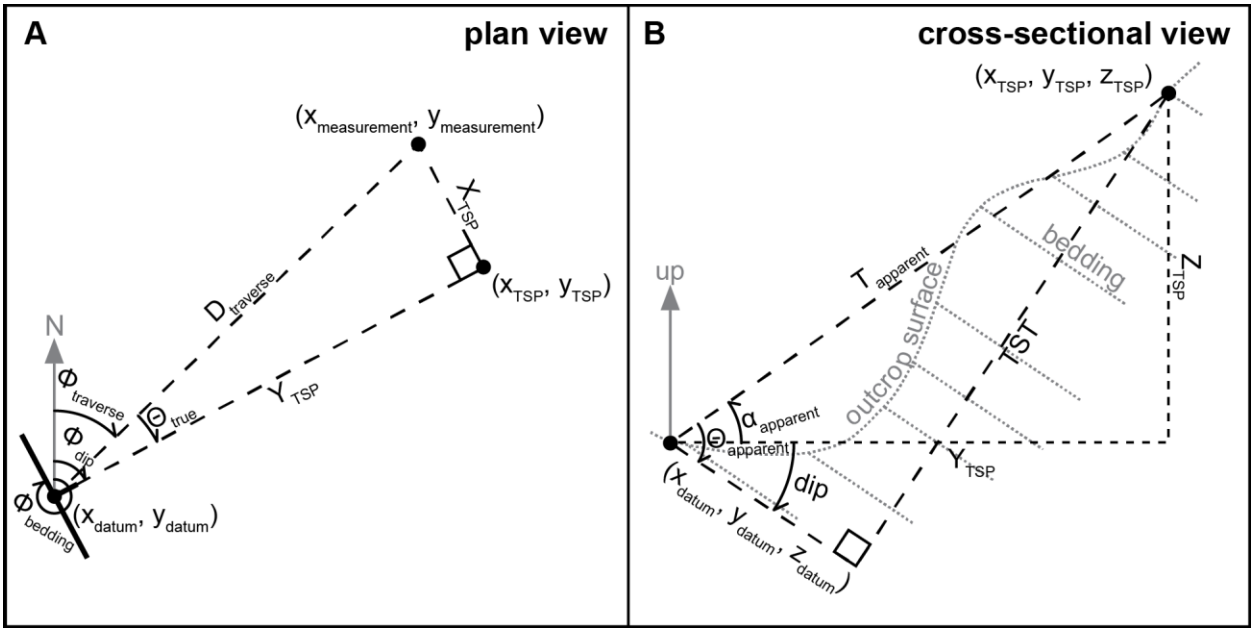

Figure 31: Diagram illustrating terminology and trigonometry of transform from Cartesian coordinates to True Stratigraphic Position.

Locale	Feature	Longitude °	Latitude °	Easting m	Northing m	Elevation m	TSP m	Strike °	Dip °	Paleo-strike °	Paleo-dip °	Aperture m
MG	bedding	-120.74348	36.72749	701505	4067016	506	-46	323	33	237	3	
MG	bedding	-120.73853	36.72955	701942	4067256	327	72	326	45	319	12	
MG	bedding	-120.73844	36.73049	701947	4067360	301	86	327	40	319	7	
MG	bedding	-120.73838	36.73048	701953	4067359	302	89	322	24	166	10	
MG	bedding	-120.73843	36.73057	701948	4067368	308	96	326	32	206	2	
MG	bedding	-120.73909	36.73115	701888	4067432	329	108	332	38	349	5	
MG	bedding	-120.73705	36.73021	702073	4067332	311	140	337	29	107	6	
MG	bedding	-120.73459	36.72786	702298	4067076	322	164	330	34	358	1	
MG	bedding	-120.73699	36.73108	702075	4067428	301	165	337	22	134	12	
MG	bedding	-120.73728	36.73147	702049	4067471	365	221	327	40	319	7	
MG	bedding	-120.73564	36.73177	702194	4067508	289	233	332	48	338	15	
MG	bedding	-120.73275	36.73114	702454	4067443	256	297	318	42	288	11	
MG	bedding	-120.73278	36.73189	702449	4067526	302	360	336	39	6	7	
MG	bedding	-120.73259	36.73266	702465	4067613	325	414	343	16	136	18	
MG	bedding	-120.72879	36.73173	702807	4067517	266	483	340	51	356	19	
MG	injectite	-120.74134	36.72853	701694	4067136	426	7	52	14	124	34	11.89
MG	injectite	-120.74136	36.72853	701692	4067136	428	9	160	56	158	89	0.36
MG	injectite	-120.74110	36.72872	701715	4067158	415	15	46	20	112	34	15.54
MG	injectite	-120.74064	36.72886	701756	4067174	397	22	327	46	323	13	1.83
MG	injectite	-120.74036	36.72902	701780	4067193	384	29	339	61	347	29	0.30
MG	injectite	-120.74036	36.72902	701780	4067193	384	29	326	39	311	6	2.44
MG	injectite	-120.73681	36.72657	702104	4066928	326	34	344	32	72	8	6.00
MG	injectite	-120.74351	36.72751	701503	4067018	503	50	327	37	312	4	
MG	injectite	-120.73882	36.72962	701916	4067262	311	50	290	15	174	23	
MG	injectite	-120.73957	36.72956	701850	4067254	368	65	313	45	283	16	5.00
MG	injectite	-120.73872	36.73049	701923	4067359	295	71	323	36	278	5	
MG	injectite	-120.73930	36.72963	701874	4067263	360	72	321	43	300	11	2.44
MG	injectite	-120.73861	36.73048	701933	4067359	294	74	325	30	182	4	

MG	injectite	-120.73811	36.73013	701978	4067320	302	88	220	43	197	61	
MG	injectite	-120.73804	36.73010	701985	4067317	307	94	321	33	236	4	1.83
MG	injectite	-120.73810	36.73018	701979	4067327	308	95	331	35	359	2	3.66
MG	injectite	-120.73870	36.73048	701924	4067358	327	98	343	31	80	8	3.00
MG	injectite	-120.73809	36.73020	701979	4067328	313	100	333	28	129	5	1.50
MG	injectite	-120.73865	36.73050	701929	4067360	327	101	325	40	309	7	2.00
MG	injectite	-120.73799	36.73014	701989	4067322	311	101	314	33	233	8	1.04
MG	injectite	-120.73545	36.72751	702223	4067036	306	104	321	36	269	5	4.00
MG	injectite	-120.73800	36.73017	701988	4067326	314	104	307	22	182	15	0.33
MG	injectite	-120.73798	36.73015	701989	4067323	316	105	309	31	220	11	1.50
MG	injectite	-120.74127	36.73231	701690	4067556	381	106	329	38	329	5	
MG	injectite	-120.73800	36.73014	701988	4067322	319	107	228	36	196	52	0.50
MG	injectite	-120.73794	36.73019	701994	4067328	316	109	317	38	270	9	3.96
MG	injectite	-120.73562	36.72772	702207	4067058	313	111	324	40	304	8	2.50
MG	injectite	-120.73802	36.73024	701986	4067333	320	111	220	43	197	61	19.96
MG	injectite	-120.73786	36.73018	702000	4067326	319	113	266	36	217	35	1.02
MG	injectite	-120.73889	36.73083	701907	4067396	345	118					0.61
MG	injectite	-120.73782	36.73019	702004	4067327	322	118	328	28	154	5	1.50
MG	injectite	-120.73510	36.72755	702254	4067041	306	119	233	83	230	87	0.91
MG	injectite	-120.73773	36.73012	702012	4067320	323	120					0.05
MG	injectite	-120.73797	36.73029	701990	4067339	328	121					0.08
MG	injectite	-120.73773	36.73012	702012	4067320	323	121	246	80	239	78	0.53
MG	injectite	-120.73532	36.72767	702234	4067053	313	121	331	38	343	5	1.22
MG	injectite	-120.73780	36.73019	702006	4067328	324	121					0.13
MG	injectite	-120.73789	36.73025	701998	4067334	326	121	53	85	57	83	0.28
MG	injectite	-120.73780	36.73020	702005	4067329	325	122	237	72	227	76	0.15
MG	injectite	-120.73822	36.73047	701967	4067358	334	122					0.10
MG	injectite	-120.73844	36.73056	701947	4067368	340	122	331	43	337	10	0.99
MG	injectite	-120.73829	36.73050	701961	4067361	337	124	346	82	351	51	0.13
MG	injectite	-120.73904	36.73098	701893	4067413	353	124	47	90	49	84	0.08
MG	injectite	-120.73837	36.73054	701954	4067365	340	124					0.08

MG	injectite	-120.73812	36.73042	701977	4067352	334	125					0.08
MG	injectite	-120.73819	36.73046	701970	4067357	336	125					0.15
MG	injectite	-120.73919	36.73109	701880	4067425	358	127	11	90	16	66	4.42
MG	injectite	-120.73782	36.73039	702004	4067350	332	133	215	35	188	56	31.09
MG	injectite	-120.73686	36.73002	702090	4067311	303	134	325	42	312	9	1.09
MG	injectite	-120.73714	36.73021	702064	4067332	313	138	251	76	241	72	
MG	injectite	-120.73720	36.73088	702057	4067406	289	139	329	31	149	2	
MG	injectite	-120.73573	36.72815	702196	4067106	334	139	254	82	247	75	0.30
MG	injectite	-120.73685	36.73005	702091	4067314	307	139	325	32	212	2	
MG	injectite	-120.73665	36.73053	702108	4067368	280	142	55	80	61	80	
MG	injectite	-120.73577	36.72822	702192	4067114	338	143	321	44	301	12	0.46
MG	injectite	-120.73774	36.73128	702009	4067449	305	146	345	58	360	27	
MG	injectite	-120.73568	36.72826	702200	4067118	337	147	83	67	91	83	0.46
MG	injectite	-120.73661	36.73033	702112	4067346	306	157	247	78	239	76	2.67
MG	injectite	-120.73660	36.73043	702112	4067357	303	159	318	30	207	7	1.50
MG	injectite	-120.73665	36.73042	702107	4067355	307	159					0.25
MG	injectite	-120.73667	36.73043	702106	4067357	307	160					0.61
MG	injectite	-120.73666	36.73042	702107	4067356	307	160	52	90	53	86	0.25
MG	injectite	-120.73663	36.73039	702110	4067353	307	160	302	47	267	22	0.48
MG	injectite	-120.73659	36.73046	702113	4067360	304	161	241	82	236	82	0.30
MG	injectite	-120.73460	36.72783	702298	4067073	324	164	246	79	239	77	0.91
MG	injectite	-120.73739	36.73099	702041	4067417	323	164					0.25
MG	injectite	-120.73697	36.73077	702079	4067394	313	164	230	80	226	87	0.13
MG	injectite	-120.73690	36.73070	702085	4067386	313	165					0.13
MG	injectite	-120.73694	36.73076	702081	4067393	313	165					0.13
MG	injectite	-120.73691	36.73071	702084	4067388	314	166	97	80	277	79	0.20
MG	injectite	-120.73749	36.73107	702031	4067426	327	166	96	71	280	88	0.58
MG	injectite	-120.73315	36.72706	702429	4066990	291	166	53	85	57	83	4.00
MG	injectite	-120.73750	36.73109	702030	4067428	327	167					0.20
MG	injectite	-120.73647	36.73040	702124	4067354	308	167	229	81	226	88	2.00
MG	injectite	-120.73679	36.73097	702094	4067416	299	167	275	34	218	29	

MG	injectite	-120.73751	36.73110	702029	4067430	328	168					0.30
MG	injectite	-120.73795	36.73149	701989	4067472	346	179	197	48	184	73	0.30
MG	injectite	-120.73786	36.73142	701997	4067464	345	180					0.53
MG	injectite	-120.73792	36.73147	701991	4067470	348	181	11	68	28	46	0.15
MG	injectite	-120.73796	36.73151	701988	4067474	349	182	350	47	22	19	0.81
MG	injectite	-120.73796	36.73153	701988	4067476	349	182	246	74	236	73	0.23
MG	injectite	-120.73335	36.72738	702410	4067026	306	182	230	76	224	83	2.00
MG	injectite	-120.73805	36.73158	701980	4067482	351	183	86	67	94	84	0.15
MG	injectite	-120.73329	36.72738	702416	4067026	306	185	301	79	293	51	2.00
MG	injectite	-120.73618	36.73043	702149	4067358	314	185	250	80	243	76	1.50
MG	injectite	-120.73822	36.73176	701964	4067501	367	196	2	24	103	18	10.01
MG	injectite	-120.73550	36.73118	702208	4067442	264	196	321	44	301	12	
MG	injectite	-120.73575	36.73067	702188	4067385	300	199	228	72	220	81	1.50
MG	injectite	-120.73275	36.72718	702465	4067004	307	200	60	90	240	90	0.50
MG	injectite	-120.73825	36.73184	701961	4067510	372	201	354	13	134	22	4.06
MG	injectite	-120.73233	36.72727	702502	4067015	295	210	282	52	250	36	2.00
MG	injectite	-120.73540	36.73071	702218	4067391	296	211	252	83	246	77	1.63
MG	injectite	-120.73543	36.73068	702216	4067387	299	211	63	90	242	88	3.00
MG	injectite	-120.73710	36.73140	702065	4067463	360	221					2.01
MG	injectite	-120.73534	36.73109	702223	4067432	292	223	328	27	153	6	7.26
MG	injectite	-120.73455	36.73099	702294	4067424	268	231	82	81	263	86	
MG	injectite	-120.73452	36.73100	702297	4067424	270	233	276	75	263	58	
MG	injectite	-120.73454	36.73112	702295	4067437	272	239	254	82	247	75	
MG	injectite	-120.73433	36.73069	702315	4067391	289	246	295	54	267	31	0.36
MG	injectite	-120.73429	36.73074	702318	4067396	289	250	252	55	228	55	0.64
MG	injectite	-120.73412	36.73076	702332	4067399	283	252	243	49	216	55	1.68
MG	injectite	-120.73453	36.73099	702296	4067424	302	260	77	80	260	89	2.74
MG	injectite	-120.73393	36.73089	702350	4067414	284	265	226	73	219	83	
MG	injectite	-120.73452	36.73111	702296	4067436	304	266	254	83	248	76	1.07
MG	injectite	-120.73458	36.73119	702291	4067445	309	270	227	71	219	80	2.44
MG	injectite	-120.73403	36.73114	702340	4067441	296	280	71	90	249	84	1.00

MG	injectite	-120.73382	36.73112	702359	4067439	290	283	70	90	248	84	4.00
MG	injectite	-120.73427	36.73130	702318	4067459	305	284	237	75	229	79	5.00
MG	injectite	-120.73309	36.73093	702424	4067420	278	295	93	64	101	85	0.33
MG	injectite	-120.73324	36.73124	702410	4067453	283	303	241	90	241	89	3.40
MG	injectite	-120.73303	36.73105	702429	4067433	282	304					0.13
MG	injectite	-120.73266	36.73144	702462	4067477	255	310	251	80	244	75	
MG	injectite	-120.73355	36.73149	702382	4067481	296	311	208	73	24	89	
MG	injectite	-120.73358	36.73153	702379	4067485	297	312	215	88	38	79	3.35
MG	injectite	-120.73332	36.73159	702402	4067493	300	327	224	77	220	87	3.00
MG	injectite	-120.73248	36.73106	702479	4067436	284	329	132	61	314	87	4.88
MG	injectite	-120.73256	36.73192	702469	4067531	271	345	64	90	243	87	
MG	injectite	-120.73258	36.73149	702469	4067483	291	345	257	85	252	76	3.12
MG	injectite	-120.73258	36.73196	702467	4067535	273	346	232	68	221	75	
MG	injectite	-120.73259	36.73158	702467	4067493	290	347	237	82	233	84	0.30
MG	injectite	-120.73279	36.73181	702449	4067518	297	353	252	85	247	79	0.61
MG	injectite	-120.73285	36.73185	702443	4067522	300	355	147	42	148	75	1.47
MG	injectite	-120.73286	36.73189	702442	4067526	299	355	147	51	147	84	
MG	injectite	-120.73282	36.73185	702446	4067522	301	357	231	79	226	85	2.79
MG	injectite	-120.73284	36.73191	702444	4067529	304	361	158	55	156	88	1.02
MG	injectite	-120.73347	36.73237	702387	4067578	334	377	5	35	69	20	5.18
MG	injectite	-120.73152	36.73169	702563	4067508	272	379	55	82	60	81	0.18
MG	injectite	-120.73188	36.73198	702530	4067539	283	384	243	60	225	63	0.66
MG	injectite	-120.73151	36.73172	702563	4067511	279	385	258	81	250	72	3.00
MG	injectite	-120.73152	36.73173	702563	4067512	280	386	265	86	259	73	2.44
MG	injectite	-120.73187	36.73202	702530	4067543	290	391	240	80	234	81	0.38
MG	injectite	-120.73197	36.73213	702521	4067555	295	395	39	85	45	75	1.52
MG	injectite	-120.73186	36.73209	702532	4067551	292	396	206	84	28	78	0.10
MG	injectite	-120.73163	36.73197	702552	4067538	286	396	238	75	230	78	
MG	injectite	-120.73164	36.73199	702551	4067541	287	397					0.11
MG	injectite	-120.73207	36.73219	702512	4067562	300	398	232	65	219	73	0.51
MG	injectite	-120.73221	36.73230	702500	4067574	307	402	182	83	4	69	0.18

MG	injectite	-120.73159	36.73197	702556	4067538	292	402	244	78	237	77	2.00
MG	injectite	-120.73027	36.73178	702674	4067520	267	426	114	87	290	66	
MG	injectite	-120.73049	36.73193	702654	4067536	281	435					0.23
MG	injectite	-120.73082	36.73229	702624	4067575	298	449					1.14
MC	bedding	-120.72806	36.70441	702943	4064489	469	-28	338	47	269	2	
MC	bedding	-120.73049	36.70968	702713	4065067	460	-27	337	30	315	5	
MC	bedding	-120.72787	36.70432	702960	4064479	462	-27	331	31	122	2	
MC	bedding	-120.72781	36.70431	702966	4064477	459	-27	337	38	103	2	
MC	bedding	-120.72692	36.70932	703032	4065036	340	52	344	35	136	6	
MC	bedding	-120.72746	36.71188	702978	4065319	357	102	344	34	19	3	
MC	bedding	-120.72575	36.70935	703137	4065041	332	107	340	32	8	4	
MC	bedding	-120.72785	36.71235	702941	4065370	382	114	331	32	3	8	
MC	bedding	-120.72676	36.71152	703041	4065280	339	115	342	28	98	5	
MC	bedding	-120.72620	36.71110	703092	4065234	333	128	341	34	15	7	
MC	bedding	-120.72294	36.70924	703388	4065035	305	226	333	36	352	15	
MC	bedding	-120.72228	36.70852	703449	4064957	295	234	337	47	355	15	
MC	bedding	-120.72266	36.70896	703414	4065004	307	234	333	35	73	6	
MC	bedding	-120.72180	36.70794	703493	4064893	295	243	336	40	56	7	
MC	bedding	-120.72169	36.70842	703502	4064947	307	271	326	34	102	8	
MC	bedding	-120.71941	36.70635	703711	4064722	302	331	347	34	58	8	
MC	bedding	-120.71903	36.70724	703743	4064821	284	359	306	36	52	9	
MC	bedding	-120.71846	36.70690	703795	4064785	276	373	327	38	61	10	
MC	bedding	-120.71947	36.70805	703701	4064910	380	432	332	27	95	14	
MC	injectite	-120.73052	36.70968	702710	4065067	460	-29	354	27	242	13	0.30
MC	injectite	-120.72701	36.70921	703025	4065023	345	49	228	33	194	50	2.50
MC	injectite	-120.72881	36.71271	702854	4065407	385	76	1	26	96	17	4.00
MC	injectite	-120.72830	36.71236	702901	4065370	367	79	326	30	175	3	4.00
MC	injectite	-120.72674	36.70966	703047	4065073	357	83	318	39	277	9	0.69
MC	injectite	-120.72849	36.71260	702884	4065396	387	91	359	52	28	27	4.00
MC	injectite	-120.72762	36.71192	702963	4065322	355	93	32	70	47	59	1.30
MC	injectite	-120.72737	36.71178	702985	4065307	346	95	327	32	195	2	2.00

MC	injectite	-120.72731	36.71173	702991	4065301	347	98	247	89	245	85	0.76
MC	injectite	-120.72620	36.70949	703097	4065056	346	98	327	42	321	9	0.51
MC	injectite	-120.72879	36.71302	702856	4065442	402	99	336	35	35	4	0.91
MC	injectite	-120.72578	36.70933	703134	4065038	327	100	227	34	194	51	3.00
MC	injectite	-120.72755	36.71194	702969	4065325	361	102	336	30	101	5	10.00
MC	injectite	-120.72848	36.71275	702884	4065413	397	104	336	44	353	12	10.00
MC	injectite	-120.72882	36.71307	702853	4065447	409	104	335	33	62	3	0.56
MC	injectite	-120.72888	36.71311	702847	4065452	415	106	333	36	8	4	0.41
MC	injectite	-120.72885	36.71311	702850	4065452	413	106	331	31	122	2	0.15
MC	injectite	-120.72579	36.70942	703133	4065048	335	108	168	90	351	59	1.50
MC	injectite	-120.72770	36.71221	702955	4065354	374	111	328	33	239	1	14.00
MC	injectite	-120.72834	36.71279	702897	4065417	397	112	328	34	300	1	0.76
MC	injectite	-120.72758	36.71214	702966	4065346	370	113	339	38	22	8	0.25
MC	injectite	-120.72722	36.71181	702999	4065311	359	114	327	41	320	8	20.00
MC	injectite	-120.72731	36.71190	702991	4065321	362	115	318	44	293	13	20.00
MC	injectite	-120.72685	36.71159	703033	4065288	344	116	262	25	197	32	1.52
MC	injectite	-120.72827	36.71279	702903	4065418	399	117	242	71	231	73	1.32
MC	injectite	-120.72755	36.71213	702969	4065346	375	118	312	36	249	10	0.28
MC	injectite	-120.72814	36.71272	702915	4065410	394	118	234	82	231	86	0.28
MC	injectite	-120.72753	36.71213	702970	4065346	374	119	51	85	55	82	0.43
MC	injectite	-120.72797	36.71256	702930	4065393	390	119	9	56	36	35	18.00
MC	injectite	-120.72788	36.71249	702938	4065385	390	122	235	75	227	80	0.23
MC	injectite	-120.72687	36.71171	703031	4065301	350	123	343	25	115	10	0.30
MC	injectite	-120.72623	36.71113	703089	4065238	328	124	343	56	358	25	0.28
MC	injectite	-120.72681	36.71172	703036	4065302	356	130	67	90	246	86	0.30
MC	injectite	-120.72584	36.71137	703124	4065265	336	156	101	90	276	69	0.30
MC	injectite	-120.72511	36.71072	703190	4065195	322	165	232	68	221	75	1.17
MC	injectite	-120.72484	36.71079	703215	4065202	329	187	261	90	258	78	1.78
MC	injectite	-120.72400	36.70997	703291	4065114	313	196	24	63	45	49	0.91
MC	injectite	-120.72465	36.71091	703231	4065217	331	201	252	60	232	58	4.00
MC	injectite	-120.72495	36.71141	703203	4065271	340	205	64	82	68	86	1.24

MC	injectite	-120.72459	36.71091	703236	4065217	333	205	237	82	233	84	2.13
MC	injectite	-120.72477	36.71110	703220	4065237	341	207	239	81	234	83	1.52
MC	injectite	-120.72458	36.71094	703237	4065220	336	209	234	70	224	76	0.66
MC	injectite	-120.72431	36.71102	703261	4065229	326	217	239	75	231	78	2.44
MC	injectite	-120.72452	36.71126	703242	4065255	336	220	71	88	250	85	3.15
MC	injectite	-120.72426	36.71097	703265	4065224	332	223	60	83	64	85	0.13
MC	injectite	-120.72433	36.71102	703259	4065230	338	225	253	88	250	81	2.36
MC	injectite	-120.72427	36.71106	703264	4065234	336	228	246	70	234	70	3.00
MC	injectite	-120.72434	36.71132	703258	4065262	334	229	221	42	197	59	2.00
MC	injectite	-120.72352	36.71002	703334	4065120	327	233	72	79	76	88	0.61
MC	injectite	-120.72451	36.71164	703242	4065297	340	234	328	39	323	6	0.30
MC	injectite	-120.72412	36.71110	703277	4065239	333	234	66	85	68	90	3.25
MC	injectite	-120.72426	36.71154	703264	4065287	328	234	326	43	317	10	2.44
MC	injectite	-120.72355	36.71049	703330	4065172	321	239	339	29	101	7	0.69
MC	injectite	-120.72423	36.71157	703267	4065290	332	240	321	45	303	13	1.22
MC	injectite	-120.72416	36.71139	703274	4065270	335	241	68	86	249	89	1.24
MC	injectite	-120.72196	36.70824	703479	4064926	296	244	203	66	197	87	0.91
MC	injectite	-120.72395	36.71107	703293	4065236	342	250	64	84	67	88	0.23
MC	injectite	-120.72396	36.71111	703292	4065240	342	250	68	85	249	89	1.47
MC	injectite	-120.72223	36.70902	703452	4065012	306	257	272	68	255	54	0.51
MC	injectite	-120.72191	36.70858	703481	4064964	303	260	212	63	203	81	1.32
MC	injectite	-120.72173	36.70839	703499	4064943	298	261	340	68	347	36	2.74
MC	injectite	-120.72194	36.70859	703479	4064965	307	262	237	82	233	84	2.08
MC	injectite	-120.72221	36.70895	703454	4065005	315	264	97	87	274	73	0.81
MC	injectite	-120.72165	36.70816	703507	4064918	306	265	73	90	251	82	1.52
MC	injectite	-120.72378	36.71120	703307	4065250	348	265	244	74	234	74	2.00
MC	injectite	-120.72129	36.70780	703540	4064879	295	266	103	84	281	73	0.09
MC	injectite	-120.72214	36.70894	703460	4065003	314	267	271	42	228	35	0.28
MC	injectite	-120.72177	36.70848	703495	4064953	306	267	164	64	343	84	1.98
MC	injectite	-120.72188	36.70865	703484	4064971	308	267	234	73	226	79	1.83
MC	injectite	-120.72390	36.71151	703296	4065285	348	268	65	90	244	87	1.42

MC	injectite	-120.72367	36.71120	703318	4065251	343	268	238	65	224	70	0.43
MC	injectite	-120.72158	36.70822	703512	4064925	303	268	262	79	253	68	1.78
MC	injectite	-120.72133	36.70791	703535	4064891	298	269	63	83	66	86	0.81
MC	injectite	-120.72220	36.70901	703455	4065011	320	270	111	80	290	74	0.79
MC	injectite	-120.72220	36.70904	703455	4065014	320	270	271	75	258	60	0.36
MC	injectite	-120.72156	36.70822	703514	4064924	306	272	78	84	258	85	1.14
MC	injectite	-120.72365	36.71122	703319	4065253	346	272	243	90	242	88	1.83
MC	injectite	-120.72370	36.71123	703315	4065254	349	272	253	50	224	50	3.18
MC	injectite	-120.72368	36.71126	703317	4065258	347	272	99	82	278	77	0.64
MC	injectite	-120.72128	36.70795	703540	4064895	299	274	167	90	350	59	5.00
MC	injectite	-120.72375	36.71159	703310	4065294	351	280	71	90	249	84	2.00
MC	injectite	-120.72143	36.70825	703525	4064928	311	282	73	90	251	82	1.52
MC	injectite	-120.72071	36.70742	703592	4064838	292	284	179	64	356	87	2.00
MC	injectite	-120.72058	36.70735	703604	4064830	287	285	168	67	347	82	1.50
MC	injectite	-120.72136	36.70828	703532	4064932	313	289	87	90	263	75	1.22
MC	injectite	-120.72174	36.70887	703496	4064997	319	289	13	61	36	42	1.42
MC	injectite	-120.72137	36.70833	703531	4064938	316	292	333	21	142	12	5.00
MC	injectite	-120.72118	36.70813	703548	4064915	312	293	321	32	223	4	4.00
MC	injectite	-120.72148	36.70864	703520	4064971	316	294	338	44	360	12	3.05
MC	injectite	-120.72336	36.71136	703345	4065269	351	294	243	79	236	79	7.00
MC	injectite	-120.72179	36.70900	703492	4065011	330	299					1.04
MC	injectite	-120.72145	36.70860	703522	4064967	322	299	351	35	59	12	2.97
MC	injectite	-120.72333	36.71133	703348	4065266	356	299	74	79	78	89	0.51
MC	injectite	-120.72359	36.71166	703324	4065302	362	299	51	84	56	81	1.47
MC	injectite	-120.72155	36.70884	703513	4064993	321	299	322	32	221	4	1.12
MC	injectite	-120.72335	36.71136	703346	4065269	358	300	254	77	244	71	3.05
MC	injectite	-120.72331	36.71136	703350	4065269	357	301	237	90	57	89	2.13
MC	injectite	-120.72124	36.70831	703542	4064936	322	303	331	45	336	12	1.30
MC	injectite	-120.72152	36.70887	703516	4064996	322	303	157	48	155	81	1.22
MC	injectite	-120.72202	36.70968	703469	4065086	332	305	341	48	1	17	1.63
MC	injectite	-120.72111	36.70827	703554	4064931	325	311	236	88	235	90	0.27

MC	injectite	-120.72070	36.70775	703592	4064874	317	312	222	83	41	87	1.07
MC	injectite	-120.72074	36.70779	703588	4064879	318	312	351	78	359	48	1.07
MC	injectite	-120.72098	36.70809	703566	4064911	327	314	48	72	60	69	0.43
MC	injectite	-120.72110	36.70826	703555	4064930	330	314	60	86	62	87	0.53
MC	injectite	-120.72313	36.71146	703365	4065280	362	317	73	84	254	88	1.32
MC	injectite	-120.72331	36.71179	703348	4065317	365	318	234	80	229	84	1.40
MC	injectite	-120.72129	36.70891	703537	4065002	326	318					3.30
MC	injectite	-120.72311	36.71146	703367	4065280	363	319	63	88	243	90	2.59
MC	injectite	-120.72120	36.70885	703544	4064995	327	322	74	43	99	59	1.22
MC	injectite	-120.72127	36.70881	703538	4064990	333	322	95	46	111	69	0.94
MC	injectite	-120.72116	36.70867	703548	4064975	334	325	181	90	6	63	0.46
MC	injectite	-120.72154	36.70916	703513	4065029	345	327	189	73	8	81	1.78
MC	injectite	-120.72295	36.71149	703382	4065285	362	327	261	78	251	68	3.73
MC	injectite	-120.72307	36.71193	703369	4065333	365	334					0.36
MC	injectite	-120.72090	36.70836	703572	4064942	339	335	79	87	258	82	1.83
MC	injectite	-120.72283	36.71155	703392	4065292	365	337					3.94
MC	injectite	-120.72112	36.70893	703551	4065004	339	338	245	75	236	74	2.74
MC	injectite	-120.72171	36.70984	703496	4065104	350	339	343	52	1	21	3.05
MC	injectite	-120.72074	36.70820	703587	4064924	339	339					2.67
MC	injectite	-120.72279	36.71154	703395	4065290	366	339	252	86	248	80	0.43
MC	injectite	-120.72057	36.70809	703603	4064912	335	342					1.68
MC	injectite	-120.72135	36.70944	703530	4065061	345	344	307	73	298	43	0.33
MC	injectite	-120.72137	36.70942	703528	4065058	348	344	111	72	293	81	0.36
MC	injectite	-120.72064	36.70840	703596	4064947	333	345	63	90	242	88	0.58
MC	injectite	-120.72056	36.70828	703603	4064933	332	345	66	90	245	86	2.00
MC	injectite	-120.72072	36.70837	703589	4064943	341	346	255	72	242	66	1.83
MC	injectite	-120.72043	36.70844	703614	4064951	322	347	105	84	283	72	1.00
MC	injectite	-120.72266	36.71164	703407	4065301	366	348	51	88	53	84	0.99
MC	injectite	-120.72043	36.70842	703615	4064950	326	350	90	83	269	80	0.94
MC	injectite	-120.72020	36.70809	703636	4064913	322	350					13.97
MC	injectite	-120.72053	36.70842	703605	4064949	334	351	76	90	253	81	1.63

MC	injectite	-120.72040	36.70834	703617	4064941	328	351	79	90	256	79	1.07
MC	injectite	-120.72097	36.70898	703564	4065011	345	351	62	84	65	87	
MC	injectite	-120.72052	36.70843	703606	4064950	335	353	56	54	78	59	0.69
MC	injectite	-120.72080	36.70873	703581	4064983	344	353	182	72	1	80	1.52
MC	injectite	-120.72037	36.70847	703619	4064955	328	356	243	85	240	84	0.61
MC	injectite	-120.72104	36.70920	703558	4065034	348	356	162	79	343	69	0.61
MC	injectite	-120.72030	36.70842	703626	4064949	327	357	76	90	253	81	1.50
MC	injectite	-120.72078	36.70874	703583	4064984	349	358	181	73	0	79	1.02
MC	injectite	-120.72254	36.71170	703418	4065308	370	360	229	78	224	85	0.91
MC	injectite	-120.72134	36.70963	703530	4065082	359	360	25	65	45	51	2.13
MC	injectite	-120.72030	36.70839	703626	4064946	332	360	73	86	253	86	1.02
MC	injectite	-120.72192	36.71093	703474	4065224	357	361	356	43	39	19	0.61
MC	injectite	-120.72248	36.71167	703423	4065305	370	362	236	82	232	85	0.91
MC	injectite	-120.71992	36.70823	703661	4064929	317	364					3.05
MC	injectite	-120.72025	36.70853	703630	4064962	331	366	236	86	234	88	1.17
MC	injectite	-120.72027	36.70851	703628	4064959	334	367	242	87	240	86	0.86
MC	injectite	-120.71999	36.70829	703655	4064935	325	368	158	90	340	58	3.00
MC	injectite	-120.72008	36.70838	703646	4064946	328	369	210	85	32	79	0.42
MC	injectite	-120.72015	36.70847	703639	4064955	331	369	72	90	250	83	1.04
MC	injectite	-120.72094	36.70934	703567	4065050	357	372	182	90	7	63	1.52
MC	injectite	-120.72017	36.70858	703637	4064968	335	375	334	64	338	31	1.00
MC	injectite	-120.72061	36.70898	703597	4065011	352	376					1.93
MC	injectite	-120.72067	36.70906	703591	4065020	360	381	224	73	217	84	4.57
MC	injectite	-120.72093	36.70945	703567	4065062	364	381					3.51
MC	injectite	-120.71978	36.70858	703672	4064968	319	381	263	76	252	65	0.30
MC	injectite	-120.72216	36.71176	703451	4065316	373	383					0.69
MC	injectite	-120.72009	36.70859	703644	4064969	340	383	248	88	246	83	0.86
MC	injectite	-120.72030	36.70911	703624	4065026	351	394	156	55	155	88	1.07
MC	injectite	-120.71974	36.70858	703676	4064969	332	394	253	82	246	76	0.69
MC	injectite	-120.72045	36.70924	703611	4065040	359	396	252	85	247	79	2.44
MC	injectite	-120.71978	36.70859	703672	4064969	338	397	263	78	253	67	0.51

MC	injectite	-120.71991	36.70871	703660	4064982	344	398	246	84	242	81	0.71
MC	injectite	-120.71988	36.70871	703663	4064982	344	399	243	81	237	80	0.97
MC	injectite	-120.71976	36.70876	703674	4064989	336	401	239	70	228	73	0.91
MC	injectite	-120.71985	36.70884	703665	4064997	340	401	102	65	108	89	0.71
MC	injectite	-120.72037	36.70930	703617	4065047	359	401	250	64	233	63	4.57
MC	injectite	-120.71976	36.70879	703673	4064992	336	401	237	79	231	82	0.91
MC	injectite	-120.72036	36.70931	703618	4065048	358	402	132	43	137	75	0.66
MC	injectite	-120.71996	36.70889	703655	4065002	346	402	107	62	113	88	0.79
MC	injectite	-120.71951	36.70872	703696	4064984	331	408	81	72	87	86	0.86
MC	injectite	-120.71964	36.70884	703684	4064997	335	408	245	81	239	79	1.04
MC	injectite	-120.71946	36.70864	703701	4064976	333	411	253	89	250	82	0.48
MC	injectite	-120.71960	36.70884	703688	4064998	339	413	237	79	231	82	1.47
MC	injectite	-120.71972	36.70903	703677	4065018	345	417	44	82	51	75	0.04
MC	injectite	-120.72013	36.70948	703638	4065067	362	420					3.66
MC	injectite	-120.71902	36.70860	703740	4064972	323	424	102	71	285	86	0.76
MC	injectite	-120.71884	36.70828	703757	4064937	323	426	247	77	239	75	1.12
MC	injectite	-120.71912	36.70876	703731	4064989	328	427	72	90	250	83	0.10
MC	injectite	-120.71912	36.70876	703731	4064989	328	427	72	90	250	83	0.11
MC	injectite	-120.71912	36.70876	703731	4064989	328	427	72	90	250	83	0.17
MC	injectite	-120.71912	36.70876	703731	4064989	328	427	71	90	249	84	0.18
MC	injectite	-120.71891	36.70859	703750	4064971	322	429	94	71	278	89	0.81
MC	injectite	-120.71895	36.70858	703746	4064971	327	431	283	61	260	43	1.50
MC	injectite	-120.71927	36.70900	703717	4065016	341	436	238	83	234	85	1.55
MC	injectite	-120.71928	36.70896	703716	4065011	344	437	233	77	227	82	2.00
MC	injectite	-120.71942	36.70924	703702	4065042	345	437					0.20
MC	injectite	-120.71920	36.70897	703723	4065012	340	438	222	70	214	82	0.23
MC	injectite	-120.71756	36.70758	703873	4064863	283	442	230	76	224	83	0.06
MC	injectite	-120.71753	36.70757	703876	4064860	283	443	235	60	219	67	0.10
MC	injectite	-120.71755	36.70759	703874	4064863	285	444	242	67	228	69	0.08
MC	injectite	-120.71758	36.70762	703871	4064867	287	445	220	79	37	89	0.03
MC	injectite	-120.71774	36.70780	703856	4064886	291	445					0.13

MC	injectite	-120.71757	36.70759	703872	4064864	290	447	221	71	214	84	0.10
MC	injectite	-120.71784	36.70791	703847	4064898	303	451	221	48	201	64	0.43
MC	injectite	-120.71895	36.70901	703745	4065018	339	451	190	76	10	79	0.23
MC	injectite	-120.71883	36.70889	703756	4065005	338	453	97	76	279	83	0.07
MC	injectite	-120.71876	36.70877	703763	4064991	338	454	113	67	296	86	0.08
MC	injectite	-120.71901	36.70912	703740	4065030	343	454	242	73	232	74	0.94
MC	injectite	-120.71917	36.70936	703725	4065056	350	457	237	75	229	79	0.53
MC	injectite	-120.71901	36.70908	703739	4065026	349	457	240	71	229	74	1.00
MC	injectite	-120.71788	36.70806	703843	4064914	309	458	97	63	104	85	0.13
MC	injectite	-120.71804	36.70827	703828	4064937	318	462	108	58	115	85	0.09
MC	injectite	-120.71886	36.70921	703752	4065040	348	467	232	66	220	74	0.71
MC	injectite	-120.71801	36.70831	703831	4064942	322	467					0.20
MC	injectite	-120.71888	36.70916	703751	4065034	351	467	239	69	227	73	
MC	injectite	-120.71803	36.70831	703829	4064942	324	468					0.33
MC	injectite	-120.71877	36.70923	703761	4065042	346	471	241	64	226	67	0.56
MC	injectite	-120.71899	36.70944	703740	4065065	356	473	234	77	228	82	0.30
MC	injectite	-120.71760	36.70835	703867	4064947	307	477	179	42	170	72	0.20
MC	injectite	-120.71870	36.70925	703767	4065045	350	478					0.61
MC	injectite	-120.71771	36.70840	703857	4064953	317	481	232	81	228	86	0.09
MC	injectite	-120.71742	36.70816	703884	4064927	309	484					0.38
MC	injectite	-120.71772	36.70848	703856	4064962	322	487	222	69	214	81	0.05
MC	injectite	-120.71684	36.70777	703937	4064884	298	495	272	90	268	73	0.46
MC	injectite	-120.71774	36.70868	703854	4064983	330	497					0.20
MC	injectite	-120.71742	36.70852	703883	4064967	318	500					0.25
MC	injectite	-120.71765	36.70872	703862	4064988	328	502	231	83	229	89	0.23
MC	injectite	-120.71653	36.70768	703965	4064876	293	505	116	82	294	70	0.10
MC	injectite	-120.71699	36.70825	703922	4064938	306	506	222	70	214	82	0.18
MC	injectite	-120.71679	36.70797	703941	4064906	303	506	108	61	114	87	0.10
MC	injectite	-120.71763	36.70883	703864	4065001	334	510	247	84	242	81	0.48
MC	injectite	-120.71686	36.70808	703935	4064919	308	510	106	63	112	89	0.46
MC	injectite	-120.71756	36.70880	703870	4064998	331	510	224	79	221	89	0.18

MC	injectite	-120.71753	36.70875	703873	4064991	331	510	240	70	229	73	0.18
MC	injectite	-120.71685	36.70805	703935	4064915	310	511	27	76	39	61	0.51
MC	injectite	-120.71738	36.70858	703887	4064974	326	511	221	75	216	87	0.25
MC	injectite	-120.71778	36.70903	703850	4065023	341	513					0.01
MC	injectite	-120.71732	36.70864	703892	4064980	328	516	212	79	30	85	0.33
MC	injectite	-120.71725	36.70869	703898	4064986	325	519					0.03
MC	injectite	-120.71389	36.70655	704204	4064756	311	626	156	90	337	57	1.50

Table 12: Bedding and injectite orientation measurements and injectite aperture measurements collected in Moreno Gulch (MG) and Marca Canyon (MC). Easting and northing are in the NAD83 UTM Zone 10N coordinate system. TSP is True Stratigraphic Position above the top of the Uhalde Formation (the PGIC source). Paleostrike and paleodip record the rotated orientation of data (i.e., paleo-orientation).

APPENDIX 4: UNMANNED AERIAL VEHICLE DATA ACQUISITION AND PROCESSING OF MORENO GULCH, PANOCHE HILLS

A camera-equipped UAV was used to acquire aerial photography over the course of a week in October 2014 to obtain high-resolution (cm-scale) aerial imagery and elevation data of Moreno Gulch. A DJI Phantom 2 UAV unit with a GoPro Hero3 mounted via gimbal was flown at ~30 m above ground level, in an effort to achieve a uniform photographic resolution. Actual UAV elevation likely fluctuated between 10-50 m as a result of extreme topography within the locale. In order to georeference the photogrammetric model, a grid of control points was acquired with a high-precision (dm-scale) Trimble GEOXH 6000 handheld GPS unit with a pole-mounted Trimble Zephyr 2 antennae. Control points were spaced ~100 m apart and were code (preferred) or carrier-processed using Trimble Pathfinder Office software.

Roughly 10,000 photographs were manually selected for photogrammetric modeling. Agisoft PhotoScan Pro software was used to align photographs and georeference them to control points, after which the project was divided into four subsets to compensate for the extraordinary number of photographs. Each subset was then used to generate point clouds, meshes, and photographic textures in PhotoScan Pro. Resulting models were then exported as point clouds or DEM/orthophoto pairs for merging and mapping in Applied Imagery Quick Terrain Modeler or ArcGIS Desktop, respectively.

References

Abe, H., L. Keer, and T. Mura (1976), Growth rate of a penny-shaped crack in hydraulic fracturing of rocks, *Journal of Geophysical Research*, *81*(35), 6292-6298.

Alegret, L., E. Molina, and E. Thomas (2001), Benthic Foraminifera at the Cretaceous-Tertiary boundary around the Gulf of Mexico, *Geology*, *29*(10), 891-894.

Allmendinger, R. W., N. Cardozo, and D. Fisher (2012), Structural Geology Algorithms, *Vectors and Tensors in Structural Geology*, 289.

Alvarez, L. W., W. Alvarez, F. Asaro, and H. V. Michel (1980), Extraterrestrial cause for the Cretaceous Tertiary extinction, *Science*, *208*(4448), 1095-1108.

Alvarez, W., P. Claeys, and S. W. Kieffer (1995), Emplacement of Cretaceous-Tertiary boundary shocked quartz from Chicxulub crater, *Science*, *269*(5226), 930-935.

Alvarez, W., J. Smit, W. Lowrie, F. Asaro, S. V. Margolis, P. Claeys, M. Kastner, and A. R. Hildebrand (1992), Proximal impact deposits at the Cretaceous-Tertiary boundary in the Gulf of Mexico; a restudy of DSDP Leg 77 sites 536 and 540; with Suppl. Data 92-25, *Geology*, *20*(8), 697-700.

Anderson, R., and R. W. Pack (1915), *Geology and oil resources of the west border of the San Joaquin Valley north of Coalinga, California*, US Government Printing Office.

Artemieva, N., and J. Morgan (2009), Modeling the formation of the K-Pg boundary layer, *Icarus*, *201*(2), 768-780.

Atwater, T. (1970), Implications of plate tectonics for the Cenozoic tectonic evolution of western North America, *Geological Society of America Bulletin*, *81*(12), 3513-3536.

Bartow, J. A. (1996), *Geologic Map of the West Border of the San Joaquin Valley in the Panoche Creek-Cantua Creek Area, Fresno and San Benito Counties, California*, US Geological Survey.

Blakey, R. W. (2011), Cretaceous-Tertiary (65 Ma) North American Paleogeographic Map, in *Paleogeography and Geologic Evolution of North America*, edited by R. W. Blakey, Colorado Plateau Geosystems.

Blakey, R. W. (2013), North American Late Cretaceous and Paleogene Paleotectonic Maps, in *Paleogeographic and Tectonic History of North America*, edited by R. W. Blakey, Colorado Plateau Geosystems.

Boslough, M. B., E. Chael, T. Trucano, and D. Crawford (1995), Axial focusing of energy from a hypervelocity impact on earth, *International Journal of Impact Engineering*, *17*(1), 99-108.

Bralower, T. J., C. K. Paull, and R. M. Leckie (1998), The Cretaceous-Tertiary boundary cocktail; Chicxulub impact triggers margin collapse and extensive sediment gravity flows, *Geology*, *26*(4), 331-334.

Bralower, T. J., L. Eccles, J. Kutz, T. Yancey, J. Schueth, M. A. Arthur, and D. Bice (2010), Grain size of Cretaceous-Paleogene boundary sediments from Chicxulub to the open ocean; implications for interpretation of the mass extinction event, *Geology*, *38*(3), 199-202.

Buffler, R. T. (1991), Early evolution of the Gulf of Mexico basin, in *An Introduction to Central Gulf Coast Geology*, edited by D. Goldthwaite, pp. 1-15, New Orleans Geological Society, New Orleans, LA.

Buffler, R. T., and D. S. Sawyer (1985), Distribution of crust and early history, Gulf of Mexico basin, *GCAGS Trans.*, *35*, 333-344.

Buffler, R. T., et al. (1984), *Intl. Repts. DSDP, 77*, U.S. Government Printing Office, Washington, D. C.

Bunge, H.-P., and S. P. Grand (2000), Mesozoic plate-motion history below the northeast Pacific Ocean from seismic images of the subducted Farallon slab, *Nature*, *405*(6784), 337-340.

Burger, H. R., A. F. Sheehan, and C. H. Jones (2006), *Introduction to Applied Geophysics: Exploring the Shallow Subsurface*, 600 pp., W. W. Norton & Company, New York City, NY.

Campbell, C. E., F. E. Oboh-Ikuenobe, and T. L. Eifert (2007), Megatsunami deposit in Cretaceous-Paleogene boundary interval of southeastern Missouri, *GSA Special Paper*, *437*, 189-198.

Cantu-Chapa, A., and R. Landeros-Flores (2001), The Cretaceous-Paleocene boundary in the subsurface Campeche Shelf, southern Gulf of Mexico, *AAPG Memoir*, *75*, 389-395.

Cardozo, N., and R. W. Allmendinger (2013), Spherical projections with OSXStereonet, *Computers & Geosciences*, *51*, 193-205.

Chang, C., L. C. McNeill, J. C. Moore, W. Lin, M. Conin, and Y. Yamada (2010), In situ stress state in the Nankai accretionary wedge estimated from borehole wall failures, *Geochemistry, Geophysics, Geosystems*, *11*(12).

Christeson, G., D. Eddy, H. van Avendonk, I. Norton, G. Karner, C. Johnson, E. Kneller, and J. Snedden (2013), Deep Crustal Structure Northeastern Gulf of Mexico, paper presented at EGU General Assembly, European Geosciences Union, Vienna, Austria, 7-12 April 2013.

Christeson, G. L., G. S. Collins, J. V. Morgan, S. P. Gulick, P. J. Barton, and M. R. Warner (2009), Mantle deformation beneath the Chicxulub impact crater, *Earth and Planetary Science Letters*, *284*(1), 249-257.

Claeys, P., W. Kiessling, and W. Alvarez (2002), Distribution of Chicxulub ejecta at the Cretaceous-Tertiary boundary, *Special Paper - Geological Society of America*, *356*, 55-68.

Covey, C., S. L. Thompson, P. R. Weissman, and M. C. MacCracken (1994), Global climatic effects of atmospheric dust from an asteroid or comet impact on Earth, *Global and Planetary Change*, *9*(3), 263-273.

Day, S., and M. Maslin (2005), Linking large impacts, gas hydrates, and carbon isotope excursions through widespread sediment liquefaction and continental slope failure: The example of the KT boundary event, *GSA Special Paper*, *384*, 239-258.

DeGraaff-Surpless, K., S. A. Graham, J. L. Wooden, and M. O. McWilliams (2002), Detrital zircon provenance analysis of the Great Valley Group, California: Evolution of an arc-forearc system, *Geological Society of America Bulletin*, *114*(12), 1564-1580.

Denne, R. A., and R. H. Blanchard (2013), Regional Controls on the Formation of the Ancestral DeSoto Canyon by the Chicxulub Impact, *GCAGS Journal*, *2*, 17-28.

Denne, R. A., E. D. Scott, D. P. Eickhoff, J. S. Kaiser, R. J. Hill, and J. M. Spaw (2013), Massive Cretaceous-Paleogene boundary deposit, deep-water Gulf of Mexico: New evidence for widespread Chicxulub-induced slope failure, *Geology*, *41*(9), 983-986.

Dickinson, W., and D. Seely (1979), Structure and stratigraphy of forearc regions, *AAPG Bulletin*, *63*(1), 2-31.

Dickinson, W. R. (1976), Sedimentary basins developed during evolution of Mesozoic-Cenozoic arc-trench system in western North America, *Canadian Journal of Earth Sciences*, *13*(9), 1268-1287.

Dooley, T. P., M. P. A. Jackson, and M. R. Hudec (2013), Coeval extension and shortening above and below salt canopies on an uplifted, continental margin; application to the northern Gulf of Mexico, *AAPG Bulletin*, *97*(10), 1737-1764.

Dunham, R. J. (1962), Classification of carbonate rocks according to depositional textures, in *Classification of Carbonate Rocks—A Symposium*, edited by W. E. Ham, pp. 108-121, American Association of Petroleum Geologists, Denver, CO.

Durham, J. W. (1943), Pacific coast Cretaceous and Tertiary corals, *Journal of Paleontology*, 196-202.

Engebretson, D. C., A. Cox, and R. G. Gordon (1985), Relative motions between oceanic and continental plates in the Pacific basin, *Geological Society of America Special Papers*, *206*, 1-60.

England, A., and A. Green (1963), Some two-dimensional punch and crack problems in classical elasticity, paper presented at Mathematical Proceedings of the Cambridge Philosophical Society, Cambridge Univ Press.

Ewing, T. E. (1991), Structural framework, in *The Gulf of Mexico Basin*, edited by A. Salvador, pp. 31-52, Geological Society of America, Boulder, CO.

Ferrell, R., D. T. King, Jr., and L. W. Petruny (2011), Nontronitic clay pseudomorphs of Cretaceous-Paleogene (K-T) boundary microtektites, Shell Creek, Alabama, U.S.A, *Journal of Sedimentary Research*, *81*(5), 348-354.

Fiduk, J. C., et al. (1999), The Perdido fold belt, northwestern deep Gulf of Mexico, Part 2; Seismic stratigraphy and petroleum systems, *AAPG Bulletin*, *83*(4), 578-612.

Fisher, R. (1953), Dispersion on a sphere, *Proceedings of the Royal Society of London. Series A. Mathematical and Physical Sciences*, *217*(1130), 295-305.

Fourcade, É., R. Rocchia, S. Gardin, J.-P. Bellier, P. Debrabant, E. Masure, E. Robin, and W. T. Pop (1998), Age of the Guatemala breccias around the Cretaceous-Tertiary boundary: relationships with the asteroid impact on the Yucatan, *Comptes Rendus de l'Académie des Sciences-Series IIA-Earth and Planetary Science*, *327*(1), 47-53.

Frederiksen, N. O., et al. (1982), Biostratigraphy and paleoecology of lower Paleozoic, Upper Cretaceous, and lower Tertiary rocks in U. S. Geological Survey New Madrid test wells, southeastern Missouri, *Tulane Studies in Geology and Paleontology*, *17*(2), 23-45.

French, B. M. (1998), *Traces of Catastrophe: A Handbook of Shock-Metamorphic Effects in Terrestrial Meteorite Impact Structures*, 117 pp., Lunar and Planetary Institute, Houston, TX.

Friedmann, J., P. Vrolijk, X. Ying, A. Despandhe, G. Moir, and D. Mohrig (2002), Quantitative Analysis of Sandstone Intrusion Networks, Panoche Hills, California, paper presented at AAPG Annual Meeting 2002.

Geertsma, J. (1989), Two-Dimensional Fracture-Propagation Models, in *Recent Advances in Hydraulic Fracturing*, edited by J. L. Gidley, S. A. Holditch, D. E. Nierode and J. Veatch, R. W., pp. 81-94, Society of Petroleum Engineers, Richardson, TX.

Geertsma, J., and F. De Klerk (1969), A rapid method of predicting width and extent of hydraulically induced fractures, *Journal of Petroleum Technology*, *21*(12), 1,571-571,581.

Gilmour, I., and E. Anders (1989), Cretaceous-Tertiary boundary event: Evidence for a short time scale, *Geochimica et Cosmochimica Acta*, *53*(2), 503-511.

Goldin, T. J., and H. J. Melosh (2007), Interactions Between Chicxulub Ejecta and the Atmosphere: The Deposition of the K/T Double Layer, paper presented at 38th LPI Conference, Lunar and Planetary Institute, League City, TX.

Graham, S. A. (1987), Tectonic controls on petroleum occurrence in central California, *Cenozoic Basin Development of Coastal California*, 47-63.

Grajales-Nishimura, J. M., E. Cedillo Pardo, C. Rosales-Dominguez, D. J. Moran-Zenteno, W. Alvarez, P. Claeys, J. Ruiz-Morales, J. Garcia-Hernandez, P. Padilla-Avila, and A. Sanchez-Rios (2000), Chicxulub impact; the origin of reservoir and seal facies in the southeastern Mexico oil fields, *Geology*, *28*(4), 307-310.

Gulick, S. P. S., and P. J. Barton (2005), The 2005 Chicxulub Impact Crater Seismic Experiment*Rep.*, 20 pp, The University of Texas Institute for Geophysics, Austin, TX.

Gulick, S. P. S., G. Christeson, P. Barton, R. Grieve, J. Morgan, and J. Urrutia-Fucugauchi (2013), Geophysical characterization of the Chicxulub impact crater, *Reviews of Geophysics*, *51*(1), 31-52.

Gulick, S. P. S., et al. (2008), Importance of pre-impact crustal structure for the asymmetry of the Chicxulub impact crater, *Nature Geoscience*, *1*(2), 131-135.

Hart, M. B., P. J. Harries, and A. L. Cárdenas (2013), The Cretaceous/Paleogene Boundary Events in the Gulf Coast: Comparisons between Alabama and Texas, *GCAGS Trans.*, *63*, 235-255.

Hildebrand, A. R., and W. V. Boynton (1990), Proximal Cretaceous-Tertiary boundary impact deposits in the Caribbean, *Science*, *248*(4957), 843-847.

Hubbert, M. K., and D. G. Willis (1957), Mechanics of Hydraulic Fracturing, *SPE Transactions*, *210*, 153-168.

Hubbert, M. K., and D. G. Willis (1972), Mechanics of hydraulic fracturing, in *Underground Waste Management and Environmental Implications*, edited, pp. 239-287, AAPG.

Hudec, M. R., M. P. A. Jackson, and F. J. Peel (2013a), Influence of deep Louann structure on the evolution of the northern Gulf of Mexico, *AAPG Bulletin*, *97*(10), 1711-1735.

Hudec, M. R., I. O. Norton, M. P. A. Jackson, and F. J. Peel (2013l), Jurassic evolution of the Gulf of Mexico salt basin, *AAPG Bulletin*, *97*(10), 1683-1710.

Hurst, A., A. Scott, and M. Vigorito (2011), Physical characteristics of sand injectites, *Earth-Science Reviews*, *106*(3), 215-246.

Ibrahim, A., J. Carye, G. Latham, and R. Buffler (1981), Crustal structure in Gulf of Mexico from OBS refraction and multichannel reflection data, *AAPG Bulletin*, *65*(7), 1207-1229.

Ingersoll, R. V. (1979), Evolution of the Late Cretaceous forearc basin, northern and central California, *Geological Society of America Bulletin*, *90*(9), 813-826.

Ingersoll, R. V. (1983), Petrofacies and provenance of late Mesozoic forearc basin, northern and central California, *AAPG Bulletin*, *67*(7), 1125-1142.

Izett, G. A. (1990), The Cretaceous/Tertiary boundary interval, Raton Basin, Colorado and New Mexico, and its content of shock-metamorphosed minerals; evidence relevant to the K/T boundary impact-extinction theory, *Special Paper - Geological Society of America*, *249*, 1-100.

Jablonski, D. (1994), Extinctions in the fossil record, *Philosophical Transactions of the Royal Society of London, Series B: Biological Sciences*, *344*(1307), 11-17.

Jenkins, O. P. (1930), Sandstone dikes as conduits for oil migration through shales, *AAPG bulletin*, *14*(4), 411-421.

Keller, G. (2011), The Cretaceous-Tertiary mass extinction; theories and controversies, *SEPM Special Publication*, *100*, 7-22.

Keller, G., N. MacLeod, J. B. Lyons, and C. B. Officer (1993), Is there evidence for Cretaceous-Tertiary boundary-age deep-water deposits in the Caribbean and Gulf of Mexico?; with Suppl. Data 9331, *Geology*, *21*(9), 776-780.

Keller, G., W. Stinnesbeck, T. Adatte, and D. Stueben (2003a), Multiple impacts across the Cretaceous-Tertiary boundary, *Earth-Science Reviews*, *62*(3-4), 327-363.

Keller, G., W. Stinnesbeck, T. Adatte, B. Holland, D. Stueben, M. Harting, C. de Leon, and J. de la Cruz (2003b), Spherule deposits in Cretaceous-Tertiary boundary sediments in Belize and Guatemala, *Journal of the Geological Society of London*, *160*(5), 783-795.

King, D. T., and L. W. Petruny (2007), Impact spherule-bearing, Cretaceous-Tertiary boundary sand body, Shell Creek stratigraphic section, Alabama, USA, *Geological Society of America Special Papers*, *437*, 179-187.

Kiyokawa, S., et al. (2002), Cretaceous-Tertiary boundary sequence in the Cacarajicara Formation, western Cuba; an impact-related, high-energy, gravity-flow deposit, *GSA Special Paper*, *356*, 125-144.

Klaus, A., R. D. Norris, D. Kroon, and J. Smit (2000), Impact-induced mass wasting at the K-T boundary; Blake Nose, western North Atlantic, *Geology*, *28*(4), 319-322.

Klitgord, K. D., and H. Schouten (1986), Plate kinematics of the central Atlantic, in *The Gulf of Mexico Basin*, edited by A. Salvador, pp. 351-378, Geological Society of America, Boulder, CO.

Kyte, F. T., J. Smit, and J. T. Wasson (1985), Siderophile interelement variations in the Cretaceous-Tertiary boundary sediments from Caravaca, Spain, *Earth and Planetary Science Letters*, *73*(2-4), 183-195.

MacLeod, K. G., D. L. Whitney, B. T. Huber, and C. Koeberl (2007), Impact and extinction in remarkably complete Cretaceous-Tertiary boundary sections from Demerara Rise, tropical western North Atlantic, *GSA Bulletin*, *119*(1-2), 101-115.

Martin, L. (1964), *Upper Cretaceous and Lower Tertiary Foraminifera from Fresno County, California*, Geologische Bundesanstalt.

Marton, G. L., and R. T. Buffler (1999), Jurassic—early cretaceous tectono-paleogeographic evolution of the southeastern gulf of Mexico basin, *Sedimentary Basins of the World*, *4*, 63-91.

McGuinness, D. B., and J. R. Hossack (1993), The development of allochthonous salt sheets as controlled by the rates of extension, sedimentation, and salt supply, paper

presented at 14th Annual GCAGS SEPM Research Conference, Society for Sedimentary Geology (SEPM).

McGuire, D. J. (1988), Stratigraphy, depositional history, and hydrocarbon source-rock potential of the Upper Cretaceous-Lower Tertiary Moreno Formation, central San Joaquin basin, California, Stanford University.

Miller, K. G., R. M. Sherrell, J. V. Browning, M. P. Field, W. Gallagher, R. K. Olsson, P. J. Sugarman, S. Tuorto, and H. Wahyudi (2010), Relationship between mass extinction and iridium across the Cretaceous-Paleogene boundary in New Jersey, *Geology*, *38*(10), 867-870.

Milsom, J. (2007), *Field geophysics*, John Wiley and Sons, West Sussex, United Kingdom.

Minisini, D., and H. Schwartz (2007), An early Paleocene cold seep system in the Panoche and Tumey Hills, central California (United States).

Mitchell, C., S. A. Graham, and D. H. Suek (2010), Subduction complex uplift and exhumation and its influence on Maastrichtian forearc stratigraphy in the Great Valley Basin, northern San Joaquin Valley, California, *Geological Society of America Bulletin*, *122*(11-12), 2063-2078.

Morgan, J., J. Urrutia-Fucugauchi, S. P. S. Gulick, G. Christeson, P. Barton, M. Rebolledo-Vieyra, and J. Melosh (2005), Chicxulub crater seismic survey prepares way for future drilling, *Eos Trans. AGU*, *86*(36), 325-328.

Morgan, J., et al. (1997), Size and morphology of the Chicxulub impact crater, *Nature*, *390*(6659), 472-476.

Mount, V. S., K. Dull, and S. Mentemeier (2007), Structural style and evolution of traps in the paleogene play, deepwater Gulf of Mexico, paper presented at 27th Annual GCAGS SEPM Research Conference, Society for Sedimentary Geology (SEPM), Houston, TX.

Natland, M. (1957), Paleoecology of west coast Tertiary sediments, *Geological Society of America Memoirs*, *67*, 543-571.

Nordgren, R. (1972), Propagation of a vertical hydraulic fracture, *Society of Petroleum Engineers Journal*, *12*(04), 306-314.

Norris, R. D., and J. Firth (1999), Mass failure of the eastern North American margin triggered by the K/T impact, paper presented at GSA Annual Meeting, Geological Society of America, Denver, CO.

Norris, R. D., J. Firth, J. S. Blusztajn, and G. Ravizza (2000), Mass failure of the North Atlantic margin triggered by the Cretaceous-Paleogene bolide impact, *Geology*, *28*(12), 1119-1122.

Norton, I., H. van Avendonk, G. Christeson, and D. Eddy (2013), Crustal structure of the northern Gulf of Mexico from potential fields and seismic refraction, paper presented at EGU General Assembly, European Geosciences Union, Vienna, Austria.

Ocampo, A. C., K. O. Pope, and A. G. Fischer (1996), Ejecta blanket deposits of the Chicxulub crater from Albion Island, Belize, *The Cretaceous-Tertiary event and other catastrophes in Earth history*, 75-88.

Pälike, H. (2013), Impact and extinction, *Science*, *339*(6120), 655-656.

Payne, M. B. (1951), *Type Moreno Formation and overlying Eocene strata on the west side of the San Joaquin Valley, Fresno and Merced counties, California*, State of California, Department of Natural Resources, Division of Mines.

Payne, M. B. (1962), Type Panoche Group (Upper Cretaceous) and overlying Moreno and Tertiary strata on the west side of the San Joaquin Valley, *California Division of Mines and Geology Bulletin*, *181*, 165-175.

Perch-Nielsen, K., J. McKenzie, and Q. He (1982), Biostratigraphy and isotope stratigraphy and the 'catastrophic'extinction of calcareous nannoplankton at the Cretaceous/Tertiary boundary, *GSA Special Paper*, *190*, 353-371.

Perfit, M. R., and W. W. Chadwick Jr (1998), Magmatism at mid-ocean ridges: Constraints from volcanological and geochemical investigations, *Geophysical Monograph Series*, *106*, 59-115.

Perkins, T., and L. Kern (1961), Widths of hydraulic fractures, *Journal of Petroleum Technology*, *13*(09), 937-949.

Phelps, R. M. (2012), Middle-Hauterivian to Lower-Campanian sequence stratigraphy and stable isotope geochemistry of the Comanche Platform, South Texas, The University of Texas at Austin, Austin, TX.

Pilcher, R. S., B. Kilsdonk, and J. Trude (2011), Primary basins and their boundaries in the deep-water northern Gulf of Mexico; origin, trap types, and petroleum system implications, *AAPG Bulletin*, *95*(2), 219-240.

Pindell, J. L. (1993), Regional synopsis of Gulf of Mexico and Caribbean evolution, paper presented at 13th Annual SEPM Research Conference, SEPM.

Pope, K. O., A. C. Ocampo, A. G. Fischer, F. J. Vega, D. E. Ames, D. T. King Jr, B. W. Fouke, R. J. Wachtman, and G. Kletetschka (2005), Chicxulub impact ejecta deposits in southern Quintana Roo, México, and central Belize, *GSA Special Paper*, *384*, 171-190.

Raup, D. M., and J. Sepkoski, John (1982), Mass extinctions in the marine fossil record, *Science*, *215*(4539), 1501-1503.

Renne, P. R., A. L. Deino, F. J. Hilgen, K. F. Kuiper, D. F. Mark, W. S. Mitchell, III, L. E. Morgan, R. Mundil, and J. Smit (2013), Time scales of critical events around the Cretaceous-Paleogene boundary, *Science*, *339*(6120), 684-687.

Richardson, G., L. D. Nixon, C. M. Bohannon, E. G. Kazanis, T. M. Montgomery, and M. P. Gravois (2008), Deepwater Gulf of Mexico 2008: America's Offshore Energy Future*Rep.*, 112 pp, U.S. Department of the Interior, New Orleans, LA.

Ricoy-Paramo, V. (2005), 3D seismic characterisation of the Cantarell Field, Campheche Basin, Mexico, Doctoral thesis, 418 pp, Cardiff University, Cardiff, Wales, United Kingdom.

Rohde, R. A., and R. A. Muller (2005), Cycles in fossil diversity, *Nature*, *434*(7030), 208-210.

Sahagian, D., O. Pinous, A. Olferiev, and V. Zakharov (1996), Eustatic curve for the Middle Jurassic-Cretaceous based on Russian platform and Siberian stratigraphy: zonal resolution, *AAPG Bulletin*, *80*(9), 1433.

Salvador, A. (1991), Origin and development of the Gulf of Mexico basin, in *The Gulf of Mexico Basin*, edited by A. Salvador, pp. 389-444, The Geological Society of America, Boulder, CO.

Sawyer, D. S., R. T. Buffler, and R. H. Pilger Jr (1991), The crust under the Gulf of Mexico Basin, in *The Gulf of Mexico Basin*, edited by A. Salvador, pp. 53-72, The Geological Society of America, Boulder, CO.

Schulte, P., A. Deutsch, T. Salge, J. Berndt, A. Kontny, K. MacLeod, R. Neuser, and S. Krumm (2009), A dual-layer Chicxulub ejecta sequence with shocked carbonates from the Cretaceous–Paleogene (K–Pg) boundary, Demerara Rise, western Atlantic, *Geochimica et Cosmochimica Acta*, *73*(4), 1180-1204.

Schulte, P., et al. (2010), The Chicxulub asteroid impact and mass extinction at the Cretaceous-Paleogene boundary, *Science*, *327*(5970), 1214-1218.

Schwartz, H., J. Sample, K. D. Weberling, D. Minisini, and J. C. Moore (2003), An ancient linked fluid migration system: cold-seep deposits and sandstone intrusions in the Panoche Hills, California, USA, *Geo-Marine Letters*, *23*(3-4), 340-350.

Scott, A., A. Hurst, and M. Vigorito (2013), Outcrop-based reservoir characterization of a kilometer-scale sand-injectite complex, *AAPG bulletin*, *97*(2), 309-343.

Scott, E. D., R. A. Denne, J. S. Kaiser, and D. P. Eickhoff (2014), Impact on Sedimentation into the North-Central Deepwater Gulf of Mexico as as Result of the Chicxulub Event, *GCAGS Journal*, *3*, 41-50.

Scott, T. M., and D. Anderson (2001), Text to accompany the Geologic Map of Florida*Rep.*, Florida Geological Survey, Tallahasse, FL.

Sharpton, V. L., L. E. Marin, and B. C. Schuraytz (1994), The Chicxulub multiring basin: evaluation of geophysical data, well logs, and drill core samples, in *New Developments Regarding the KT Event and Other Catastrophes in Earth History*, edited by W. Alvarez, et al., p. 108, Lunar and Planetary Institute, Houston, TX.

Sharpton, V. L., L. E. Marin, J. L. Carney, S. Lee, G. Ryder, B. C. Schuraytz, P. Sikora, and P. D. Spudis (1996), A model of the Chicxulub impact basin based on evaluation of geophysical data, well logs, and drill core samples, *GSA Special Paper*, *307*, 55-74.

Sheriff, R. E. (1980), *Seismic Stratigraphy*, Springer, Boston, MA.

Shipley, T., L. Gahagan, K. Johnson, and M. Davis (2013), Seismic Data Center, edited, The University of Texas Institute for Geophysics, Austin, TX, United States.

Simmons, G. R. (1992), The regional distribution of salt in the northwestern Gulf of Mexico: styles of emplacement and implications for early tectonic history, 180 pp, Texas A&M University, College Station, TX.

Smit, J. (1999), The global stratigraphy of the Cretaceous-Tertiary boundary impact ejecta, *Annual Review of Earth and Planetary Sciences*, *27*(1), 75-113.

Smit, J., and J. Hertogen (1980), An extraterrestrial event at the Cretaceous-Tertiary boundary, *Nature*, *285*(5762), 198-200.

Smit, J., T. B. Roep, W. Alvarez, A. Montanari, P. Claeys, J. M. Grajales-Nishimura, and J. Bermudez (1996), Coarse-grained, clastic sandstone complex at the K/T boundary around the Gulf of Mexico; deposition by tsunami waves induced by the Chicxulub impact?, *GSA Special Paper*, *307*, 151-182.

Smit, J., A. Montanari, N. H. M. Swinburne, W. Alvarez, A. R. Hildebrand, S. V. Margolis, P. F. Claeys, W. Lowrie, and F. Asaro (1992), Tektite-bearing, deep-water clastic unit at the Cretaceous-Tertiary boundary in northeastern Mexico, *Geology*, *20*(2), 99-103.

Smith, L. A., and B. W. McNeely (1970), Summary of Leg 10, biostratigraphy, in *Intl. Rept. DSDP, 10*, edited by J. L. Worzel, pp. 731-736, U.S. Government Printing Office, Washington, D. C.

Smyers, N. B., and G. L. Peterson (1971), Sandstone dikes and sills in the Moreno shale, Panoche Hills, California, *Geological Society of America Bulletin*, *82*(11), 3201-3208.

Snedden, J. W., and J. F. Sarg (2008), Seismic Stratigraphy: A Primer on Methodology, *AAPG Search and Discovery*, *40270*.

Snedden, J. W., I. A. Norton, and J. C. Sanford (2014), Interaction of deep-water deposition and a mid-ocean spreading center, Eastern Gulf of Mexico Basin, USA, in *64th Annual GCAGS Convention*, edited, Gulf Coast Association of Geolocial Sciences, Lafayette, LA.

Soria, A. R., C. L. Liesa, M. P. Mata, J. A. Arz, L. Alegret, I. Arenillas, and A. Melendez (2001), Slumping and a sandbar deposit at the Cretaceous-Tertiary boundary in the El Tecolote section (northeastern Mexico); an impact-induced sediment gravity flow, *Geology*, *Geological Society of America*(3), 231-234.

Stinnesbeck, W., et al. (1993), Deposition of channel deposits near the Cretaceous-Tertiary boundary in northeastern Mexico; catastrophic or 'normal' sedimentary deposits?, *Geology*, *21*(9), 797-800.

Stock, C. (1939), Occurrence of Cretaceous reptiles in the Moreno shales of the Southern Coast Ranges, California, *Proceedings of the National Academy of Sciences of the United States of America*, *25*(12), 617.

Tada, R., et al. (2002), Complex tsunami waves suggested by the Cretaceous-Tertiary boundary deposit at the Moncada section, western Cuba, *GSA Special Paper*, *356*, 109-123.

Tada, R., et al. (2003), K/T boundary deposits in the paleo-western Caribbean Basin, in *The Circum-Gulf of Mexico and the Caribbean: Hydrocarbon habitats, basin formation, and plate tectonics*, edited by C. Bartolini and R. T. Buffler, pp. 582-604, AAPG Memoir, Tulsa, OK.

Trudgill, B. D., M. G. Rowan, J. C. Fiduk, P. Weimer, P. E. Gale, B. E. Korn, R. L. Phair, W. T. Gafford, G. R. Roberts, and S. W. Dobbs (1999), The Perdido fold belt, northwestern deep Gulf of Mexico; Part 1, Structural geometry, evolution and regional implications, *AAPG bulletin*, *83*(1), 88-113.

Trudgill, B. D., et al. (1995), The geological evolution of the deep water Perdido Foldbelt, Alaminos Canyon, northwestern deep Gulf of Mexico, *AAPG Bulletin*, *79*(10), 1568-1568.

Vail, P. R. (1987), Seismic stratigraphy interpretation using sequence stratigraphy: Part 1: Seismic stratigraphy interpretation procedure, in *Atlas of Seismic Stratigraphy*, edited by A. W. Bally, pp. 1-10, American Association of Petroleum Geologists, Tulsa, OK.

Vail, P. R., and R. M. Mitchum, Jr. (1979), Global Cycles of Relative Changes of Sea Level from Seismic Stratigraphy: Resources, Comparative Structure, and Eustatic Changes in Sea Level, in *Geological and Geophysical Investigations of Continental Margins*, edited, American Association of Petroleum Geologists, Tulsa, OK.

Van Wagoner, J. C. (1988), An overview of the fundamentals of sequence stratigraphy and key definitions, *SEPM Special Publication*, *42*.

Vétel, W., and J. Cartwright (2010), Emplacement mechanics of sandstone intrusions: insights from the Panoche Giant Injection Complex, California, *Basin Research*, *22*(5), 783-807.

Vigorito, M. (2007), Architecture and Internal Geometry of a Giant Intrusive-Extrusive Complex, Panoche Hills-Central Coastal Range, CA, USA, paper presented at 2007 AAPG Annual Convention and Exhibition.

Vigorito, M., and A. Hurst (2010), Regional sand injectite architecture as a record of pore-pressure evolution and sand redistribution in the shallow crust: insights from the

Panoche Giant Injection Complex, California, *Journal of the Geological Society*, *167*(5), 889-904.

Vigorito, M., A. Hurst, J. Cartwright, and A. Scott (2008), Regional-scale subsurface sand remobilization: geometry and architecture, *Journal of the Geological Society*, *165*(3), 609-612.

Ward, S. N. (2011), Tsunami, in *Encyclopedia of Solid Earth Geophysics*, edited by H. K. Gupta, pp. 1473-1493, Springer, Amsterdam, Netherlands.

Ward, W. C., G. Keller, W. Stinnesbeck, and T. Adatte (1995), Yucatan subsurface stratigraphy; implications and constraints for the Chicxulub impact, *Geology*, *23*(10), 873-876.

Watkins, D. K., and C. L. McNulty (1984), Paleontological synthesis, Leg 77, in *Intl. Repts. DSDP, 77*, edited by R. T. Buffler, et al., pp. 703-714, U.S. Government Printing Office, Washington, D. C.

Weberling, K. D. (2002), Clastic intrusions and cold seeps in the late Cretaceous-early Tertiary Great Valley forearc basin, Panoche Hills, CA: Structural context of a linked fluid system, 48 pp, University of California, Santa Cruz, University of California, Santa Cruz.

Whalen, M. T., S. P. S. Gulick, Z. F. Pearson, R. D. Norris, L. Perez-Cruz, and J. Urrutia-Fucugauchi (2013), Annealing the Chicxulub Impact: Paleogene Yucatán Carbonate Slope Development in the Chicxulub Impact Basin, Mexico, *SEPM Special Publication*, *105*.

Worzel, J. L., W. Bryant, A. O. Beall, Jr., R. Capo, K. Dickinson, H. P. Foreman, R. Laury, B. W. McNeely, and L. A. Smith (1970), *Intl. Repts. DSDP, 10*, U.S. Government Printing Office, Washington, D. C.

Yancey, T. E. (1996), Stratigraphy and depositional environments of the Cretaceous-Tertiary boundary complex and basal Paleocene section, Brazos River, Texas, *GCAGS Trans.*, *46*, 433-442.

Yancey, T. E., and C. Liu (2013), Impact-induced sediment deposition on an offshore, mud-substrate continental shelf, Cretaceous-Paleogene boundary, Brazos River, Texas, U.S.A, *Journal of Sedimentary Research*, *83*(4), 354-367.

Zimmerman, J. (1944), Tumey sandstone (Tertiary), Fresno County, California, *AAPG Bulletin*, *28*(7), 953-976.

Zoback, M. D., D. Moos, L. Mastin, and R. N. Anderson (1985), Well bore breakouts and in situ stress, *Journal of Geophysical Research: Solid Earth (1978–2012)*, *90*(B7), 5523-5530.

Vita

Jason C. Sanford is an M.S. recipient at the Jackson School of Geosciences at the University of Texas at Austin. His M.S. work focused on the geologic record of the Chicxulub asteroid impact in the Gulf of Mexico (with the Gulf Basin Depositional Synthesis Project) and the geomechanics of reservoir-scale sand injectites in the Panoche Hills of central California (with UT GeoFluids). Jason now works at Chevron as an exploration earth scientist in the deepwater Gulf of Mexico. Jason obtained his B.A. in geology and Spanish at Middlebury College and is a native of Dallas, Texas.

E-mail address: jason.charles.sanford@gmail.com

This thesis typed by the author.